UNIVERSIDAD TECNOLOGICA NACIONAL
Facultad Regional Concepción del Uruguay
INGENIERIA ELECTROMECANICA

PROYECTO FINAL DE CARRERA

(P F C)

Estudio de aceros de baja aleación recubiertos con CNP mediante EPD

Proyecto N°: PFC 1809C

Autor: Alderete, Bruno

Tutores: Dr.-Ing. Suárez, Sebastián
M.Sc. MacLucas, Timothy

Dirección de Proyectos:
Ing. Puente, Gustavo
Ing. De Carli, Aníbal

AÑO 2018

Ing. Pereira 676 – C. del Uruguay (3260) – Entre Ríos - Argentina
Tel. / Fax: 03442 – 425541 / 423803 - Correo Electrónico: frcu@frcu.utn.edu.ar

Contents

Abstract

As a solution for sucker rod corrosion during transport, a carbon nanotubes (CNT) coating is investigated to protect the rod from aggressive corrosive agents. Based on the literature, two main additives are used to deposit CNT via electrophoretic deposition (EPD), Magnesium nitrate hexahydrate (Mg-Nit) and Triethylamine (TEA). Depending on the additive used, the coating presents different characteristics. In the case of Mg-Nit, the coating produced is hydrophilic, but shows adequate adhesion to the substrate. For TEA on the other hand, the coating is near super-hydrophobic but the adhesion to the substrate is weak.

Therefore, the deposition parameters are optimized to produce the best-performing coating, in terms of corrosion protection. To improve on the individual flaws that each additive possess, a double deposition system is implemented, along with additional post-processes that look to improve the coating's properties.

After analyzing via sessile drop test the post-processed samples, the resulting coatings are characterized as hydrophobic regardless of the additive used. Additionally, the post-processed samples present enhanced adhesion when compared to the original, as-deposited samples. As a possible alternative, a double deposition system was studied, taking advantage of the individual strengths of both additives. This coating system proved to be effective showing hydrophobic behavior and adequate coating adhesion.

Furthermore, a thorough characterization of the coating was conducted along with the characterization of the substrate itself. Further coating analysis include structural, thickness and compactness, and chemical. In regards to the substrate, hardness, roughness and phase analysis were investigated.

Resumen

Para proteger las varillas de bombeo que se emplean en la industria petrolera de la corrosión durante su transporte, se estudia un recubrimiento de nanotubos de carbono (CNT por sus siglas en inglés) que proteja las varillas de agentes corrosivos. Basándose en la literatura, existen dos aditivos utilizados para efectuar la deposición de CNT a través de la técnica deposición electroforética (EPD por sus siglas en inglés), nitrato de magnesio hexahidratado (Mg-Nit) y trietilamina (TEA). Las características del recubrimiento obtenido dependen de la elección de aditivo. Para el caso del Mg-Nit, se obtiene un recubrimiento hidrófilo pero que presenta una adhesión al sustrato adecuada. Para la TEA, el recubrimiento se comporta como un material cuasi súper hidrofóbico. Sin embargo, este recubrimiento posee una adhesión débil con el sustrato.

Por lo tanto, se han optimizado los parámetros de deposición de tal forma que se obtenga un recubrimiento con las mejores características anticorrosivas posibles. Buscando mejorar las deficiencias propias de cada aditivo, se ha implementado un sistema de deposición doble. A su vez, procesos posteriores a la deposición se han implementado con el objetivo mejorar las propiedades de los recubrimientos.

Luego de un análisis a través de ensayos de gota sésil, todas las muestras que han sido sometidas al post-proceso presentan características de hidrofobicidad sin importar que aditivo se ha usado. Adicionalmente, las muestras que han sido post-tratadas presentan una mejor adhesión en comparación con las muestras originales sin dicho tratamiento. Como posible alternativa a este tratamiento posterior, se estudió el sistema de doble deposición, buscando capitalizar las ventajas inherentes de cada aditivo. Con este sistema dual, se han obtenido recubrimientos que demuestran un comportamiento hidrofóbico y que su adhesión con el sustrato es adecuada.

Adicionalmente, una caracterización exhaustiva ha sido realizada, tanto del recubrimiento como del sustrato mismo. En lo que respecta a la caracterización del recubrimiento, se han realizado análisis estructurales, de espesor y compacidad, y químicos. En el caso del sustrato, se ha estudiado su dureza superficial, rugosidad y fase del mismo.

Acknowledgements

With the following words I aspire to acknowledge all those that were somehow involved in the making of this thesis.

For starters I would like to thank Dr. Sonia Brühl. None of this would have been possible without her trust and support throughout this whole experience. Additionally, I would like to thank Prof. Frank Mücklich for giving me the opportunity to carry out my experimental work at his institute, and Dr.-Ing. Flavio Soldera for his help throughout the previous stages of my stay in Saarbrücken.

Many thanks go to GradUS Global for financially supporting my trip and stay in Saarbrücken, giving me the possibility to carry out my research.

I would also like to thank all the wonderful people that I met at Saarland University, in specific my two tutors: Dr.-Ing. Sebastián Suárez and M.Sc. Timothy MacLucas. I am extremely thankful for all their time, dedication and effort. They have taught me so much and have played a key role in this thesis. Additional thanks go to Rafael Puyol for conducting all the resistivity measurements.

Many thanks to all members of the Surface Engineering Group (GIS), and all other people that have influenced me throughout the last six years. Especially my dear friends, who have made studying (most of the time) fun and enjoyable. Their support and friendship has been essential throughout this entire process.

Last but not least, I would like to thank my parents, my sister and my girlfriend. Their love and support has been vital every step of the way, and for that I am truly thankful. I would not be the person that I am today without all of them in my life. This achievement is as much theirs, as it is mine.

-Bruno Alderete
Concepción del Uruguay, November 2018

1. Introduction and Motivation

In an oil extraction well, many different pieces and components are combined to get the job correctly done. All these elements play a key role for the extraction process. In specific, sucker rods are the link that connect the components on the surface (motor group) with the components downhole (pump). A schematic of a typical oil extraction site is shown in **Fig. 1**, along with a detailed image of the sucker rods used.

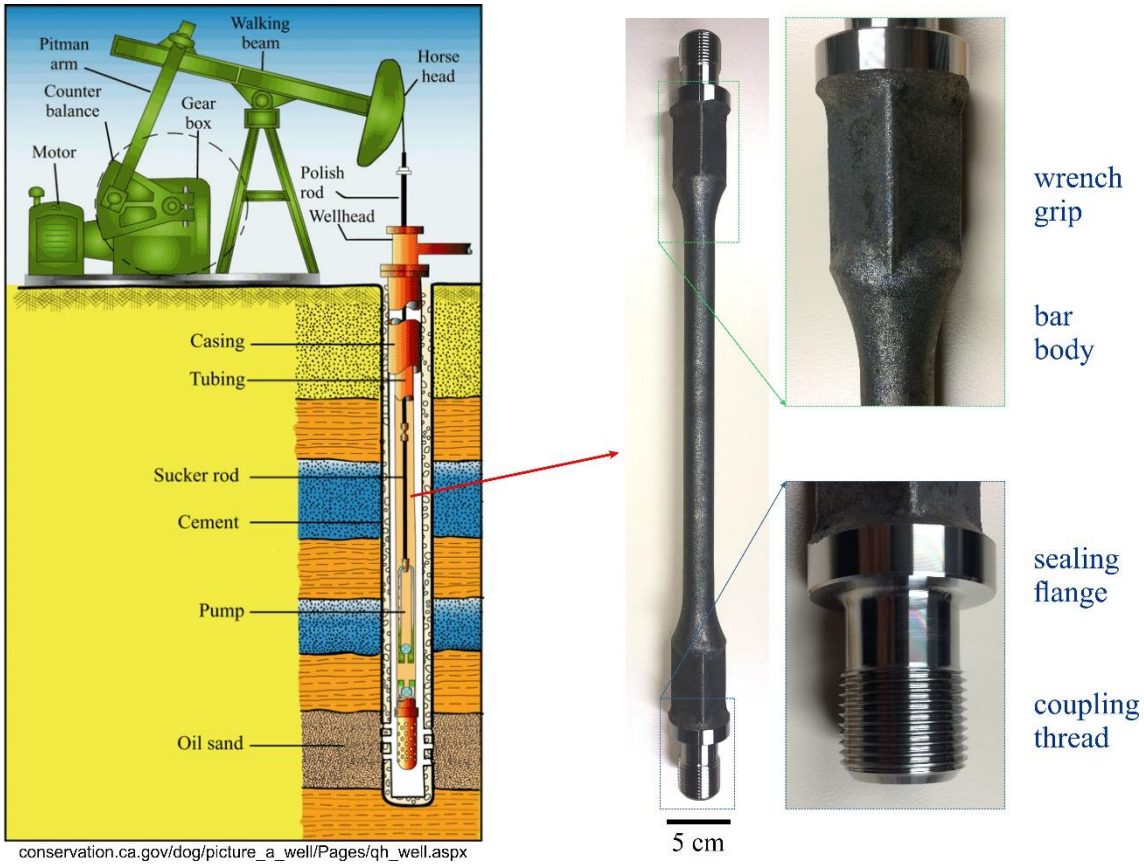

Fig. 1 - Schematic drawing of oil well and detailed image of the characteristics of a sucker rod.

Due to the nature of a sucker rod's application, maintenance work and substitution of these components is extremely complicated, time-consuming and costly. Therefore, it is of great importance that these components arrive on-site unaffected and that they are mounted correctly as to not affect their expected duty life. Consequently, these components will require premature maintenance or, in severe cases, untimely substitution of the component as a whole.

The failure of one, or many, of these components entails various consequences. Initially, the entire oil extracting process must be interrupted. This unscheduled stop

would generate significant financial setbacks. The substitution or repair's cost is insignificant in these cases, but halting the extraction process for an indefinite amount of time generates enormous financial losses. Apart from the operational responsibilities that these components have, they also entail an important safety obligation. If the sucker rods are mounted with defects present, the chances of a component failure are significantly increased. Consequently, the failure of these components produces safety hazards for all workers on-site, putting in danger their lives and the physical integrity of the equipment used.

The primary obstacle that the sucker rods face is preventing their corrosion. Due to the nature of the steel used to manufacture the sucker rods, these pieces are prone to be corroded in aggressive environments, specifically during transport. The sucker rods (as many components used at wells) are usually produced far from the operation site. During their transport, the rods endure harsh, saline environments at sea (or seashores) which may compromise the properties that these possess once they are mounted in the well.

As a solution to this problem, the main concept is to apply a protective film over the sucker rod's surface that would hinder the rod's surface to be exposed to corrosive agents present in the environment. This way, a protective barrier is placed between the sucker rods and the atmosphere, precluding corrosion to occur. The proposed film is a carbon nanotube (CNT) coating deposited via electrophoretic deposition (EPD). Based on the available literature, there are two different additives used to deposit the nanotubes on the rod's surface. Depending on the additive used, the coating deposited presents different tribological and wetting characteristics. Although for the problem at hand, the determining property is the coating's wetting behavior.

As a possible solution, it has been found that a post-deposition "cooking" process in crude oil enhances the coating's wetting and adhesive characteristics. From the study conducted, three very important tendencies were notices:

1. On all the Mg-Nit-based coatings, the sample's wetting behavior improves significantly with the coating's thickness. In other words, the samples do not require extensive cooking times. A short cook time of 1 day is sufficient to improve the wetting behavior. It is very important to highlight that however short the cooking time is, the samples must be cooked in order to obtain said enhanced properties.
2. On all the TEA-based coatings, the sample's wetting behavior is greatly improved by the length of the cooking time. The coating's thickness is not

very important as long as the entire sample is covered by CNT. However, out of all the TEA samples, the best contact angle measurements were obtained for the samples that were cooked for three and four days. The other samples did present an enhancement, but for prolonged cook times the results were better.

3. Correctly drying and removing excess oil from the coating is extremely important. When a sample was incorrectly dried, the regions with excess oil resulted being hydrophilic, making this process counterproductive.

Once *in operando,* the coating applied must withstand the well conditions: wear and corrosion. Many papers establish that carbon nanotubes reduce friction and wear on steel surfaces acting as solid lubricants [1]–[3], but this analysis lays outside of the scope of the present thesis. The coating however, must remain adhered to the rod during normal applications or it must be completely degraded during the extraction process. The reason for this is that the detached coating must not block pump filters. Therefore, the coating has two alternatives; it either remains adhered to the substrate or be detached and degraded into small agglomerates that do not obstruct the downhole components of the well.

In the present thesis, three different coating systems are studied to establish the most appropriate coatings in terms of corrosion protection. There is a wide span of critical factors for designating the best coating. The primary factor is the wetting behavior (as derived from the contact angle between a water droplet and the coating). This parameter is fundamental when assessing corrosion protection, since for low wettability, the contact between the rod and corrosive agents would be effectively avoided. Another parameter is the adhesion, where the coating must not easily detach from the rod. The final two parameters do not relate to performance of the coating, but are equally important.

Considering that this is a field application in a widespread industrial field (oil extraction and transport), the chosen coating process must be able to be straightforwardly up-scaled from a laboratory into an industrial scale. This up-scalability entails the ability to mass deposit CNT, along with considering the safety of the workers in charge of the deposition processes. Lastly, because of the industrial application of this process, the most cost-effective coating is selected. All the deposition parameters must be optimized keeping these last two considerations in mind.

2. Theoretical Framework and State of the Art

2.1. Carbon nanoparticles

Carbon is the most abundant element in our planet and the second most abundant element in the human body. In recent times, carbon materials have been in the focus of nanotechnology due to their ability to produce new materials with particular properties [4]. Because of the valence of carbon, it is able to form a great number of different allotropes. In this section, carbon nanotubes will be discussed, providing a brief theoretical overview of their structure, synthesis, and properties.

2.1.1. Carbon nanotubes

Perhaps the most studied allotrope of nanometric carbon are carbon nanotubes (CNT) [4]–[9], and in recent years CNT have definitely grown in interest. CNT are a sp^2 hybridized allotrope, with a hollow, cylindrical shape. They can be closed, with fullerene-shaped caps at their ends, or they can be open at their ends. CNT have the particularity of possessing a high aspect ratio, being quasi-one dimensional. When a CNT is made up of only one tube shaped carbon structure, it is called a single-walled carbon nanotube (SWCNT). If a CNT is comprised of two or more concentric SWCNT, it is called a multiwall carbon nanotube (MWCNT). CNT generally possess a diameter in the order of nm, while having a length that can reach several mm.

To understand CNT, they can be thought of as a single two-dimensional graphene structure that has been wrapped in a cylindrical shape. It is very important to keep in mind that this is not how CNT are synthetized, it is merely a visual aid to better understand CNT. **Fig. 2.1** represents three different sp^2 carbon allotropes obtained from a single 2D graphene sheet.

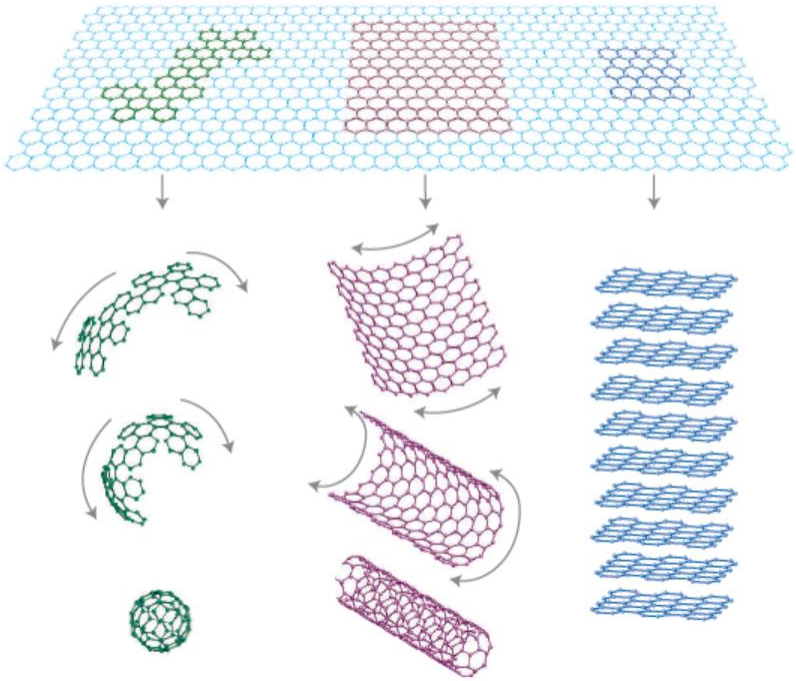

H.X. Kong, "Hybrids of carbon nanotubes and graphene/graphene oxide." *Curr. Opin. Solid State Mater. Sci.*, vol. 17, pp. 31-37, 2013.

Fig. 2.1 - Obtaining of fullerene, CNT and graphite (from left to right) parting form graphene analogy.

Given that CNT present sp^2 hybridized allotropes, each carbon atom possesses three strong, covalent, planar sigma (σ) bond and two high mobility pi (π) bonds, as shown in **Fig. 2.2**. The σ-bonds define the CNT's mechanical properties due to the strength of these bonds. The π-bonds, on the other hand, are very weak, caused by Van-der-Waals forces. These π-bonds, due to their high mobility define the CNT's transfer properties, such as thermal and electrical conductivity. The delocalized p_z orbitals are the ones responsible for CNT agglomeration.

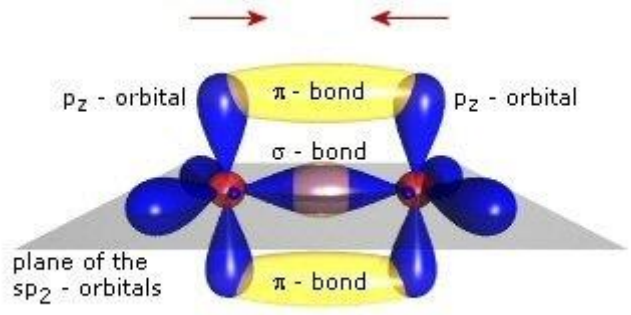

https://etd.ohiolink.edu/!etd.send_file?accession=wright1450358356&disposition=inline.

Fig. 2.2 – sp^2-hybridized carbon atom with bond illustration.

CNT have a curved carbon structure. For this reason, the sp^2 plane shown in **Fig. 2.2** is consequently also curved. This curvature causes one of the π-bonds to become weaker (the outer bond), and the other π-bond to become stronger (the inner bond). Therefore, the diameter of the CNT is an important parameter. If the diameter is too large, the sp^2 plane's curvature is very small and the π-bonds aren't affected. However, if the diameter of the CNT is too small, the sp^2 plane's curvature is very large and the inner π-bond is greatly strengthened and the outer π-bond is greatly weakened. Therefore, the CNT's diameter defines its reactivity. The more the π-bonds are affected, the more reactive a CNT is, while the fewer the π-bonds are affected, the CNT will be less reactive. This is important when CNT must be chemically functionalized, because smaller diameter CNT (weaker π-bonds) are more reactive and more easily functionalized.

There are three primary industrial methods for CNT synthesis, these are: arc method, laser ablation and by CVD. Being the latter the most commonly used synthetization method due to its up-scalability to industrial levels and thus being used for large-scale production of CNT. CVD CNT growth requires a carbon source, transportation fluid, furnace, substrate and catalyzer. Generally, carbon is provided by acetylene, ethylene, ethanol or a hydrocarbon, generally methane. The transportation fluid generally is ammonia, hydrogen or nitrogen. Inside the furnace, the decomposition of the process gas occurs by applying temperature. The growth of the CNT occur on the surface of the catalyst material, also inside the furnace. The substrate occupied is generally a silicon wafer, while the catalytic materials used are nickel, cobalt, iron, platinum or other transition metals.

CVD CNT synthesis consists of two main steps. The first step is the preparation of the catalyst via sputtering, PVD or dip coating. Once the catalyst has been prepared, the substrate is heated in a carbon rich atmosphere at a temperature where the process gas will be decomposed. With this, the reactive carbon reacts with the substrate. When the substrate has reached its intrinsic saturation point, carbon begins to precipitate on the substrate and CNT grow over its surface.

This method presents various advantages, some of which have already been mentioned. It is a very versatile process, since a great number of process gases, catalyst and substrates can be occupied. It is cheap and simple, with excellent control over the growth parameters, and it is done at relatively low temperature (between 500ºC and 1000ºC, while laser ablation is done at around 1200ºC) and atmospheric pressure. It also allows CNT growth in a number of forms, such as aligned or entangled, straight or coiled,

in films, etc. However, the CNT obtained by CVD present lower crystallinity than CNT synthetized by arc discharge or laser ablation. CVD allows a continuous growth of CNT up to a certain point, at which the catalyst is "poisoned". To prolong the duty cycle of the catalyst, steam can be inserted, along with the other gases. This steam helps purify the catalyst and prevent premature "poisoning".

The intrinsic properties that a CNT possesses depends exclusively on how the CNT grows during synthetization. Depending on the orientation that the graphene structure has when "rolled up", the CNT's properties differ. This is known as a CNT's chirality [10]. The specific orientation of a CNT's chirality is defined by a chiral vector. This chiral vector is defined by two integers (*m*,*n*), known as chiral index. **Fig. 2.3** shows a representation of a planar graphene sheet in which the chiral vector can be identified. Two atoms are chosen from this sheet, one of which is used as the chiral vector's origin. The chiral vector $\vec{C}$ points from the origin atom, towards the second atom chosen, and is defined by Eq. (1):

$$\vec{C} = n \cdot \vec{a} + m \cdot \vec{b} \quad (1)$$

Where, $\vec{a}$ and $\vec{b}$ are the unit cell vector of a 2D lattice formed by a graphene sheet.

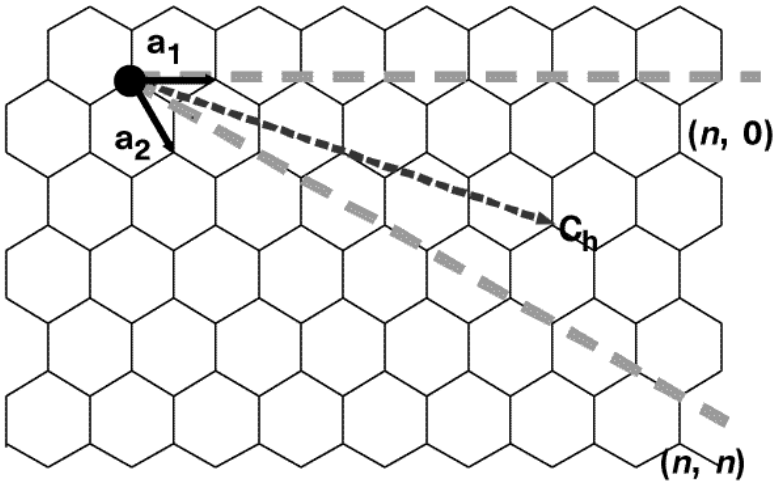

T.W. Odom, J. Huang, P. Kim, C.M. Lieber, "Atomic structure and electronic properties of single-walled carbon nanotubes." *Nature*, vol. 391, pp. 62-64, 1998.

Fig. 2.3 – Schematic representation of the hexagonal grid of a graphene sheet illustrating the unit vector a_1 and a_2 and the chiral vector.

The chiral angle θ is formed between the $\vec{a}$ vector and the chiral vector. This angle also helps to determine the chirality of a CNT.

There are three possible chiralities a CNT may possess and are shown in **Fig. 2.4**. These are:

1. Armchair. When $n = m$ and $\theta = 0°$

2. Zigzag. When $m = 0$ and $\theta = 30°$.
3. Chiral. When $n \neq m$ and $0° < \theta < 30°$

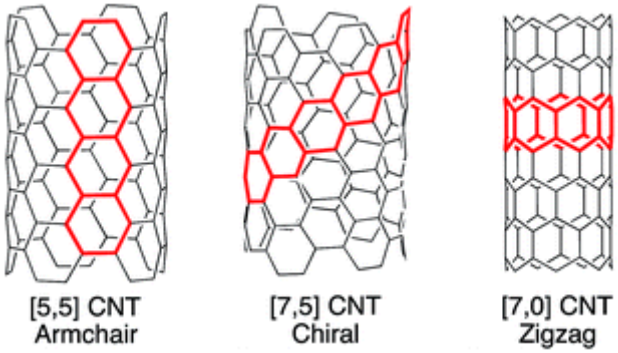

T.S. Sisto, L.N. Zakharov, B.M. White, R. Jasti, "Towards pi-extended cycloparaphenylenes as seeds for CNT growth: investigating strain relieving ring-openings and rearrangements." *Chem. Sci.*, vol. 7, pp. 3681-3688, 2016.

Fig. 2.4 – Different chiral configurations of a SWCNT: armchair, chiral, and zigzag, respectively.

Important information can be obtained from the chiral vector of a CNT:

- The CNT's circumference is given by the length of $\vec{C}$.
- The values of m and n determine the chirality of CNT. Different chiralities possess different optical, mechanical and electrical properties.
- The density and interlayer spacing of CNT depend on their chirality.

For this latter reason, the periodic table of CNT is of great significance, and is shown in **Fig. 2.5**. Given the values of m and n, one can extract the CNT's properties and behavior. The reason for a CNT's varying properties depending on its chirality is simple due to a difference in energy gaps when rolled up in different manners.

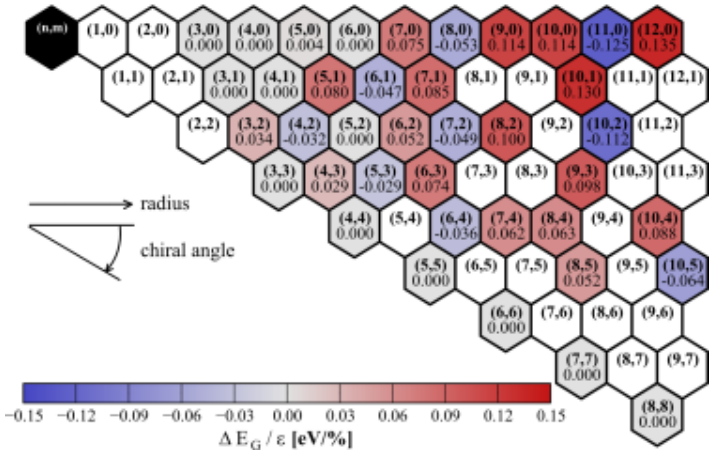

https://www.zfm.tu-chemnitz.de/for1713/projects.php.en.

Fig. 2.5 - Periodic table of CNT, representing the dependence of the energy gap for different chiralities.

There are four mayor defects that a CNT may present [11]. These are:

- Structural defects.
- Bond rotations.
- Doping-induced defects.
- Non-sp^2 carbon defects.

Structural defects are related to imperfections that distort the curvature of the hexagonal carbon structure of a CNT. This usually occurs when there is a non-hexagonal carbon ring that is surrounded by hexagonal carbon rings.

Bond rotation result from the 90° rotation of two bonded carbon atoms. This rotation results in the transformation of four hexagonal carbon rings into two heptagonal carbon rings, and two pentagonal carbon rings. The heptagonal carbon rings are weaker than the hexagonal, and the pentagonal carbon rings are stronger.

Doping induced defects appear when the graphitic lattice has non-carbon atoms embedded in it. Nitrogen and boron are typically found in sp^2 lattices. These two elements tend to increase the CNT's surface reactivity as a result of the number of electron each element possesses.

Non-sp^2 carbon defects are caused by high reactive carbon atoms found in the lattice, such as vacancies, interstitials, edges (in the case of open CNT), among others.

As it was mentioned before, CNT present outstanding mechanical properties. They are far stronger than steel and they weigh much less, and they are as hard as diamond, but possess a greater thermal capacity. CNT are thermally stable at elevated temperatures and are great electrical conductors. They also can act as metallic, semi-metallic or semiconductors, depending on their chirality. Although, CNT can never act as insulators. The major drawback to CNT are the strong Van-der-Waals interactions that form the agglomerates (p_z orbitals). These agglomerates are not easily separated and they reduce the excellent properties that individual CNT present.

2.2. Deposition techniques

There are several particle deposition techniques used in science and in the industry, some very simple and others very complex. In this section, the most widely used techniques, due to their simplicity, will be briefly explained.

2.2.1. Dip coating

As the name states, dip coating [12]–[14] consists of dipping the substrate in a liquid coating medium, followed by the removal of the substrate. The coating is deposited onto the surface through three key steps.

The first step is the immersion of the substrate in the medium, followed by the withdrawal. Once the substrate has been removed from the medium, the next step is the evaporation of the liquid solvent, leaving the solid film on the substrate's surface. This last step is usually accompanied by physisorption, which is a reactions that occurs between the solid coating and the substrate itself. **Fig. 2.6** shows the step-by-step process of dip coating.

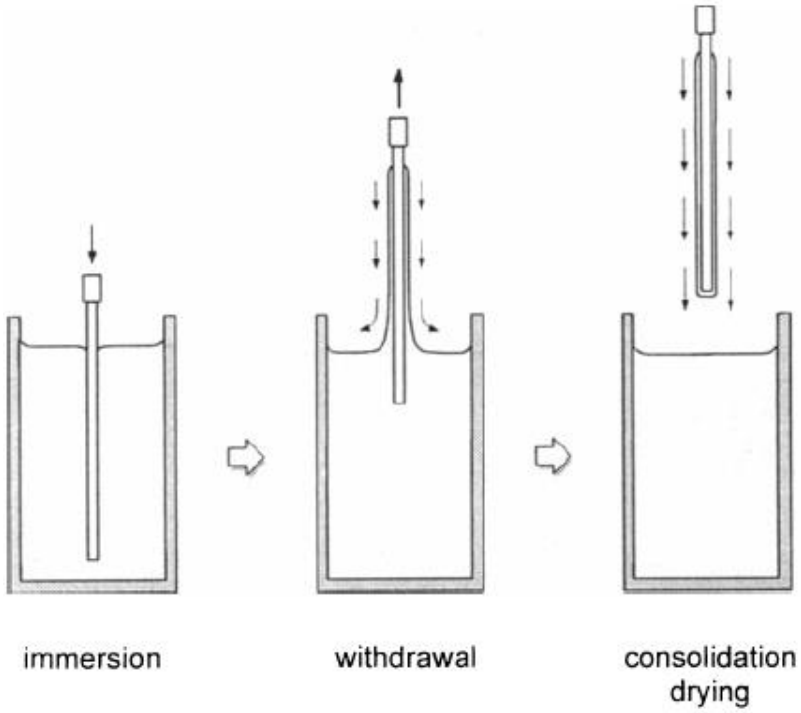

J. Puetz and M. A. Aegerter, "Dip Coating Technique," Sol-Gel Technol. Glas. Prod. Users, pp. 37–48, 2004.

Fig. 2.6 – Schematic representation of the dip coating deposition process.

Dip coating is a simple process that results in high quality coatings for a relatively low cost. For these reasons, it is extensively used for industrial applications, as well as for research purposes. However, this technique does not allow the film thickness to be controlled and the quality of the coating depends on the wettability of the substrate. If the medium has high wettability with the substrate, once this one is removed from the medium, the liquid will drag the coating down. Resulting in a very inhomogeneous coating, especially in the lowermost region of the coated material.

An alternative dip coating method is the Langmuir-Blodgett assembly [15]. This method involves forming a layer of the coating material on the surface of a liquid, instead of dispersing it in a suitable medium. This is achieved using an emulsion, allowing the coating material to remain on the interface between the two fluids. Once this is obtained, the substrate is dipped in the medium and later removed. This way, once the substrates comes into contact with the coating material, this material adheres to the substrate. **Fig. 2.7** illustrates the Langmuir-Blodgett assembly. In this technique, the coating also remains adhered to the substrate's surface by physisorption.

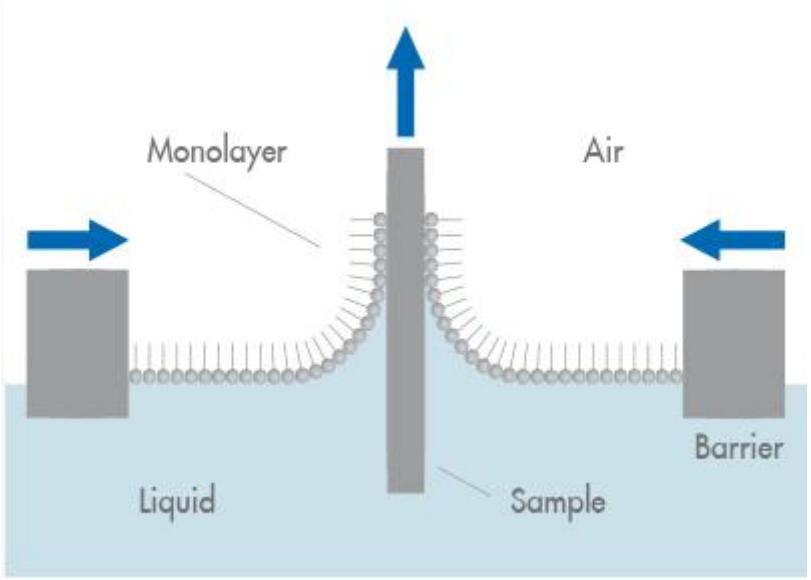

https://www.researchgate.net/publication/296488838_Boron_Nitride_and_Carbon_Nanostructures_Synthesis_Characterization_and_Ab_Initio_Calculations.

Fig. 2.7 - Langmuir-Blodgett assembly using a liquid and air as fluids.

2.2.2. Spin coating

Spin coating [16]–[18] is a widely used coating technique that generates a uniform, thin film over the substrate's surface. It basically consists of depositing a colloid, containing the deposition material, on the sample and dispersing it over its surface uniformly via rotation. This coating is achieved through four steps, which are: deposition, spin-up, spin-off and evaporation.

The first step, deposition, requires an excess of the liquid solvent with the deposition material to be deposited on the surface of the substrate. In this stage, the substrate can be still of it can be rotating at low speed. In the second step, the liquid starts to flow radially outward due to the centrifugal forces that are generated due to the rotation of the substrate. During this step, the substrate achieves speeds of up to several thousand rpm. Once the set speed is reached and the liquid has flowed towards the edges of the

substrate, the third step begins. Here, the excess liquid is accumulated on the edges, it forms droplets, and these droplets fly off the substrate. This leaves behind a thin, solid film. The film becomes completely solid once the fourth and last step is complete, the evaporation of the liquid medium. **Fig 2.8** illustrates the mechanisms of spin coating.

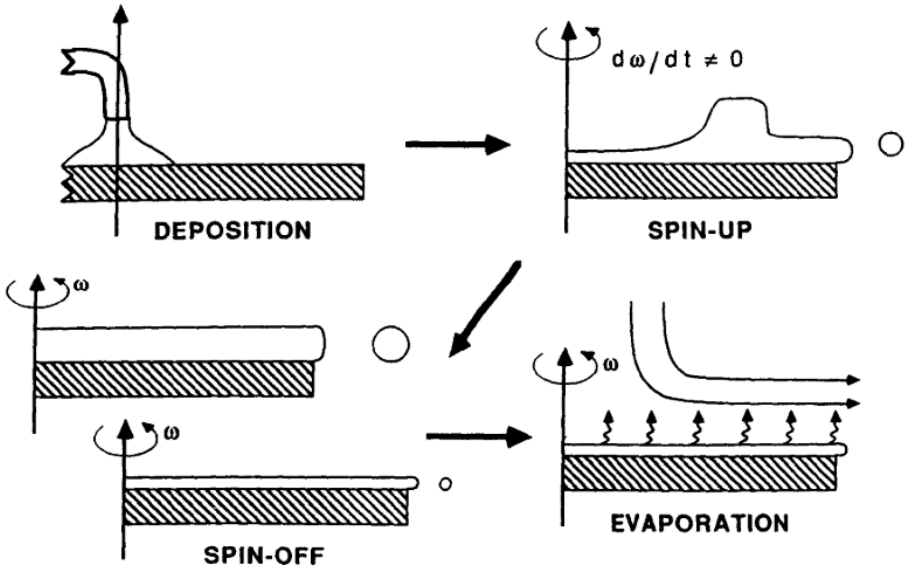

L. E. Scriven, "Physics and Applications of Dip Coating and Spin Coating," *Better Ceram. Through Chem. III*, vol. 121, pp. 717–729, 1988.

Fig. 2.8 - The four steps of spin coating.

An alternate form of spin coating involves the use of the off-spun droplets. This means that at the center, a spinning disc is placed, where the coating solution is deposited. This liquid flows radially outwards and spins off from the disc. Around the disc, the substrates are placed vertically. When the droplets fly off the disc, they impact the substrates and dry on their surface, leaving behind the coating material.

This disposition technique is fast, simple and cheap, it requires very elementary equipment, and has very few parameters, which makes it easier to control the results obtained. However, it cannot be used for large substrates and there is a lack of material efficiency, since most of it is wasted during the spin-off step. Furthermore, the rheology of the solution must be taken into consideration, somewhat complicating the process.

2.2.3. Drop casting

Drop casting [14] is a simple method that involves depositing drops of a liquid that contains the desired coating material, over the substrate's surface. Once the drops have been deposited, and the solvent has evaporated, what remains is the coated surface.

The coating left behind after evaporation remains adhered to the substrate by physisorption. **Fig. 2.9** shows the working principal of drop casting.

This method presents the advantage that it is extremely simple. The coating material is simply mixed in a suitable solvent and dropped onto the surface. However, it is very difficult to control the thickness of the coating, resulting in a very inhomogeneous coating. In some cases, multiple deposition processes are necessary to obtain a usable coating. Therefore, this method is applied when coating precision is not required.

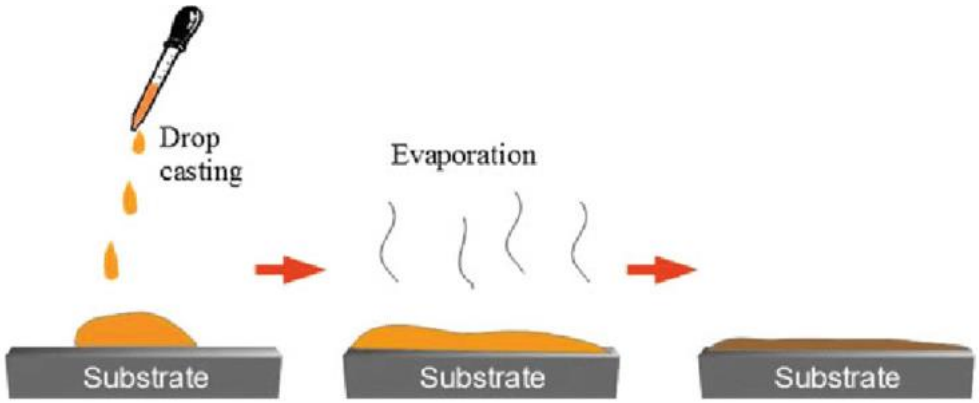

https://www.researchgate.net/figure/Perovskite-deposition-using-drop-casting-technique-99_fig5_321396151.

Fig. 2.9 - Schematic representation of the drop casting process.

This inhomogeneous coating is a consequence of the Marangoni Effect [19], [20]. When a drop is casted onto the surface of the substrate, the solvent begins to evaporate. During the evaporation process, the dispersed coating material begins to move inside the drop in a convective motion as a result of surface tension gradients. Due to this movement, the dispersed material tends to accumulate on the edges of the droplet. Since there is less mass on the edges, this is where the solvent evaporates the fastest, leaving on these regions the material over the substrate. Therefore, a coating gradient is generated, in which there is a higher coating density located where the edges of the drops were, and no coating where the center of each drop was located. This is known as the coffee-stain effect [21], due to the similarity between the ring-like deposition pattern and the resemblance to the shape of a coffee stain. **Fig. 2.10a** illustrates the convective motion inside the drop and **Fig. 2.10b** the coffee-stain effect left behind.

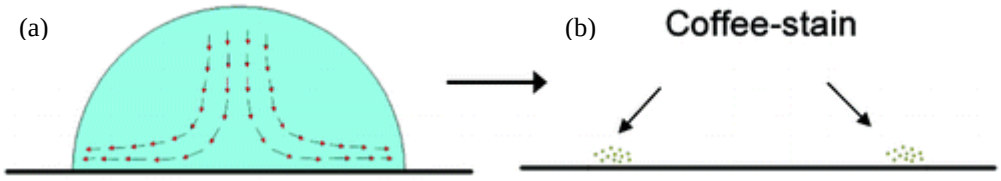

M. Majumder, C.S. Rendall, J.A. Eukel, J.Y.L. Wang, N. Behabtu, C.L. Pint, T.Y. Liu, A.W. Orbaek, F. Mirri, J. Nam, A.R. Barron, R.H. Hauge, H.K. Schmidt, M. Pasquali, "Overcoming the coffee-stain effect by compositional Marangoni-flow-assisted drop-drying.", *J. Phys. Chem.*, vol. 116, pp. 6536-6542, 2012.

Fig. 2.10 - (a) Marangoni convection within the drop; **(b)** Coffee-stain effect.

2.2.4. Spray coating

Spray coating [22], [23] is a coating technique that can be performed with or without applying heat, although it is most commonly done thermally. These techniques involve the Venturi effect [24].

The main difference between the two types of spray coating is the state of the coating material. In thermal spray coating, the coating material is in solid state, it is molten via heat and it is spread over the substrate's surface. In cold spray coating, however, the coating material must be dispersed in a suitable solvent, similarly to the other coating techniques. Therefore, through the Venturi effect, this disaggregation can be transported towards the substrate. Once the disaggregation reaches the substrate, the solvent evaporates and the coating material is left behind forming the coating layer through physisorption. The schematic image shown in **Fig. 2.11** describe the working principal of cold spray coating.

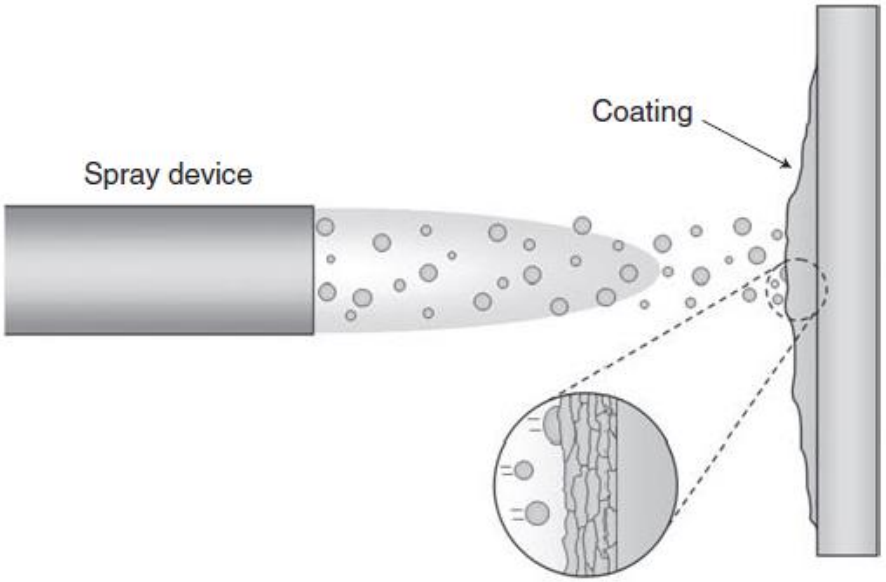

M.F. Smith, "Comparing cold spray with thermal spray coating technologies." *Fundamentals and applications*, pp. 43-61, 2007.

Fig. 2.11 – Schematic representation of spray coating.

2.2.5. Electrophoretic deposition

The chosen deposition technique for the CNT coatings is electrophoretic deposition (EPD). EPD [25] is a relatively straightforward deposition method used to create films or coatings through the use of a colloidal dispersion (between a suitable solvent and the deposition material). For the deposition to take place, this technique requires a DC voltage power source, a solvent with the dispersed functionalized (covalently or non-covalently) CNT and two electrodes (one of which will be coated with the CNT).

Once dispersed, the CNT particles move through the disaggregation by electrophoresis. In order for particle movement to take place, the applied force must be strong enough to overcome three fundamental forces [26]:

- Gravitational forces that make the particles sink or rise depending on their density.
- Drag forces as a consequence of the fluid's viscosity (resistance to the particle's motion).
- Kinetic energy of the particles and molecules.

The deposition method is simple. The two electrodes are submerged in a glass vessel that contains the solvent with the dispersed CNT. On their end, the electrodes are connected to the DC power source. The distance between the anode and the cathode must remain constant during the deposition process. **Fig. 2.12** shows a schematic diagram of the deposition method.

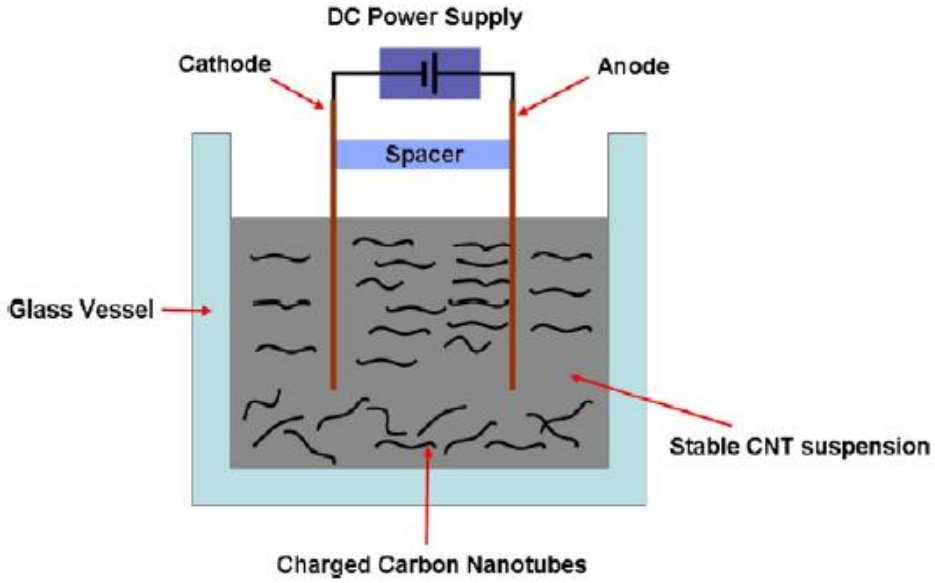

A.R. Boccaccini, J. Cho, J.A. Roether, B.J.C. Thomas, E.J. Minay, M.S.P. Shaffer, "Electrphoretic deposition of carbon nanotubes.", *Carbon*, vol. 44, pp. 3149-3160, 2006.

Fig. 2.12 - Schematic diagram of an EPD cell for CNT deposition.

Some advantages EPD presents are:

- Straightforward deposition technique.
- Simple equipment requirements.
- High material efficiency can be achieved.
- High packing density of coating compared to CNT coatings obtained through other deposition techniques.
- Thickness of the coating is controllable.
- It can be used to coat complex geometries homogeneously.
- Cost-effective method.
- Easily scalable to larger dimensions.

This deposition method is a two-step process [25]. First, the CNT in the colloidal dispersion must move towards the deposition electrode, this is caused by the electric field (electrophoresis). Once the CNT have reached the deposition electro, the actual deposition occurs on the substrate's surface by particle coagulation, according to Boccaccini et al. [25]. However, the most accepted deposition model is the one proposed by Sarkar and Nicholson [27]. The same bonds that cause CNT to agglomerate (Van-der-Waals forces), are the bonds that maintain the coating on the electrode, in the case of non-functionalized CNT. This is a consequence of the curvature of the carbon surface and the destabilization of the π-bonds (CNT pyramidalization). After the CNT have reached the surface of the electrode, they adhere to this surface due to the electric field. As the coating gets thicker, the new CNT adhere to the CNT already deposited. Initially, the CNT repel each other, since they have the same superficial charge. However, these particles adhere to each other due to Van-der-Waals forces (physisorption). Correspondingly, after the electric field is removed, the coating remains attached to the substrate by Van-der-Waals forces.

When the power source is switched on, an electric field is formed between the two electrodes. This electric field is the force that produces the motion of the dispersed CNT, towards the anode or cathode, depending on the superficial charge of the nanoparticles. The oxygen-containing CNT possess a negative surface charge. Therefore, when CNT are dispersed utilizing TEA the deposition is an anodic deposition. When Mg-Nit is used to disperse the CNT on the other hand, the Mg^{2+} ions attach themselves to the negatively charged surface of the CNT. Therefore, Mg-Nit based depositions occur on the cathode.

Once electrophoresis is achieved, the CNT will move towards the corresponding electrode and accumulate on its surface, forming a homogeneous coating.

The characteristics of the obtained coating depends on a number of parameters. In order to control the deposition process, and therefore obtain the desired characteristics, a good understanding of EPD kinetics in necessary. H.C. Hamaker [27]–[29] proposed a mathematical model (Eq. 2) where various parameters come into play that affect the coating :

$$\frac{dw}{dt} = \mu \cdot c \cdot A \cdot E \quad (2)$$

Where (*dw/dt*) is the deposition rate (*g/s*), μ is the electrophoretic mobility of the particles ($cm^2/s \cdot V$), c is the particle concentration used in the colloidal dispersion (g/cm^3), A is the deposition area (cm^2), and E is the applied electric field (*V/cm*).

All these parameters may be freely varied. The electrophoretic mobility of the particles depends on the particles themselves, and on the selected solvent. The electrophoretic mobility of the CNT is fixed, however the solvent selected may be varied to obtain different values of electrophoretic mobility. The particle concentration certainly may be varied, along with the electric field that is applied. The latter is controlled by varying the voltage that is applied. Lastly, the deposition area may be varied by manipulating the submerging of the electrode in the suspension.

Later on, Sarkar and Nicholson [27] added an efficiency factor to Hamaker's model. This f factor takes into consideration the fact that not all the CNT particles that reach the electrode will form part of the coating. To determine this *f* factor, authors have assumed that particle detachment during the deposition process occurs at the same rate as after the voltage source has been switched off. Therefore, considering this assumption, this factor may be determined by Eq. (3), which is the quotient between the mass flow of particles effectively deposited and the total flow of particles [29]. Mathematically:

$$f = \frac{j_i}{j_i + j_d} \quad (3)$$

Where j_i is the mass flow of particles that were deposited and j_d is the mass flow of detached particles. Since *f* is an efficiency factor, it can only take values between 0 and 1. Therefore, introducing this factor in Eq. (2), the result is the following equation (Eq. 4):

$$\frac{dw}{dt} = f \cdot \mu \cdot c \cdot A \cdot E \quad (4)$$

The electrophoretic mobility of the particles can be determined through the following equation (Eq. 5):

$$\mu = \frac{\varepsilon_0 \cdot \varepsilon_r \cdot \xi}{\eta} \quad (5)$$

Where ε_o is the vacuum permittivity, ε_r is the relative dielectric constant of the suspension medium, ζ is the Zeta potential of the particles, and η is the dynamic viscosity of the medium.

Therefore, once the electrophoretic mobility is calculated, and with the deposition area set, one can vary the remaining parameters in order to obtain the best deposition results. In summary, the different parameters that influence the characteristics of the coatings deposited via EPD are:

- Particle size.
- Dielectric constant of the solvent and permittivity.
- Electrical conductivity of the dispersion.
- Viscosity of the dispersion.
- Zeta-potential.
- Stability of the suspension.
- Deposition time.
- Applied voltage.
- Solid content of the suspension.
- Conductivity of the substrate.

3. Characterization Methods

In this section, a brief overview of the different characterization methods will be explained. The focus will be on their basic working principle and the information that can be obtained through the application of said methods.

3.1. Scanning Electron Microscope

The Scanning Electron Microscope (SEM) [30] is an instrument used to observe the surface of a certain material. The main advantage of this microscope is that it can reach a far greater magnification level compared to an optical microscope as a consequence of the wavelength of the electrons, it also has a greater depth of field. The SEM is a powerful equipment, which allows the characterization of a specimen's surface, observing its topography, irregularities and compositional variations.

The SEM microscope utilizes electromagnetic lenses to focus a beam of electrons towards the specimen's surface. When the electrons impact the surface, several by-products are obtained from this interaction. The primary by products are: secondary electrons, X-rays, Auger electros, among others. Each of these by-products are used for different kinds of analysis. The secondary electrons that are emitted by the specimen are collected by the microscope's detectors, and an image is generated. Depending on the energy the secondary electrons possess (intensity detected), the image shown has a higher or lower contrast and brightness level. A difference in intensities may be related to a change in surface orientation, showing the surface's topography, or a difference in the surface's chemistry, showing different surface phases. **Fig. 3.1a** and **Fig. 3.1b** show SEM images of CNT.

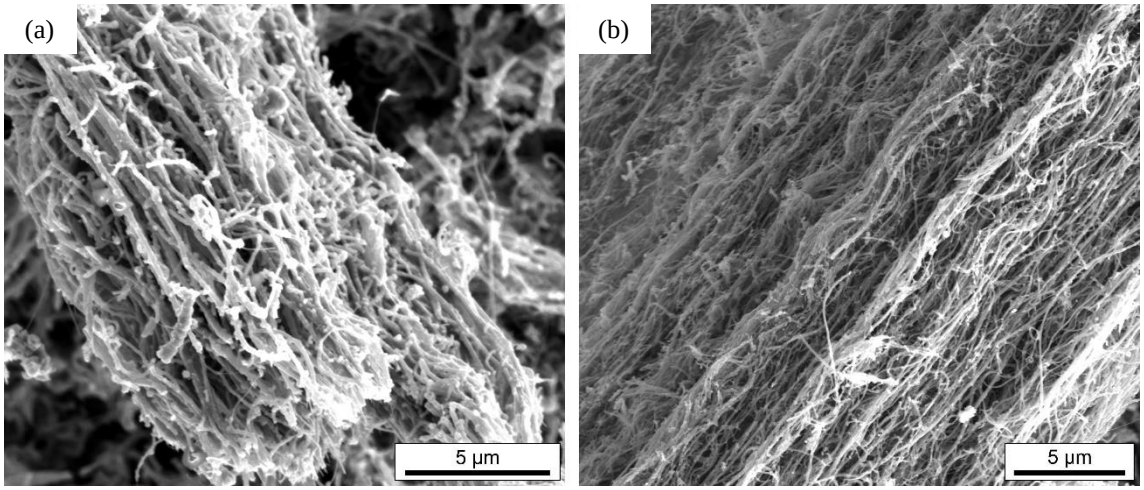

Fig. 3.1 – **(a-b)** CNT linear agglomerates as observed with SEM.

3.2. Focused Ion Beam

Focused Ion Beam (FIB) [31] is a technique which allows the operator to observe the surface of a sample and the possibility to create a cross-section of the specimen's surface. This technique is usually annexed to an electron microscope. The difference between FIB and SEM is that the latter utilizes a beam of electrons to image the sample, whereas the FIB utilizes a beam of ions (usually gallium) to produce the cross-section and image the sample.

To create the cross-section, first a thin layer of platinum must be deposited on the region of interest. This layer is applied to protect the specimen's surface from ion milling-induced curvature, avoiding the alteration of the immediate sub-surface. Once the platinum layer is deposited, the material removal process begins. It is a two-step process: the first cut is done at high current, producing a rough finishing; and the subsequent steps are performed at lower currents, polishing the cross-section in order to obtain a smoother finish. During the material removal, and due to the geometrical configuration of the dual beam microscope, the sample is tilted 52º. Therefore, an in-depth image can be observed utilizing the SEM. **Fig. 3.2a** and **Fig. 13b** show FIB cross-section of carbon nanotubes.

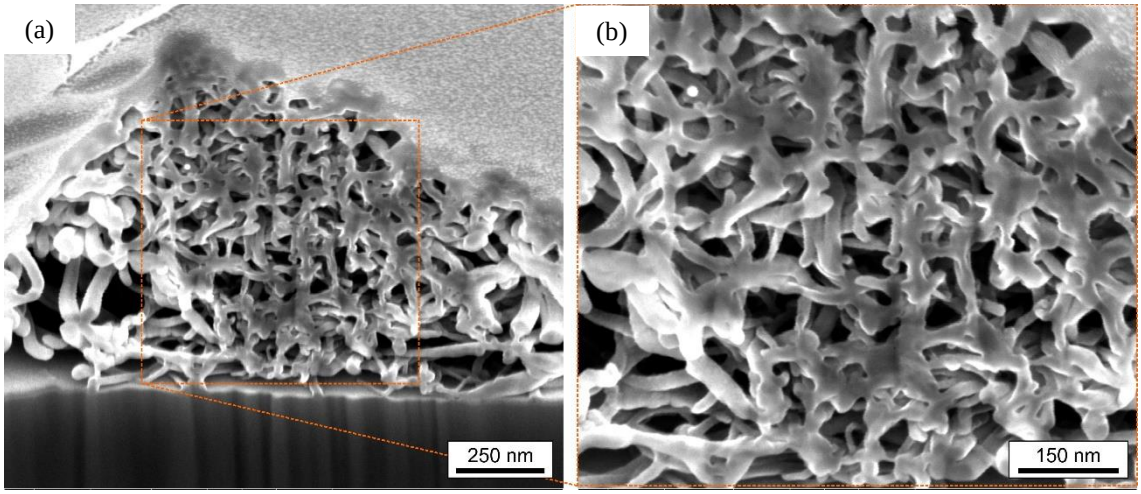

Fig. 3.2 – **(a-b)** CNT observed with SEM after FIB cut at 30 keV and 21 nA. A slight amorphization and inter-tube welding is noticeable.

One of the main disadvantages is the implantation of gallium stemming from the ion source. However, the most relevant drawback is the amorphization of the crystal structure, resulting from the high beam energy. This can generate an inaccurate measurement, especially when an in-depth chemical composition is studied. Also, FIB is a destructive technique, since it removes material from the specimen in order to create the cross-section-view.

3.3. Electron Back Scatter Diffraction

Electron back scatter diffraction (EBSD) [32]–[34] is a characterization method that allows crystallographic information to be obtained from a sample with the use of a SEM. EBSD is a powerful characterization tool that provides information about crystal type, crystalline perfection over the scanned region and the orientation of the crystalline structure.

To obtain an EBSD mapping the sample must be placed in the SEM, this sample must be tilted between 60º and 80º towards the detector. Generally done at 70º. This is done in order to increase the quality of the obtained patterns. Inside the SEM, the sample is analyzed by a focused beam of electrons. Since the SEM stage cannot reach a tilting of 70º, the specimen must be mounted on a tilted sample holder. The region of interest is covered by steps. Each step is studied carefully by the beam of electrons. At each point, some electrons are backscattered from the sample and they are collected by the SEM's detectors, forming the backscatter pattern.

The EBSD patterns are comprised of many bands with different intensities that span across the image, these bands are named Kikuchi bands [35]. Kikuchi bands are straight lines that denote the projection spot where the electron beam collides and the diffraction plane within the crystalline structure of the sample.

Once the patterns are obtained, they must be indexed in order to determine the crystallographic orientation of the sample. To do this, the Hough transformation algorithm [36] is used to transform the straight bands lines into points or peaks, which are easier to be processed mathematically. With the peaks located, and comparing them with a table of expected angles for the present phase of the sample, the crystalline structure can be retrieved. **Fig. 3.3** shows the indexed Kikuchi bands of a tetragonal Zirconia (ZrO_2) sample.

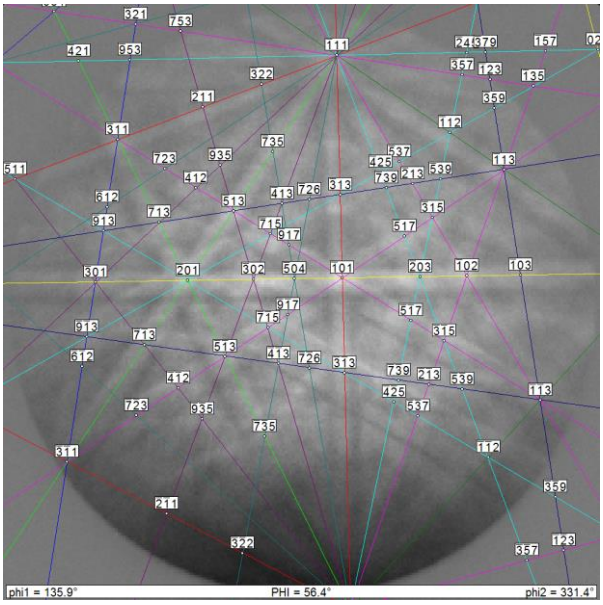

Fig. 3.3 - Indexed Kikuchi bands of tetragonal ZrO_2. The numbers in the white boxes represent different crystallographic orientations.

After a post-analysis process, the inverse pole figure (IPF) and image quality (IQ) are obtained [37]. In the IPF map each point is colored according to an automatically color coded unit triangle of the inverse pole figure, representing a specific crystallographic orientation. In the case of a cubic metal, the color red is assigned to the [001] direction, blue to [101] and green to [111]. A particular point is then shaded in the map according to the alignment of these three directions in the crystal to some user specified sample direction. This map type allows the straightforward qualitative assessment of different particularities such as grain size distribution and crystallographic texture.

The IQ describes the quality of an electron backscatter diffraction pattern, and depends on the material being measured and its condition. The factor affecting the quality of diffraction patterns, from a materials science perspective, is the state of the crystal lattice. Hence, any distortions within the evaluation volume will produce lower quality patterns. Consequently, it allows the use of the IQ as a qualitative indicator of the strain in a microstructure (which might be originated from the sample preparation).

3.4. X-Ray Diffraction

X-Ray diffraction (XRD) [38], [39] is a characterization technique which allows the user to obtain valuable information about the crystalline structure of a certain material, similarly to EBSD. XRD offers a simple method to obtain the diffraction spectrum. However, the post-analysis is very complex. Being this the main reason why one must consider between analyzing a sample via XRD or EBSD.

The diffraction phenomenon occurs when waves with similar wavelength interact. X-rays are utilized due to the fact that their wavelength is similar to the intermolecular interstice. Therefore, when an x-ray beam impacts the crystalline sample, the beam diffracts and create a characteristic pattern to the crystal's structure. The diffracted beam is collected by the detector, which processes the collected information and converts the signal to a count rate, also known as the intensity. Knowing the wavelength of the used beam and the diffraction angle, applying Bragg's Law [40], one can obtain the interplanar distance between molecular lattices. The interplanar distance correlates to the crystalline structure of the studied specimen. Mathematically (Eq. 6), Bragg's Law states that:

$$2d \cdot \sin\theta = n\lambda \quad (6)$$

Where d is the interplanar distance, θ is the scattering angle, n is a positive integer and λ is the wavelength of the x-ray beam used. **Fig. 3.4** illustrates Bragg's diffraction, where d and θ are represented.

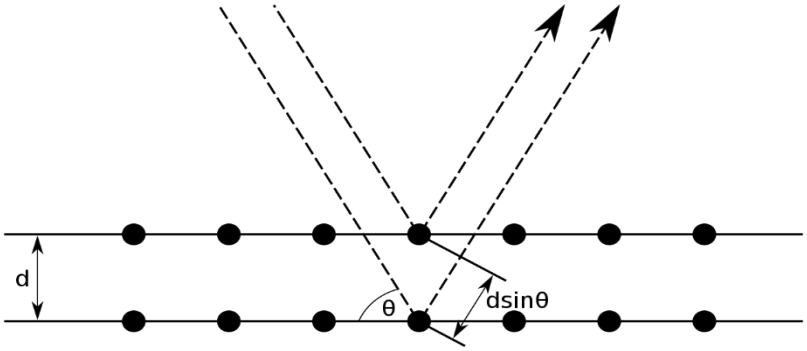

https://lampx.tugraz.at/~hadley/ss1/crystaldiffraction/atomicformfactors/powder.php.

Fig. 3.4 – Schematic representation of Bragg diffraction.

An XRD spectrum is a graph which depicts the relative intensities as a function of the detector's angle (2θ). Each crystalline structure has its own characteristic peak in a given location, the location also depends on the x-ray's wavelength. Therefore, viewing the spectrum, and with the help of a post-analysis software, one can identify the substance and crystalline structure that corresponds to each peak. It is important to keep in mind that not all peaks correlate to a pure substance, and that sometimes different substances have similar peak locations. Therefore, the resulting peaks are a convolution of the two (or more) peaks. For this reason, the peak's width is also a very important factor, and not only its intensity and location. **Fig. 3.5** shows the XRD spectrum of pure CVD-synthesized MWCNT.

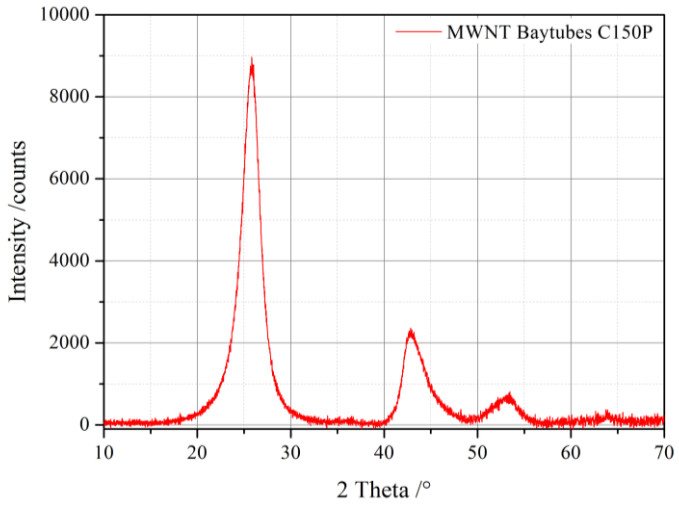

Fig. 3.5 - XRD spectrum of commercial MWCNT (Baytubes C150P).

3.5. Microhardness

Hardness [41] can be defined as the resistance a given material presents to localized plastic deformation. This characteristic is measured by forcing an indenter to plastically deform the specimen, and depending on the type of measurement and how the specimen responds, the hardness of the sample is obtained. Hardness provides important information since it can be correlated to wear resistance, tensile strength, and other physical characteristics.

Vickers hardness (ISO 6507) [42] is a very commonly used method to obtain a material's micro-hardness. In this test, a diamond indenter with a pyramidal-shape is used, resulting in an imprint with the shape of a rhombus. Once the imprint has been made, obtaining the hardness value is easily done by measuring the length of the diagonal of the rhombus. With this length, applying Eq. (7), the hardness is obtained.

$$HV = c \cdot \frac{F\,[N]}{d^2\,[mm]^2} \quad (7)$$

Where c is a constant with the value of 0.1891, F is the test force in Newton, and *d* is the length of the rhombus' diagonal (also known as surface area of indentation) in mm.

3.6. Raman spectroscopy

Raman spectroscopy [43]–[45] is a widely used optical technique which allows for a non-destructive investigation of structural properties such as: disorder, defects or strain in carbon nanostructures.

Raman spectroscopy uses a laser light (monochromatic) to irradiate a specimen. Through the interaction of this laser light with the vibrating molecules of the specimen, part of the irradiating light is scattered. The scattered light's color slightly varies from its original color. This is a direct effect of its interaction with the molecules that comprise the specimen. The instrument detects the difference in the scattered light's energy, compared to its original energy, and the Raman spectrum is generated. Most of the light that is used is unaltered, this is known as Rayleigh scattered light. However, when a ray of light loses or gains energy due to the interactions, it is called Stokes/Anti-Stokes scattering, which is what occurs when the light's color changes. When the irradiation light loses energy, the Raman scattering is called Stokes. When the light gains energy however, it is designated as Anti-stokes. This Raman scatter is generated as a consequence of photons exchanging part of their energy with the specimen's vibrating molecules. **Fig. 3.6** shows a graphical scheme of the laser light's energy before and after being scattered.

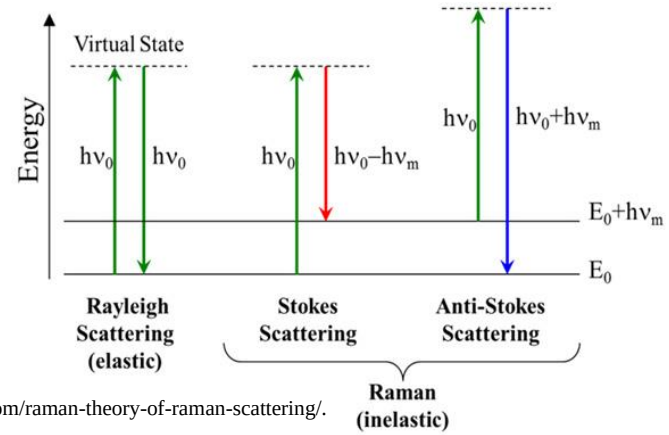

http://bwtek.com/raman-theory-of-raman-scattering/.

Fig. 3.6 - Scattered light scheme indicating Rayleigh, Stokes and Anti-Stokes scattering. E_0 represents the ground state.

The change in the light's energy depends on the frequency of each molecule's vibration, which is also linked to the atoms themselves and their bond type. When light atoms possess strong bonds (high frequency), the energy is significantly modified. Contrarily, heavier atoms with weaker bonds (lower frequency) generate smaller changes in the light's energy.

The Raman spectra obtained through this technique is a graphical depiction of the measurement, where the intensity of the scattered light is plotted on the y-axis as a function of the light's energy (frequency). The light's frequency is typically measured in wavenumbers, which is the number of waves per cm.

Some of Raman spectrum's key factors include:

- Raman shift and relative intensities of all the Raman bands of the material, which help to identify the material that is studied.
- Individual band changes: a band may shift, narrow, broaden or vary in intensity. This helps to reveal information about stress within the specimen, along with variations in crystallinity, and amount of material.
- Variation of spectra with position on the specimen, which reveals changes in uniformity of the material. This provides information on the specimen's homogeneity.

For carbon nanotubes in particular, the Raman spectrum is composed of four characteristic peaks in the case of SWCNT and three characteristic peaks in the case of MWCNT [46]–[50]. These peaks provide useful information based on their location and intensities.

The first peak is known as the Radial Breathing Mode (RBM). This peak is detected by exciting the sample with the laser light, causing the CNT to move radially. This peak may only be perceived in SWCNT and is located at low frequencies (below 200 cm^{-1}). The frequency of this mode is inversely proportional to the nanotube's diameter. Therefore, with different tube diameters, the location of the RBM differs. In the case of MWCNT, the different walls are bonded by weak Van-der-Waals forces, which attenuate the radial movement. Therefore, it is too weak to be detected, or the outer walls do not move altogether.

The second peak, first for MWCNT, corresponds to the D band. This peak indicates quantitatively the amount of defects present in the CNT. When a defect is

present in the CNT, such as a missing carbon atom, it is detected by the D band. For MWCNT, the D band is located at around 1340 cm^{-1}.

The third peak corresponds to the G band. This peak is an indicator of the crystalline structure of the CNT and is detected by a tangential vibration of the nanotube. In some cases, the G band may be split into G^+ and G^-. This occurs when the tangential vibration is confined in the circumferential direction of the tube. When this happens, the G^+ band represents the axial atomic displacement, while the G^- represents the circumferential atomic displacement. In general, observing the G band's location, it can be concluded that the higher the CNT's crystallinity is, the location of this peak will be closer to its theoretical location (between 1550 cm^{-1} and 1600 cm^{-1})[51].

Lastly, the fourth peak corresponds to the G' band. This G' band is a second harmonic of the D band caused by a secondary scattering. It represents the purity of the CNT and is located at about 2600 cm^{-1}.

These last three peaks are of utmost importance when characterizing MWCNT. However, their individual intensities are not of interest, their relative intensities provide more accurate. This is because Raman spectroscopy is a volume-sensitive technique. In other words, in order to obtain comparable results, the exact same amount of material must be irradiated in each measurement. If this is not the case, the two absolute measurements are not comparable. To overcome this disadvantage, the data must be normalized so that different measurements may be compared. Hence the importance of the relative intensities (ratio of intensities). Additionally, purity ratio is independent of the excitation energy that is used to acquire the Raman spectrum, while the G band is slightly more sensitive to energy changes. The two most important ratios are shown in the following two equations, Eq. (8) and Eq. (9):

$$defect\ ratio = \frac{I_D}{I_G} \tag{8}$$

$$purity\ ratio = \frac{I_{G\prime}}{I_D} \tag{9}$$

Eq. (8) represents the so-called "defect ratio" and is obtained by dividing the intensity of the D band by the intensity of the G band. Eq. (9) on the other hand, represents the "purity ratio" and is obtained by dividing the intensity of the G' band by the D band. The lower the defect ratio, the better the structural quality of the CNT, while purer CNT possess a higher purity ratio [46], [48], [49].

3.7. Surface Wettability: Sessile drop method

Perhaps one of the most important characterization techniques for the present work is determining the wettability characteristics of the CNT coatings applying the sessile drop method [52]–[56]. This method is of significant importance since it proved a quick, qualitative analysis of how different coatings interact with liquids. Therefore, a surface that does not interact, or slightly does so, with external liquids presents protection against water-based corrosive agents.

Utilizing this simple, yet powerful technique, one is able to determine how a given surface reacts when it comes in contact with a certain liquid. Depending on the values obtained from the sessile drop technique, one can establish a range that specifies if the specimen is hydrophilic, hydrophobic or even super-hydrophobic.

This method resides in measuring the angles θ_C that a drop, of a specific liquid with a specific volume, forms when it comes into contact with the surface of the studied sample. **Fig. 3.7** illustrates the contact angle measured for a droplet that partially wets a smooth solid sample. The figure also shows the different interfaces (solid-liquid, liquid-gas, and solid-gas). As it can be seen, θ_c is the angle formed between the solid-liquid and the liquid-gas interfaces.

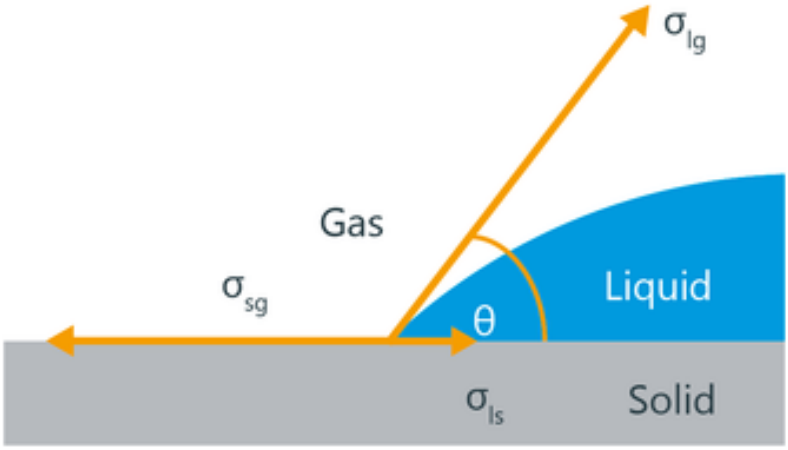

https://www.kruss-scientific.com/services/education-theory/glossary/contact-angle/.

Fig. 3.7 - Contact angle and corresponding interfaces of a liquid wetting a solid sample.

The contact angle θ_C can be mathematically obtained applying Young's equation, Eq. (10). This equation is a result of the equilibrium of all forces that act on the triple line.

$$\cos^{-1}\theta_C = \frac{\gamma_{SG}-\gamma_{SL}}{\gamma_{LG}} \quad (10)$$

The significance of this method, as it was already stated, is determining whether a solid sample is hydrophobic or hydrophilic. This information is a key factor for the topic

at hand, due to the enhanced anti-corrosive properties that a hydrophobic material presents against water-based corroding agents. If a corrosive fluid can't come into direct contact with the sample's surface, then the surface is effectively protected from corrosion. Therefore, using hydrophobic CNT coatings could potentially provide effective corrosion protection of steel surfaces.

The value of θ_C that can range from 0° to 180°. If 0° < θ_c < 90°, the surface is hydrophilic. In the extreme case of θ_c=0, the surface is known as super-hydrophilic. If 90° < θ_c < 180° the surface studied is hydrophobic. When $\theta_c \geq 150°$, the surface is considered super-hydrophobic.

Measuring the contact angle is a straightforward technique. The drop shape analyzer is used to deposit the droplet, observe the droplet on the specimen's surface, and determine its shape and the contact angle it forms. In the case that the contact area between the liquid and solid does not change during the measurement, the measurement is called static contact angle.

The measuring equipment required is quite simple. The drop shape analyzer consists of a camera and a light source, therefore it is an optical measurement. The camera is facing the light source. Between the two, the sample is places. Once the droplet has been deposited over the sample's surface, the drop will block part of the light from being picked up by the camera. Because of this, the camera shows a greyscale image where the droplet can be clearly identified. **Fig. 3.8** shows a schematic representation of how the drop shape analyzer works. Integrated in the drop shape analyzer, a software with different computational methods is able to determine the drop's outline. Choosing the most appropriate computational method (depending on the shape of the droplet different computational methods are able to model the contour best), the software calculates both contact angles, left and right.

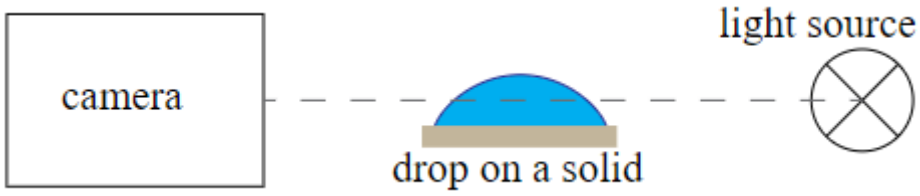

https://www.dataphysics-instruments.com/knowledge/understanding-interfaces/sessile-drop-method/.

Fig. 3.8 - Schematic setup of drop shape analyzer.

Depending on the surface's characteristics, the contact angle may or may not vary with time. For this reason, the measurement is taken 10 seconds after the droplet has been

deposited on the surface. It is of utmost importance to respect this set time and carry out all measurements in the same fashion in order to obtain comparable results. If the contact angle is measured straight after deposition, the obtained result will be higher than expected. If too much time is allowed to pass, the angle will be lower. Therefore, producing a larger standard deviation, and introducing measurement errors and inconsistent results.

If it is desired, when the surface effectively absorbs the fluid, one may also study how the wettability characteristics varies with time. This is simply done by measuring the contact angle a droplet forms with the surface over time.

The wettability measurements are to be conducted under the standards presented by ASTM [57] in order to obtain comparable results. This standard states the type of liquid that must be used and the volume that the droplet must possess. According to the aforementioned standard, deionized water is sufficient and the droplet volume must be 3 µL. The latter condition is to ensure that the measurement is not altered by the effects that gravity has on the droplet. If the droplet volume is increased, gravity will affect the droplet. This will cause the droplet to be more oval-shaped and in addition, and if the volume of the droplet is increased sufficiently, the triple point will begin to move. This oval-shaped droplet generates an inaccurate contact angle measurement. As a side effect of this low volume of water (3 µL), the droplet "sticks" to the syringe and does not fall onto the surface of the specimen. For this reason, the drop shape analyzer's stage must be lifted until the specimen's surface comes into contact with the droplet. If the surface interacts sufficiently with the droplet, the droplet will adhere to the surface and the contact angle can be measured normally. If the specimen's surface does not interact with the droplet on the other hand, the droplet will remain attached to the syringe. This behavior is characterized as super-hydrophobic.

Young's equation (Eq. 10) is accurate when the surface in question is ideal, which means flat, rigid, perfectly smooth and chemically homogeneous [52]. In the case of non-ideal solid surfaces, two other models need to be considered: Wenzel and Cassie-Baxter [58]. These two principles are of great importance for the present study for the following reasons:

- The steel substrates have a cylindrical shape.
- The coating surface is neither smooth nor flat.
- The obtained coatings consist of a porous CNT network.

Both Wenzel and Cassie-Baxter can be used to predict the wetting characteristics of non-ideal surfaces taking into consideration the apparent contact surface. However, these principles consider two different wetting situations. Wenzel governs when the surface has a relatively high roughness. **Fig. 3.9a** illustrates a rough surface that follows a Wenzel wetting behavior. On the other hand, Cassie-Baxter describes the wetting behavior of a super-hydrophobic surface. In this case, the fluid does not come into contact with all of the real surface of the substrate. The surface can be considered as smooth since the liquid traps the air pockets between the surface roughness or pores and the liquid [52], [58]. Therefore, the liquid only touches the crests of the surface's roughness or inhomogeneities, as **Fig. 3.9b** illustrates.

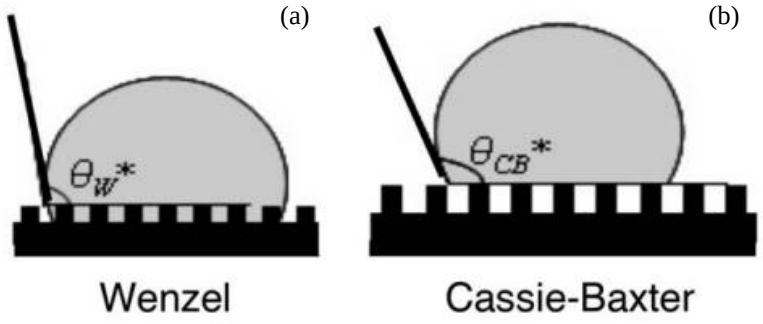

S. Ok, J. Sheets, S. Welch, S. Kaya, A. Jalilov, D.R. Cole, "Tuning hydrophobicity of a fluorinated terpolymer in differently assembled thin films.", J. Polym. Sci. B., 2017.

Fig. 3.9 - (a) Wenzel wetting regime; (b) Cassie-Baxter wetting regime.

4. Experimental Section

4.1. Rod immersion testing

As a preliminary analysis, the ends of the rod (thread, wrench grip and part of the body) were subjected to an immersion test, so as to assess qualitatively their intrinsic corrosion behavior in an unprotected state. Consequently, the fragments were completely submerged in two liters of deionized water at room temperature. The main idea behind this is to quantify the weight lost by the rod due to corrosion. This is a simple yet effective way to study how the steel behaves when in presence of a harsh, corrosive environment.

As soon as half an hour after submerging the rod, visible changes could be observed. Small orange spots could be observed on the polished section of the rod. The thread and sandblasted section however, seemed still unaltered after the initial visual inspection. Further on, after one hour of the rod being submerged, most of the rod seemed affected.

24 hours after the initial submersion, the whole rod was already covered by rust. Only some small regions of the thread seemed unaffected. The rod was removed from the container, rinsed with deionized water and dried with compressed air (8 bar). After weighing, no mass changes could be measured. Subsequently, the rod was placed in the container again with two more liters of fresh deionized water.

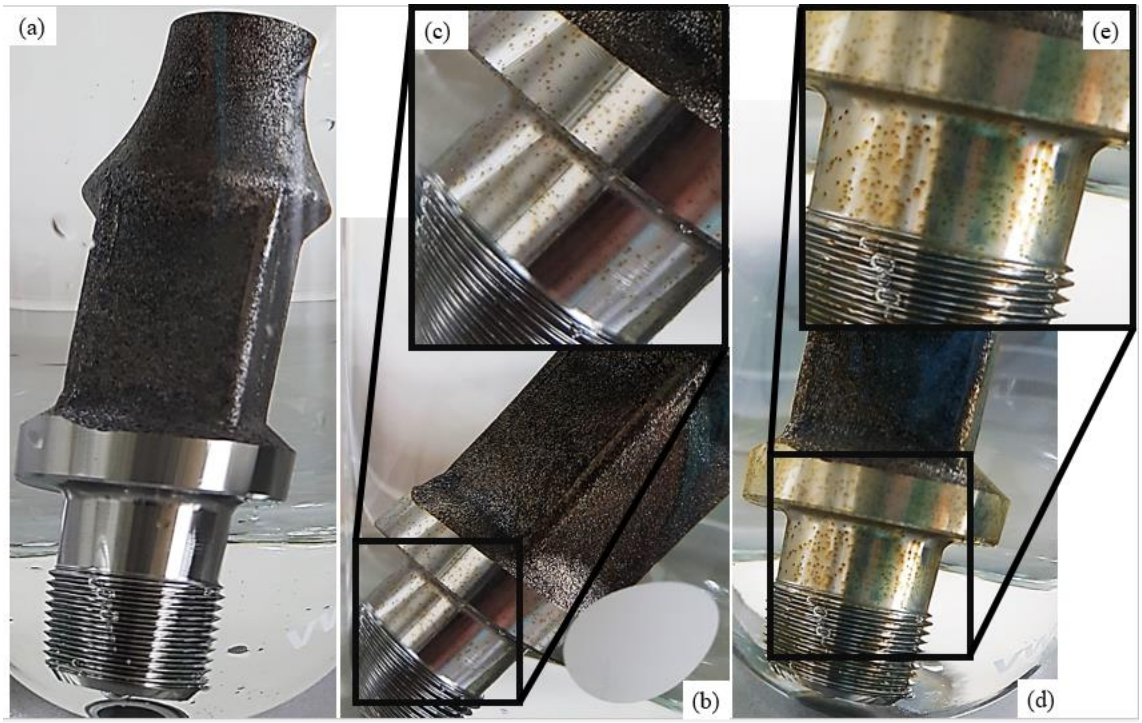

Fig. 4.1 - **(a)** Rod immediately after submerging; **(b)** Rod after 30 minutes in water; **(c)** Zoom of affected areas in rod after 30 minutes; **(d)** Rod after 1 hour in water; **(e)** Zoom of affected area in rod after 1 hour.

Since after one day no changes were seen in the rod's weight, the rod was left in the water for six days, following the above mentioned procedure. As before, no changes in the rod's weight could be perceived. As for seven and eight days submerged, no apparent changes to the rod's appearance or weight could be noticed. However, after removing and rinsing out the rod, the appearance of it had indeed changed. It is now permanently stained with orange spots, and the regions where it was polished are no longer shiny. These regions present optically a shade of dark gray.

Since as already mentioned, changes in the rod's weight were negligible, the rod was re-submerged and left for an additional seven days (for a total of fifteen days submerging), and later for an additional eleven days (for a total of twenty-six days submerging). As before, no changes in the rod's weight are observed. Its appearance however has been significantly modified. The rod's body presents now a completely dark gray shade and is mostly stained with orange, even regions of the thread. The results observed for short-term and long-term submerging are shown in **Fig. 4.1** and **Fig. 4.2**, respectively.

Fig. 4.2 - **(a)** Rod in-water after 6 days; **(b)** Dried rod after 7 days; **(c)** Dried rod after 8 days; **(d)** Dried rod after 15 days; **(e)** Dried rod after 26 days; **(f)** Recently removed rod after 15 days.

4.2. Sample preparation

Two types of samples were obtained from commercial sucker rods that are extensively used at oil extraction sites.

1. From the cylindrical part of the rod, a thin cross-section was cut, and this cross-section was cut in half. As **Fig. 4.3a** shows.
2. From the cylindrical part of the rod, a thicker cross-section was cut, and this cross-section was cut in half. As **Fig. 4.3b** shows.

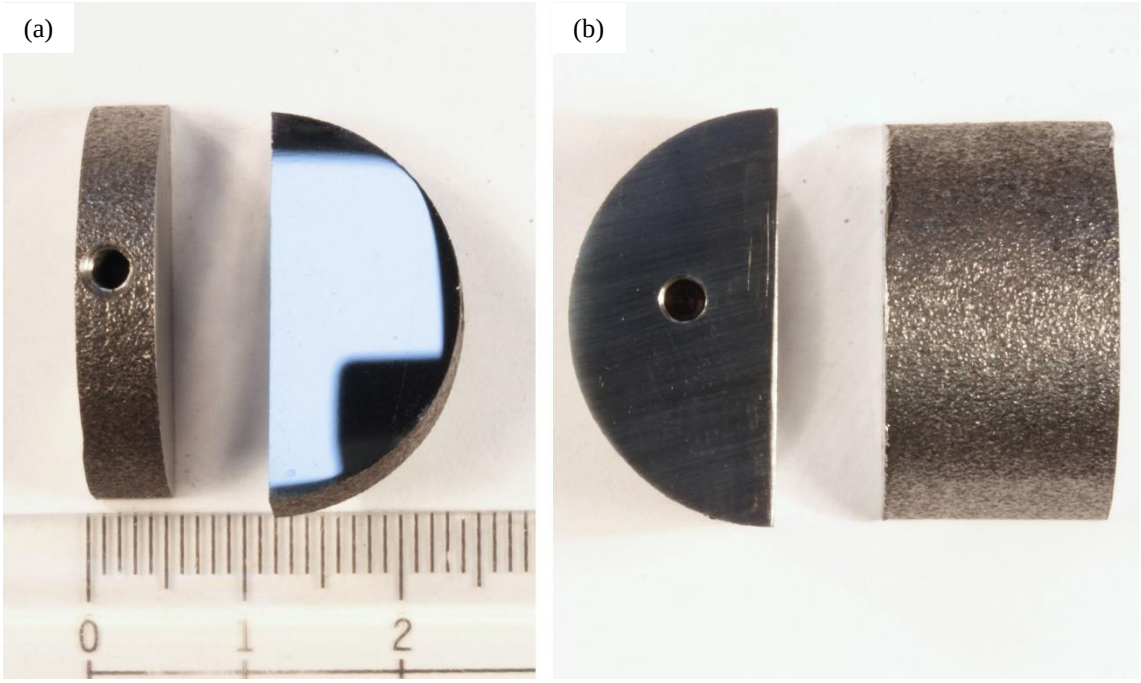

Fig. 4.3 – **(a)** Polished samples type 1; **(b)** Samples type 2.

The type 1 samples are ground with a silicon carbide paper from a grit P180 up to P1200 [59] (average 15.3 µm in surface particle diameter). Afterwards, they are polished with diamond suspension (average particle size of 1 µm), since they will be coated on the flat, smooth, polished surface. The type 1 sample shown in **Fig. 4.3a** has underwent this preparation process. The type 2 samples, do not require further preparation, since they are meant to be coated on the curved, rough surface.

The first developmental/optimization stage will be performed on the type 1 samples. Once the optimal parameter configuration and methodology have been determined, the selected process will be applied to the type 2 samples.

4.3. Pre-coating surface cleaning

To make sure that the samples that will be coated (and the counter electrodes) are completely clean, they are subjected to a procedure that consists of 3 cycles in an

ultrasonic bath. They are soaked in three different cleaning media, namely: cyclohexane, acetone and isopropanol (IPA). Between each cleaning step, the samples are rinsed with deionized water. After being cleaned with IPA, they are dried using compressed air (4 bar) and encased in aluminum foil to protect them from environmental oxidation prior to the coating process. Since the steel is very prone to chemical reactions (e.g. oxidation), the cleaning process should be kept relatively short (5 minutes per medium). Furthermore, the time spent between each cycle must be reduced as much as possible in order to minimize the time the samples are exposed to the environment. This cleaning procedure has been proposed by MacLucas et al. [2], where they kept the samples in the bath for 10 minutes per medium. However, this rendered oxidized samples, which meant that they required to be re-polished and re-cleaned. From this experience, the time spent per medium was cut in half. This way, the oxidization was reduced considerably, nearly resulting in non-oxidized samples.

4.4 Colloid preparation

After the samples have been polished and clean, the CNT colloidal dispersion must be prepared. This is done following the report by MacLucas et al. [2]. These processes are very important steps to ensure a proper coating, and they will be described thoroughly.

The concentrations used for the colloidal dispersion depends on the additive used. First, concentrations and procedures for magnesium nitrate hexahydrate [$Mg(NO_3)_2 \cdot 6H_2O$ henceforth *Mg-Nit*] as an additive will be explained. As reported by MacLucas et al. [2] the solution concentrations for Mg-Nit are:

- 80 ml of IPA.
- 0.025 mg of Mg-Nit per ml of IPA = 2 mg Mg-Nit.
- 2 ml of deionized water.
- 0.1 mg of CNT per ml of IPA = 8 mg CNT.

The concentration of Mg-Nit is key since if this value is not met accurately, the CNT will coagulate. On the other hand, if the concentration is too low, dispersion quality will be significantly affected. Therefore, when preparing the disaggregation, special attention must be paid to the Mg-Nit concentration.

When a CNT coating is produced utilizing Mg-Nit as an additive, an additional holding layer [60] is formed directly onto the surface of the deposition electrode. This

holding layer, which is comprised of $Mg(OH)_2$, improves the adhesion between the deposited nanoparticles and the substrate. It is for this reason that the 2 ml of deionized water are added, since it promotes the formation of this holding layer. The following chemical equations represent the reactions that takes place during the formation of the holding layer [61].

$$NO_3^- + H_2O + 2e^- = NO_2^- + 2OH^- \quad (11)$$

$$2H_2O + 2e^- = 2OH^- + H_2 \quad (12)$$

$$Mg^{2+} + 2OH^- = Mg(OH)_2 \quad (13)$$

The main challenge with pristine CNT is dispersing them correctly in a suitable liquid medium, due to their predisposition to re-agglomerate. When the CNT are chemically functionalized [62], their dispersability increases due to the electrostatic repulsion given by superficial functional groups with the same effective electrical charge. However, the chemical functionalization process is complex and involves an additional step in the coating process, and usually degrades the structural integrity of the CNT. Therefore, for this application it is more convenient to disperse pristine CNT than functionalized CNT. It can be assumed that the pristine CNT are chemically inert due to a lack of free (dangling) bonds, which leads to a neutral surface charge. However, it has been studied previously and proven that the pristine CNT used have a certain degree of functionalization due to the fact that they are synthesized by a CVD process [2]. These CVD-grown CNT possess carboxy groups, which contribute oxygen. This oxygen content, although very low, is enough for the CNT to be properly dispersed in the chosen medium. Without these oxygen-containing functional groups present in the pristine CNT, the dispersion process would not be possible without a previous functionalization process.

As consequence of the curved surface the CNT possess, a phenomenon known as pyramidalization occurs. Because of the curvature, the outer π-bonds are weakened, while the inner π-bonds are strengthen. This phenomenon differentiates the behavior that CNT's surface possess as opposed to other flat carbon allotropes, e.g. graphite, graphene.

For the case of triethylamine ($C_6H_{15}N$, henceforth *TEA*) as an additive, the concentrations used are:

- 80 ml of IPA.
- 0.125 ml of TEA per ml of IPA = 10 ml TEA
- 0.1 mg of CNT per ml of IPA = 8 mg CNT.

For both cases, the same instrumentation is required:

- Basic lab equipment such as beakers, pipettes, graduated cylinders, etc.
- Shear mixer or homogenizer.
- Ultrasonic bath.

4.4.1. Dispersion of CNT in a solvent with Mg-Nit as an additive

To start off the dispersion process, 80 ml of IPA are measured and placed in a glass beaker, along with 2 ml of deionized water. After 2 mg of Mg-Nit have been weighed, it is added to the beaker and it is placed inside an ultrasonic bath for 3 minutes (Bandelin Sonorex Super RK 514 BH, 33 kHz, 860 W). This is done to procure a homogeneously dispersed solution of Mg-Nit in IPA. The following step is the addition of 8 mg of CNT to the solvent. In order to disperse the CNT properly, the content of the beaker is subjected to a dispersing instrument (IKA T25 digital ULTRA-TURRAX). The instrument is set at 5000 rpm for 5 minutes. The last step in the dispersion process is 10 minutes of sonication in the same ultrasonic bath. It is important to keep in mind that the dispersion coagulates over time. Therefore, if the disaggregation is unutilized for a certain period of time, before it can be reutilized for a coating process, it must be re-dispersed.

4.4.2. Dispersion of CNT in a solvent with TEA as an additive

The process is essentially the same as previously described for the case of the Mg-Nit additive. 80 ml of IPA are measured and placed in a beaker, followed by the addition of 8 mg of CNT and 10 ml of TEA. The content of the beaker is subjected to the dispersing instrument set between 4800 and 5000 rpm for 5 minutes and lastly it is sonicated for 10 minutes. Once this is done, the dispersion is apt for a coating process.

In this case, the dispersion tends to coagulate at a much slower rate compared to the Mg-Nit dispersion. Therefore, this disaggregation does not require frequent re-dispersions. When using Mg-Nit as an additive, the concentration of this substance used is critical. Lack of sufficient Mg-Nit would not properly disperse the CNT, and an excess amount of this substance turns the disaggregation unstable. Therefore, since the amount of Mg-Nit used is very few (2 mg), it is quite difficult to add the exact same amount every time a disaggregation is prepared. This makes the Mg-Nit dispersion more unstable compared to the TEA dispersion.

4.5. Deposition

4.5.1. Process

After the samples and the colloidal dispersion have been prepared, the coating process begins. To do so, the power source must be turned on and two samples must be connected to the electrodes, one will be the deposition electrode and the other will act as a counter electrode. The electrodes are held by two clamp holders.

Depending on the additive used for the dispersion, is which electrode acts as the deposition electrode and which electrode acts as the counter electrode. In the case of Mg-Nit, the deposition occurs over the negative electrode (cathodic deposition). The deposition occurs on the negative electrode due to de magnesium ions (Mg^{2+}). These ions attach themselves to the carboxylate groups found in the pristine CNT, giving them a positive superficial charge. For TEA on the other hand, the deposition occurs on the positive electrode (anodic deposition). This is a consequence of the deprotonation of the carboxylate groups [63]. Therefore, it increases the negative surface charge of the CNT. It must be kept in mind on which electrode the deposition occurs when placing the samples, this way the desired sample is coated correctly.

After the parameters have been set on the power source (applied voltage, maximum current, maximum power and deposition time), both samples are dipped inside the colloidal dispersion. When doing this, the samples must be completely covered by the fluid in order to ensure that it is coated entirely. However, care must be taken to make certain that the clamps themselves do not touch the fluid. If this is not the case, the clamps will be coated as well. Once all these steps have been performed, the deposition process may begin. Due to the configuration of the power source, the set value of the voltage is first achieved after a 30 seconds ramp up. For this reason, the power supply functions for an additional thirty seconds from the set time.

As it was explained in *section 2.2.5*, when the electric field is applied, the dispersed nanoparticles begin to move due to electrophoresis. For this particular reason, the applied voltage is a very important factor. The electric field's intensity depends upon the applied voltage, while the electrophoretic motion depends on the electric field. Therefore, a larger applied voltage produces a stronger electric field which drives the dispersed nanoparticles to move towards the electrode through electrophoresis. This motion must be strong enough to transport the nanoparticles from their original location in the disaggregation towards the electrode, by overcoming three strong counterforces, namely: the fluid drag force (viscosity of the liquid medium), the gravitational interaction

(particle's weight) and the Brownian motion of the particles in the fluid. **Fig. 4.4** shows a simulation of an electric field generated by a pair of charged plates, which represent the two electrodes. **Fig. 4.5** shows the electrode setup for samples type 2.

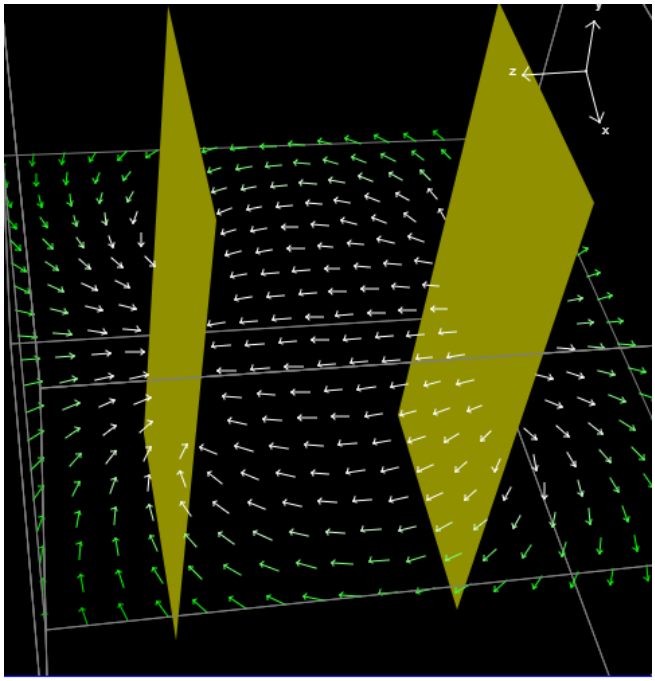

https://www.falstad.com/vector3de/.

Fig. 4.4 - Simulation of electric field generated between two parallel plates.

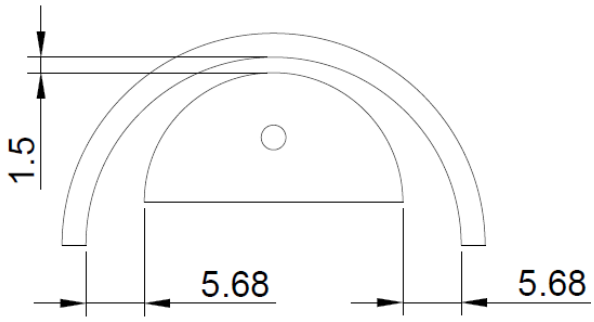

Fig. 4.5 – Electrode setup for samples type 2.

The other important factor to keep in mind is the distance between electrodes. Since the electromotive force imposes a movement on the dispersed particles, if the distance that the particles must travel is too large, the electric field that generates the electrophoretic motion must be increased. This is because the particle must overcome more drag resistance along the greater electrode distance. On the other hand, as it is noticeable from the figure and depending on the electrode's inter-distance, the edges of the electrode might concentrate electric field and may lead to inhomogeneity in the

coating thickness. This effect becomes even more critical if the distance between electrodes is small. Therefore, the distance set for the deposition process is going to affect the outcome in a very important manner.

Deeply related to these two parameters is the size of the nanoparticles, or the amount of agglomerates present in the dispersion. The larger the particle size or the agglomerate, the more it is going to weigh. Consequently, it will require a stronger electric field to impose a larger electrophoretic motion force for such a heavy particle. To avoid the need of an excessively large electric field, when dispersing the nanoparticles, the agglomerate quantity must be reduced as much as possible, without compromising their structural integrity. Larger agglomerates significantly affect the CNT physical properties. Therefore, reducing the amount of agglomerates is always one of the main goals.

After the deposition time has concluded, the power source ramps down the applied voltage from the set value to 0 V. Subsequently, the samples can be withdrawn from the liquid medium and the post-deposition process begins.

4.5.2. Coatings nomenclature

All the preliminary coatings done can be categorized in three major groups. The category a sample falls in depends exclusively on the additive that was used for the colloidal dispersion. **Table 4.1** describes the names given to each category and what additive corresponds to each category. All the preliminary coatings carried through have been applied on sample type 1. Once the coating procedure was optimized, this exact coating procedure was applied to coat samples of type 2.

Table 4.1 - Coating categories for preliminary type 1 samples.

Acronym	Additive
Mg-Nit	Magnesium Nitrate Hexahydrate
TEA	Triethylamine
DD	Double deposition

The first two categories are self-explanatory. The third category corresponds to a double deposition. DD coatings are carried out by depositing a coating of Mg-Nit, followed by an appropriate post-deposition process, and then applying a TEA coating over the Mg-Nit deposition. After the TEA coating is applied over the Mg-Nit, the sample is once again subjected to the corresponding post-deposition process.

This double deposition method was selected because it is believed that it could solve the individual problems that the Mg-Nit and TEA coatings intrinsically possess. Due to the formation of a holding layer between the substrate and the CNT particles in the Mg-Nit coatings, it is applied directly over the substrate as it has been proven in previous works to have better adhesion compared to TEA coatings. Over this Mg-Nit coating, the TEA coating is applied to improve the wetting characteristics of the coating, since the Mg-Nit coating is hydrophilic but the TEA coating is hydrophobic (and even shows near super-hydrophobic behavior in certain cases). With these two coatings combined, the coated sample might ideally have admissible adhesion and extraordinary wetting characteristics.

With a procedure and some selected deposition parameters, type 2 samples are coated. The parameters where selected based on prior coatings done on samples type 1 and the subsequent contact angle measurement. The parameters that produce the coatings with the best results (regarding wettability) are maintained and applied over samples type 2 in order to try to duplicate the results on these other samples. However, due to the geometrical and superficial differences between the two sample types, the optimal parameters vary slightly.

As done for **Table 4.1**, **Table 4.2** describes the names given to each sample. The name given depends on the category that best describes the sample.

Table 4.2 - Coating categories for samples type 1 and 2.

Acronym	Additive	Post-process
MFxy	Magnesium Nitrate Hexahydrate	Cook in crude oil
TFxy	Triethylamine	Cook in crude oil
MRxy	Magnesium Nitrate Hexahydrate	Cook in crude oil
TRxy	Triethylamine	Cook in crude oil
DDFy	Double deposition	None
DDFCy	Double deposition	Cook in crude oil
DDRy	Double deposition	None
DDRCy	Double deposition	Cook in crude oil

All categories that include an F correspond to samples type 1, while all categories that include an R correspond to samples type 2. Also, the M represents a Mg-Nit-based coating, while the T represents a TEA-based coating. As before, the DD categories

correspond to double coatings where a Mg-Nit coating is done over the substrate's surface and a TEA coating is done over the Mg-Nit coating. The letter x on the category name corresponds to a number. This number indicates the amount of time (in minutes) that the voltage was applied during the deposition process. On the other hand, the letter y on the category name corresponds to the sample number, since more than one sample were coated following the same procedure with the same coating parameters.

As will be explained in *section 4.6.4* all samples, except for samples DDF and DDR, underwent an additional post-deposition process.

4.6. Post-deposition process

The post-deposition process consists of rinsing the coated sample in IPA followed by an immediate drying step. The sample must be rinsed to make certain that any residual additives are removed from the surface of the coating. If this step is not taken, the residual additives on its surface may affect the behavior it presents when measuring wettability. It is especially important to rinse the TEA coatings, since the TEA completely changes the wettability characteristics of the surface. After rinsing the samples, they must be dried. Various post-deposition processes have been attempted in order to obtain the best results, producing the least amount of damage possible to the coatings.

4.6.1. First optimization cycle

After the samples were withdrawn from the liquid medium, they were immersed in a beaker with IPA for two minutes. Once removed from the IPA the coated sample was dried using compressed air at 4 bar. While drying, the samples were kept as far away as possible from the nozzle to avoid any damage. However, the coatings were affected nonetheless, especially the TEA coatings.

4.6.2. Second optimization cycle

The rinsing step is identical to the first attempt, two minutes immersion in IPA. Since IPA is highly volatile, the compressed air was substituted by hot air blowing. It was thought that the lower air pressure, and the higher temperature would effectively dry the sample without damaging the coating. However, this attempt also affected the coating's integrity, especially the TEA coatings. This alteration is visualized by the partial removal of the coating obtained. Although the removal is localized and does not seem severe, it

could potentially affect the coating's corrosive protection. These alterations are shown in **Fig. 4.6**, with some defects produces by this second cycle highlighted with arrows.

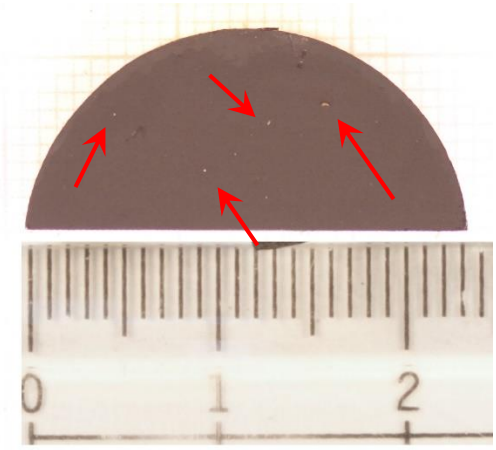

Fig. 4.6 – Overview of the damaged coating by second cycle.

4.6.3. Third optimization cycle

On the first two attempts, when immersing the coated sample in IPA, part of the coating was removed. As soon as the coating was exposed to the IPA, it was quite evident that some CNT particles became loose and remained in the liquid once the samples were removed. In addition, when removing the samples from the colloidal dispersion after the coating process, part of the coating was removed by a dragging effect (predominantly the outermost CNT). For these two reasons, once the coating was completed, the voltage was re-applied for one additional minute. As soon as the voltage reached its set value, the samples were removed from the colloidal dispersion and immediately immersed in IPA. Once in IPA, the power supply was paused, the samples were left in IPA for two minutes. After the two minutes were up, the power supply was un-paused and the samples were removed from the IPA and left until the power source stopped.

As an improvement on the drying process, after rinsing the samples, the coated one is placed on a watch glass and placed inside an oven to dry. The coated sample remains inside the oven for 5-10 minutes at a set temperature of 80 ºC to ensure that all remains of the solvent are evaporated.

This third attempt has proven to be successful at producing the least amount of damage to the coating. Therefore, it is selected as the most suitable post-deposition process.

4.6.4. Crude oil post-treatment (cooking)

This post-deposition process came into being as a test that corroborated that the coatings could withstand the standard operational conditions. Here, the samples are placed inside a beaker that contains crude oil, which is then placed inside an oven (Heraeus Instruments) at 80 °C for a prolonged period of time (minimum of 24 hours). The samples are completely covered by the oil. After they have been in the oven for the chosen period of time, they are withdrawn from the oil and left in the oven to dry. The time it takes the samples to dry is generally an additional 24 hours when placed at 80 °C, or about four hours for 200 °C.

As it was mentioned before, this process was intended as a confirmation that the coatings could endure the operational conditions. Not only did the coatings tolerate these conditions, but their wetting characteristics and the coating's adhesion were significantly enhanced. The wetting characteristics enhancements will be discussed more in depth in *section 5.2.4*. As a consequence of said enhancements, this process was adopted as an additional post-deposition process for some samples. It must be highlighted that this process is conducted after the "third optimization cycle" process described in the section above.

4.7. EPD parameter optimization

As it was discussed in *section 2.2.5*, there are a number of parameters that may be modified in the deposition process that produce considerably different coatings. The most relevant parameters are:

- Distance between electrodes.
- Applied voltage.
- Deposition time.
- Particle size.
- Particle and additive concentration.

Of these five parameters, only the first three will be analyzed, since they are easily modified and controlled. The particle size is very hard to modify and to reproduce the same results continuously due to the use of pristine CNT, their agglomeration and the dispersion process. The particle and additive concentration has great influence on the deposition process. The additives must be added in the correct proportions, otherwise the dispersion will be very unstable. Moreover, particle concentration must be kept at an

optimal level; otherwise, the resulting dispersion would be unstable. For these two reasons, these parameters are not modified. Their values are maintained constant for all coatings. On these grounds, particle and additive concentrations are kept as reported by MacLucas et al. [2].

The parameters and configuration reported in [2] are taken as parting ground. Once results are reproducible and studied (measuring contact angle), decisions will be taken in accordance to the results obtained, relating to how these three parameters will be modified.

As a work hypothesis, the theoretical process described by Hamaker et al. (through Hamaker's model) are optimized empirically, manually varying the different parameters and observing the results obtained. Therefore, finding the optimal parameters is carried out empirically on samples of type 1. This is carried out by varying one of the parameters and keeping the other two constant for both additives. The coatings obtained are later studied by measuring the coating's contact angle with water. The pair of samples that produce the best results correspond to the new set value of the variant parameter. This process is thoroughly explained for each parameter in the following sections.

All the contact angle measurements that were conducted in order to select the optimal parameter are later discussed in *section 5.2.4*.

4.7.1. Influence of the inter-electrode distance

The initial electrode distances were selected arbitrarily and set at 3.5, 2.5 and 1.5 cm. The latter corresponds to the smallest electrode distance attainable by the EPD cell (due to geometrical restrictions). In total, six samples are coated. **Table 4.3** depicts characteristics of the aforementioned samples.

Table 4.3 - Coated sample characteristics varying electrode distance.

Sample	Additive	Electrode dist. /cm	Voltage /V	Deposition time /min
Mg-Nit 1	Mg-Nit	2.5	150	5
TEA 1	TEA			
Mg-Nit 2	Mg-Nit	3.5		
TEA 2	TEA			
Mg-Nit 3	Mg-Nit	1.5		
TEA 3	TEA			

Of these six samples, Mg-Nit 3 and TEA 3 produce the best results. For this reason, the optimal electrode distance is set to the smallest possible, 1.5 cm.

These results are explained (as previously discussed) by the simple fact that a larger electrode distance equates to a larger distance that the CNT particles must travel. With a given, constant voltage, the applied force on the particles is always the same. If the same force is applied in all three situations, but the distance that must be travel is larger, fewer particles will effectively reach the surface of the deposition electrode. Therefore, the smallest distance between electrodes produces the best coating with a given deposition time and applied voltage. It is noteworthy though that even for the closest inter-electrode distance, the edge effect on the homogeneity is not observable.

4.7.2. Influence of the deposition time

To begin with, three deposition times are selected based on past experiences, 1 minute, 2 minutes and 5 minutes. **Table 4.4** summarizes the parameters used in all six depositions.

Table 4.4 - Coated sample characteristics varying deposition time.

Sample	Additive	Deposition time /min	Voltage /V	Electrode dist. /cm
M1	Mg-Nit	1	150	1.5
T1	TEA			
M2	Mg-Nit	2		
T2	TEA			
M3	Mg-Nit	5		
T3	TEA			

As expected, a thicker coating is obtained with a longer deposition time. It is for this reason that longer deposition times were tested, since it was believed that a thicker coating offered the steel more protection. However, with deposition times surpassing the five minute mark, the structural integrity of the coating is jeopardized. In other words, when the coated sample was removed from the colloidal dispersion, part of the coating broke off due to a dripping and dragging effect. It seems that when the coating is too thick, the Van-der-Waals forces that bond the CNT particles together are not strong enough to overcome said effects and the particles' own weight. Additionally, a thicker coating equates to more material used. It is not desired to use an amount of material that

is not strictly necessary. Therefore, for all these reasons, the deposition time will never surpass five minutes.

Currently, the optimal deposition time has not been established. However, after measuring contact angle, one thing can be highlighted: the optimal deposition time varies between samples and depends exclusively on the additive used. For Mg-Nit depositions, a thicker coating is desired to obtain better wetting characteristics. Therefore, a longer deposition time is required. On the other hand, for TEA depositions, the thickness of the coating is not important. It is only necessary that the coating is sufficiently thick to completely cover the entire surface of the substrate. Ergo, shorter deposition times may be exploited.

Having said this, the optimal deposition times selected are:

- For Mg-Nit coatings: 3 and 5 minutes.
- For TEA coatings: 2 and 3 minutes.
- For DD coatings: 3 minutes for Mg-Nit and 2 minutes for TEA.

In the case of TEA coatings, fewer than 2 minutes does not produce a uniform coating that covers the whole surface, leaving parts completely uncoated. This is not desired since the contact angle in these spots are equal to the exposed steel. A minimum of two minutes deposition time must be utilized. For Mg-Nit coatings however, three minutes is the least amount of time that may be utilized since coatings produced with shorter deposition times are not sufficiently thick. In order to avoid unnecessarily thick coatings, for DD coatings the individual deposition times of Mg-Nit and TEA are kept to the least amount possible.

4.7.3. Influence of the applied voltage

The final parameter that can be modified is the applied voltage. This parameter is complicated since it changes the motion force that is exerted on the CNT particles. And since the other two parameters have already been optimized for a given value of applied voltage, if this last parameter is modified, it will also modify the results of the other two parameters. In other words, if a larger voltage is applied, the distance between electrodes may be increased given that the force is stronger. Or, in the same fashion, if the applied voltage is increased and the electrode distance is maintained, the deposition time must be decreased if the same results are desired. Both larger and smaller voltages were tested all the same, parting from 150 V. **Table 4.5** summarizes all parameters.

Table 4.5 - Coated sample characteristics varying the applied voltage.

Sample	Additive	Voltage /V	Deposition time /min	Electrode dist. /cm
Mg-Nit 4	Mg-Nit	100	5	1.5
TEA 4	TEA		3	
Mg-Nit 3	Mg-Nit	150	5	
TEA 3	TEA		3	
Mg-Nit 6	Mg-Nit	200	5	
TEA 6	TEA		3	

Utilizing the other two parameters with their optimized values, and as expected, the best results obtained correspond to an applied voltage of 150 V. A lower voltage produces thinner films, and a higher voltage produce significantly thicker and irregular coatings. The thinner coatings are not sufficient to fully protect the substrate, whereas thicker coatings unnecessarily utilize a larger amount of material. Therefore, the voltage used is maintained at the initial value of 150 V.

4.8. Cooking optimization

It was found that the post-deposition process of cooking the coated samples in crude oil at 80°C significantly improved the coating's adhesion to the substrate and its wetting characteristics. To optimize the cooking time required, various samples were coated and cooked for different periods of time. Afterwards, contact angle measurements were conducted to identify empirically which samples produced the best results. This process is described in the following sections.

4.8.1. Sample coating and cooking

In the same manner as the deposition time, the cooking time required for each coated sample differs based on which additive was used for the coating process (*section 4.7.2*). To obtain the ideal cooking time for a given sample, twenty-four samples were coated with differing thicknesses and additives, and cooked for a different amount of days. The details of these 24 coated samples are shown in **Table 4.6**.

Table 4.6 - Different samples used to determine optimal cooking time.

Sample	Additive	Deposition time /min	Cook time /days
M11	Mg-Nit	1	1
M12			2
M13			3
M14			4
M21		2	1
M22			2
M23			3
M24			4
M51		5	1
M52			2
M53			3
M54			4
T11	TEA	1	1
T12			2
T13			3
T14			4
T21		2	1
T22			2
T23			3
T24			4
T51		5	1
T52			2
T53			3
T54			4

All 24 coatings were done utilizing 150 V, 1.5 cm distance between electrodes, and 10 minutes drying time after coating. The main difference between the samples is the additive used; half of them were coated using Mg-Nit and the other half using TEA. For the 12 Mg-Nit samples, 4 were coated for 1 minute, 4 more were coated for 2 minutes and the remaining 4 were coated for 5 minutes. Likewise for the 12 TEA samples.

All 24 samples were placed in the oven at the same time. All of which were completely immersed in crude oil, with a set temperature of 80°C. Each day, a different batch of samples was removed from the oven. The first day, one of each samples were removed from the oven (M11, M21, M51, T11, T21, and T51). The next day, a second batch was removed (M12, M22, M52, T12, T21, and T52). This procedure was repeated two more days until all samples have been removed from the oven.

After all samples have been cooked, they were once again placed inside the oven. This time left vertically and without the oil at 200°C for approximately 4 hours, so as to allow them to completely dry and remove any excess oil that remained. This drying process is of great significance, since it significantly affects the coatings performance when related to its wetting behavior. This will be explained in further detail in the following section.

4.8.2. Cooked sample study

Once all samples were completely dried, their wetting behavior was studied. This study was conducted to decide the ideal cook time for each additive. Whichever sample presents the best wetting characteristics in sessile drop tests (highest contact angle), is considered to be the ideal cook time for the given additive. The specifics of the sessile drop tests will be further presented in *section 5.2.4*. This section is dedicated exclusively to presenting the optimal cooking time for Mg-Nit coatings and TEA coatings.

From this study, three very important tendencies were notices:

4. On all the Mg-Nit-based coatings, the sample's wetting behavior improves significantly with the coating's thickness. In other words, the samples do not require extensive cooking times. A short cook time of 1 day is sufficient to improve the wetting behavior. It is very important to highlight that however short the cooking time is, the samples must be cooked in order to obtain said enhanced properties.
5. On all the TEA-based coatings, the sample's wetting behavior is greatly improved by the length of the cooking time. The coating's thickness is not very important as long as the entire sample is covered by CNT. However, out of all the TEA samples, the best contact angle measurements were obtained for the samples that were cooked for three and four days. The other samples did present an enhancement, but for prolonged cook times the results were better.

6. Correctly drying and removing excess oil from the coating is extremely important. When a sample was incorrectly dried, the regions with excess oil resulted being hydrophilic, making this process counterproductive.

Having exposed these tendencies, the optimal cooking time is chosen. For Mg-Nit coatings, the samples will be left in the oven for only 1 day. While for the TEA coatings, the samples will be left in the oven for a total of 4 days.

Additionally, it is important to point out that the same results were obtained as in *section 4.7.2*, relating to the required coating thicknesses. This study coincides with thicker coatings for Mg-Nit and thinner ones for TEA.

5. Results & Discussions

5.1. Substrate characterization

This section is dedicated to the analysis and characterization of the steel substrate. Samples were taken from the actual sucker rods that will be coated, in order to study the material's hardness, roughness and phase of the steel.

5.1.1. Base material hardness

Vickers hardness was measured on two type 1 samples. For each sample, two measurements were conducted. Due to the nature of the technique, only flat samples could be reliably measured. It is for this reason that only samples type 1 were measured and not type 2. This is important to keep in mind because the hardness obtained corresponds to hardness found at the center, or neighboring regions, of the sucker rod. The superficial hardness is expected to be higher due to the finishing process (sand blasting).

The measurements were conducted utilizing a micro-hardness tester (Struers DuraScan). After cleaning each sample, two regions were selected. A 4×4 grid was traced on each location, where the indenter will effectively create an imprint, for a total of sixteen measurements per region. The load selected is 0.2 kilograms-force ($HV_{0.2}$) and it is applied for ten seconds. The optical magnification was 40×. **Table 5.1** shows the mean hardness values obtained for both samples and their corresponding standard deviation.

Table 5.1 - Hardness measurements.

Sample	Measurement	Hardness ($HV_{0.2}$)
1	1	288 ± 8
	2	293 ± 20
2	1	303 ± 15
	2	297 ± 12
Average		295 ± 14

It can be seen above that the hardness of the sucker rod is between 288 and 303 HV, with a mean value of 295 HV.

5.1.2. Surface topography analysis

The rod's roughness is measured with a 3D Confocal Laser Scanning Microscope (Olympus LEXT OLS 4100). This is a powerful instrument that allows the user to observe a sample that is not smooth by obtaining a confocal micrograph. With the micrograph, the instrument allows the measurement of superficial roughness through a line scan, in a determined area, etc. In this section, only the parameter R_a is of interest, the arithmetic roughness obtained through a linear scan.

To obtain the arithmetic roughness, a type 2 sample must be cleaned using the procedure described in *section 4.3.* Once cleaned, the sample is placed in a glass sample holder with dough and loaded using a manual press to ensure that the sample is perfectly flat. Otherwise, the images observed in the laser microscope will be distorted and the results obtained incorrect.

To measure the roughness, first, a confocal image must be captured utilizing the laser. The correct focus must be set as to obtain all the desired information. With the captured image, the measuring utilities are used. Here one must make a choice; measure the roughness of the sample along a horizontal line, vertical line, or any other selected trajectory. Having said that, the roughness will be measured along both horizontal and vertical lines, to corroborate if there is any sort of anisotropy.

The sample is placed in such a way that the curvature of the rod sample is along the horizontal line. The measuring software of the laser microscope allows the removal of error due to the curvature of the sample. This error will be removed for all cases, not only for measurements conducted in the horizontal direction.

For each direction, three measurements were conducted. One at the center of the sample, and one at each side equidistantly. **Table 5.2** shows the arithmetic roughness obtained for a type 2 sample. Since this is an optical measurement, it is important to mention that the optical magnification used was 5× with no additional digital zoom.

Table 5.2 - Arithmetic roughness of type 2 sample.

Direction	Location	Ra /µm
Horizontal	Center	14.66
	Bottom	15.28
	Top	14.99
Vertical	Center	15.08
	Left	15.53
	Right	19.73

Due to the nature of the superficial finishing of the rods, it was expected that the roughness would vary throughout. As the **Table 5.2** shows, roughness values vary between about 14.66 µm and 19.73 µm. The mean roughness value is 15.88 µm, with a standard deviation of approximately 1.70 µm. **Fig. 5.1a** shows the roughness profile of the sample in the horizontal direction, while **Fig. 5.1b** the roughness profile in the vertical direction. Also, **Fig. 5.2** shows an image of the sample's surface captured with this instrument utilizing a magnification of 5×.

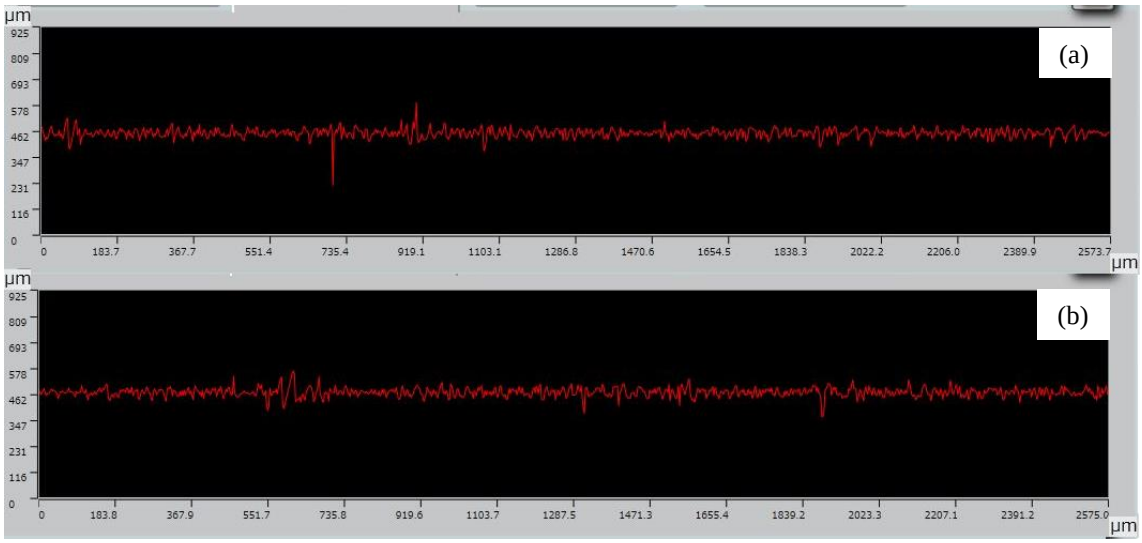

Fig. 5.1 - (a) Horizontal roughness profile; (b) Vertical roughness profile.

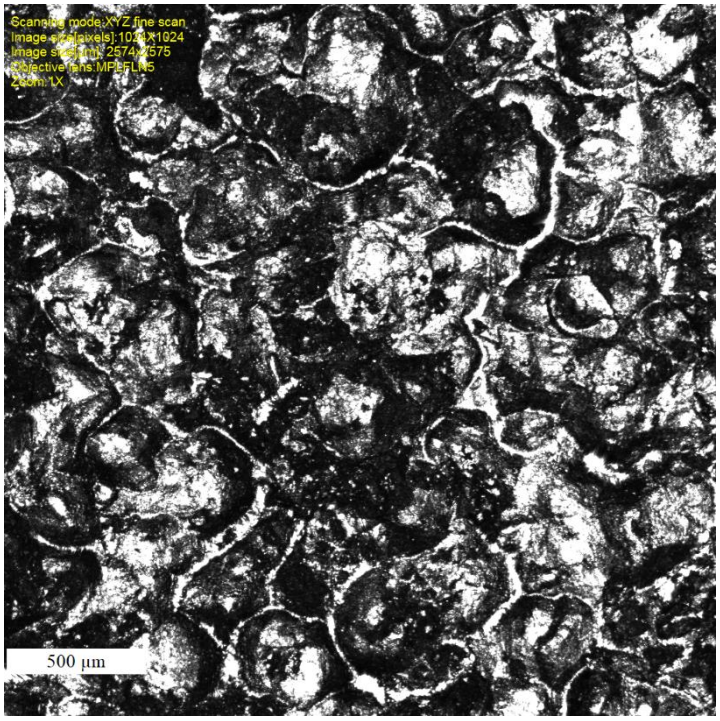

Fig. 5.2 – Laser microscope intensity image of the sample surface.

5.1.3. Base material phase analysis
X-Ray Diffraction

To acquire the XRD spectrum the following equipment parameters were used:

- 2 Theta scan range from 20° to 120°
- 2 Theta step size of 0.013°
- Counting time of 18.87 seconds per step
- Geometrical configuration of diffractometer set to Bragg-Brentano

After the XRD spectrum has been acquired, the data must be processed. To process the XRD spectrum, the *X'Pert Highscore Plus* software was utilized.
The first steps taken consists of removing the $k\alpha_2$ line, followed by a background correction.

After applying these two filters, the *X'Pert DataViewer* software is used find the appropriate powder diffraction files (PDF), while these PDF are obtained from the International Center for Diffraction Data (ICDD). These files contain information about the position of the different allowed reflections of a certain phase for a specific radiation source (in this case, Cu) and are utilized to index the peaks obtained in the clean spectrum by comparing these peaks with standard peaks of different compounds. **Fig. 5.3** shows the indexed XRD spectrum. The steel presents a predominantly ferritic crystalline

structure, along with signals from hematite (Fe_2O_3) and magnetite (Fe_3O_4) derived from oxidation.

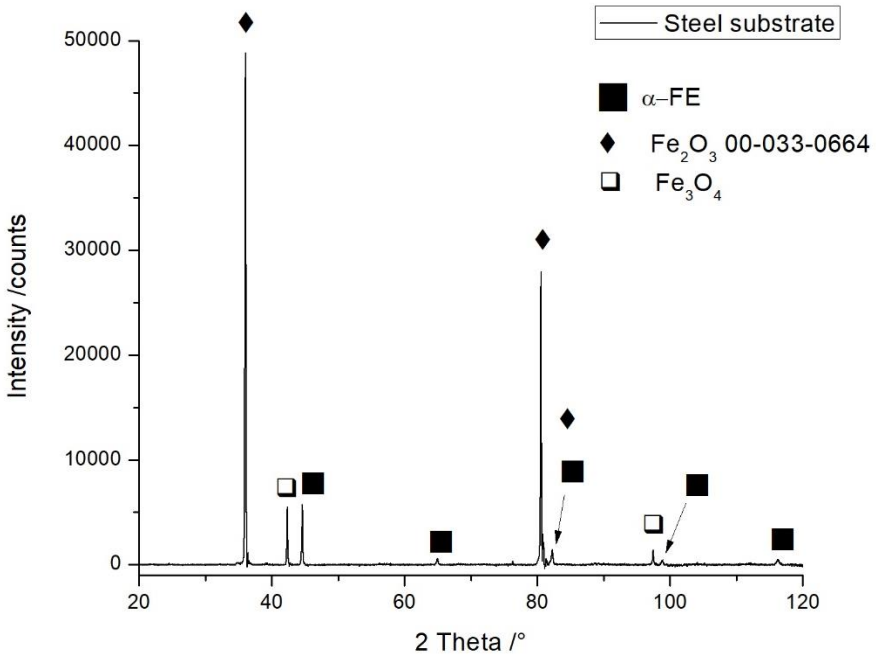

Fig. 5.3 - Indexed XRD spectrum of base material.

Phase analysis by electron backscattered diffraction (EBSD)

Since XRD provides an integral and not site-specific phase evaluation, EBSD was used to identify the phase distribution and fraction in the material. Furthermore, the grain size could also be evaluated by this means.

With the raw EBSD results, through a post-analysis process, one may obtain important information. Which are: the inverse pole figure and image quality (IPF and IQ), phase map and grain size distribution.

Before the analysis, a filtering routine must be applied so as to remove bad data points. This filter cleans up the data first by standardizing the confidence index (CI) within each grain, followed by the removal of those regions with a CI below 0.09.

The CI is calculated during the indexing of the Kikuchi diffraction patterns. For a given pattern, several combinations of orientations might satisfy the indexing to different extent. During indexing, the software automatically ranks these solutions and compares to the ideal state. Hence, the values range from 0 (no reliable solution) to 1 (perfect agreement). Factors that might deviate the CI from a value of 1 could be, for example: improper sample preparation, strains, etc. All these factors affect the sharpness of the diffraction bands, thus complicating its analysis. For lower CI values, it means that the

software is not so certain that the band matches the phase at the given orientation. An acceptable mean CI for low-alloyed steels is generally between 0.5 to 0.8 (depending on the complexity of the phase distribution, domain size, strain, etc.).

The software compares each consecutive point in pairs. If two consecutive points have a misorientation that differs in less than 5°, then it is considered that these two points belong to the same grain. If the misorientation differs in more than 5°, than this location is considered to be a grain boundary. Therefore, one grain is defined by at least two consecutive points with a misorientation below 5°. Once each grain has been identified, the software assigns each grain a CI. This CI value assigned to the whole grain corresponds to the highest point value. **Fig. 5.4a** shows IPF and IQ image obtained for the steel substrate.

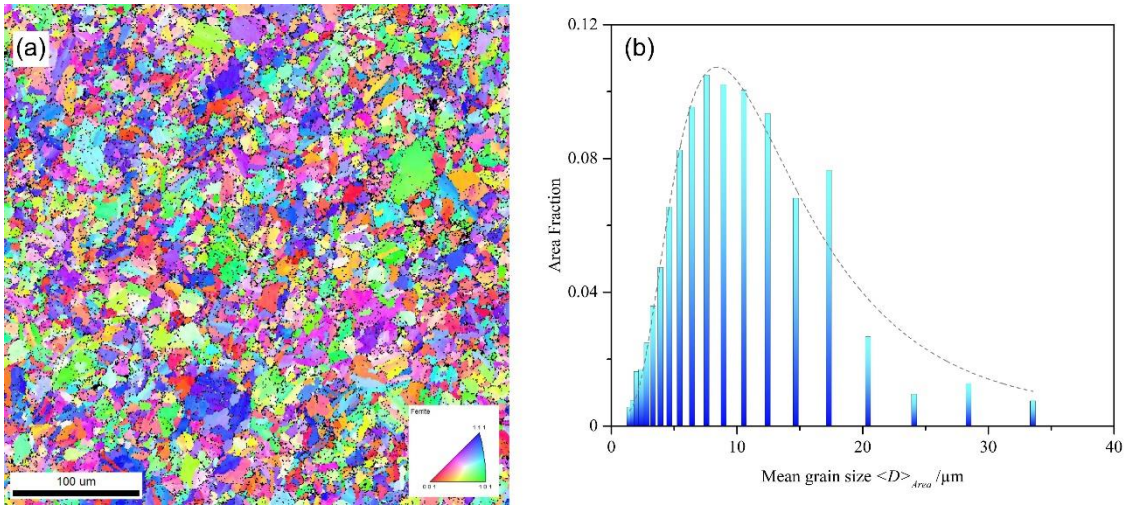

Fig. 5.4 - **(a)** Inverse pole figure map of the ferritic phase; **(b)** Grain size distribution of the ferritic phase. The dashed line represents a log-normal fitting of the distribution.

The grain size distribution of the ferrite phase is shown in **Fig. 5.4b**. It is widely accepted that in as-produced materials, the grain size distribution could be fitted with a log-normal probability density function due to the random nature of the size distribution. Accordingly, the mean grain size is 9.37 µm with a standard deviation of 5.78, obtained from a set of 7026 valid grains.

After obtaining the IPF map and grain size distribution, a second processing can be applied to obtain phase distribution map. This map shows the phase fraction present in the studied region.

For this, a CI filter is applied. This filter removes all grain information with a CI below 0.09. Therefore, all the information present in the phase map possesses a CI of at least 90%, which means each point is very accurately indexed. After applying this

processing, the phase map is obtained and shown in **Fig. 5.5a**. All the regions that are shown in red are where ferrite is present, whereas green corresponds to hematite (approximately 94% ferrite and 6% hematite). The black regions in this image corresponds to the filtered information (indexed points with CI < 0.09). Green lines shown in **Fig. 5.5b** are the locations where the misorientation exceeds 15° (denoted as high angle grain boundaries).

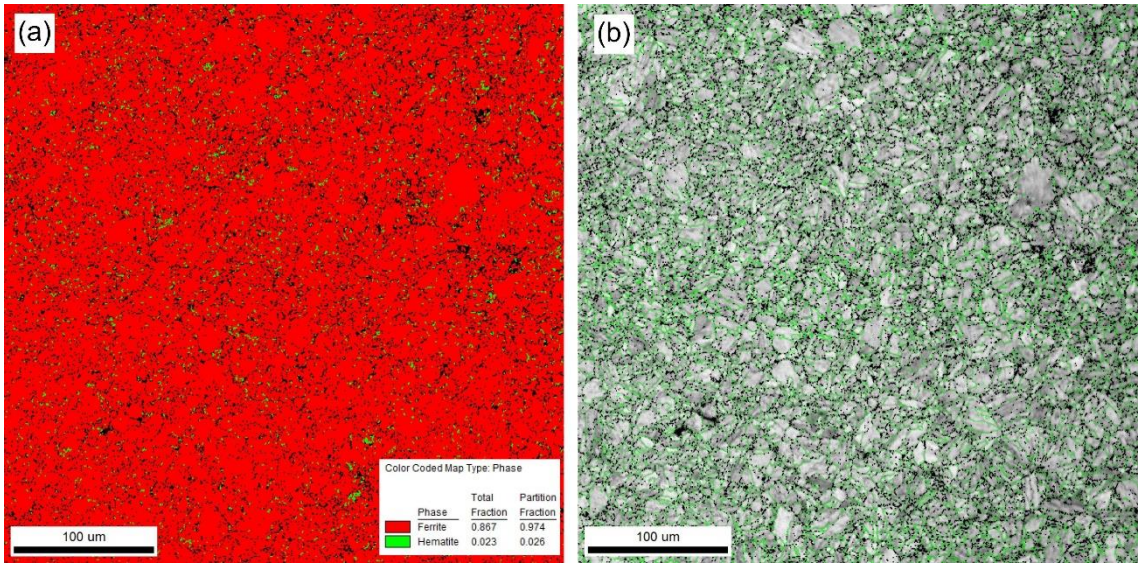

Fig. 5.5 – **(a)** Phase distribution map of ferrite (red) and hematite (green); **(b)** Image quality map with the high angle grain boundaries highlighted in green. It is evident that the native oxidation occurs predominantly on the grain boundaries.

5.2. Coating structural analysis

This section focuses on the structural characterization of the coatings. This characterization includes the study of the coatings itself, along with how it interacts with the substrate and with the atmosphere.

5.2.1. CNT structural analysis (Raman spectroscopy)

The Raman spectra are acquired utilizing a Renishaw inVia Raman Microscope. Before the spectra are acquired, the instrument must be calibrated. This is done with a standard silicon wafer. Utilizing a wavelength of 532 nm for the laser (green laser), and a corresponding 2.33 eV energy level, the Raman shift of the silicon characteristic peak should be at 520.5 ± 0.2 cm^{-1}. Each studied sample is observed three times (three accumulations), with the resulting intensity being the sum of all three accumulations. The wavenumber sweep goes from 1000 cm^{-1} to 3200 cm^{-1}, which is where the relevant bands are, and the diameter of the laser spot is 3 µm. The magnification utilized was of 50×, and

the laser power was set a 1% of the full intensity, so as to avoid thermal modifications and chemical desorption on the carbonaceous sample.

A total of seven Raman spectra were acquired for six different samples. The characteristics of these samples are summarized in **Table 5.3**, and the spectra for each sample will be individually analyzed in this section. For sample T14, two spectra were collected.

Table 5.3 - Raman samples.

Sample	Additive	Deposition time /min	Cook time /days
M51	Mg-Nit	5	1
M54	Mg-Nit	5	4
T14	TEA	1	4
T22	TEA	2	2
MRD8	Mg-Nit	5	0
TRD8	TEA	5	0

After the spectra have been acquired, a small post-processing must be conducted on the raw data. This is performed with a freeware called “CrystalSleuth”. With this software, one can remove the intensity background of the collected data, remove cosmic rays artifacts if necessary, and export the processed spectrum. Once the background is removed, the data is imported to a mathematical software (OriginPro) for analysis. In this software, the three different bands widths are selected individually with the data selector and a Lorentz Fit is adjusted. It is known that the peak profiles in Raman spectroscopy are described by a Breit-Wigner-Fano profile. However, due to its mathematical complexity, a quick and accurate approximation is achieved by adjusting a Lorentz probability distribution [64]. After fitting, the software generates a table for each peak with the information required for analysis, including: peak position, maximum intensity value of peaks, full width at half maximum (FWHM), and integral peak area (i.e. area under each peak). This process will be repeated for all seven acquired spectra.

Pristine CNT

Additionally from the seven spectra mentioned before, a Raman spectrum of the pristine CNT was acquired as a reference state (**Fig. 5.6**). In this figure, the three characteristic peaks are easily identified. For the pristine CNT, the D band is located at

approximately 1349 cm^{-1}, with the theoretical location being at 1340 cm^{-1}. The G band is also within range, located at about 1583 cm^{-1}. The G' band however, appears slightly shifted towards higher frequencies at 2960 cm^{-1}, but in agreement with the location of the D band (as already mentioned, the G' band is the second overtone of the D band).

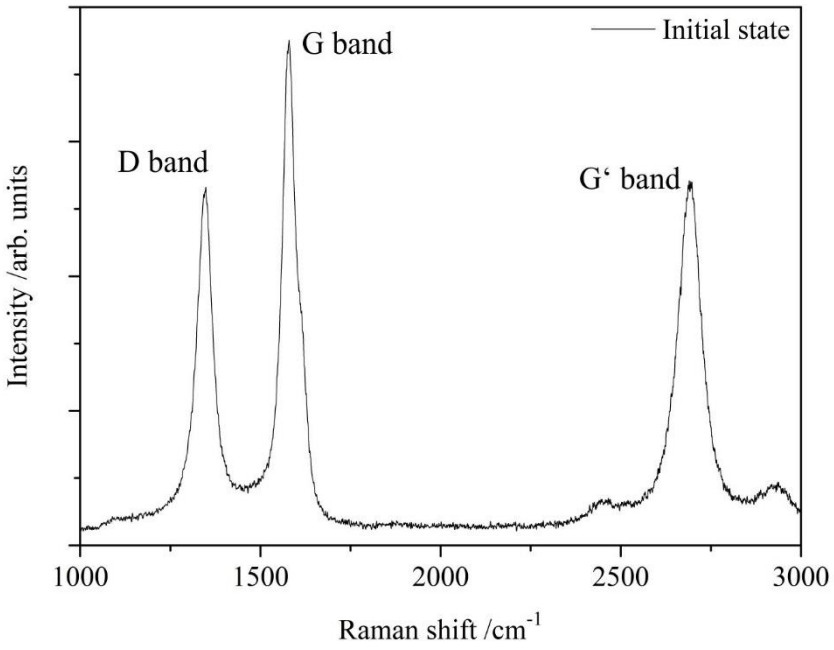

Fig. 5.6 - Raman spectrum of pristine CNT.

From this spectrum, it can be seen that the pristine CNT do not present a significant amount of defects, due to the almost ideal location of the G band and the defect ratio is below 1 (I_D/I_G = 0.71). The G band is in its expected location, meaning the majority of the CNT present a strong grade of crystallinity. Furthermore, the pristine CNT high purity, hence the strong intensity of the G' band and the elevated value of the purity ratio ($I_{G'}/I_D$ = 1.02).

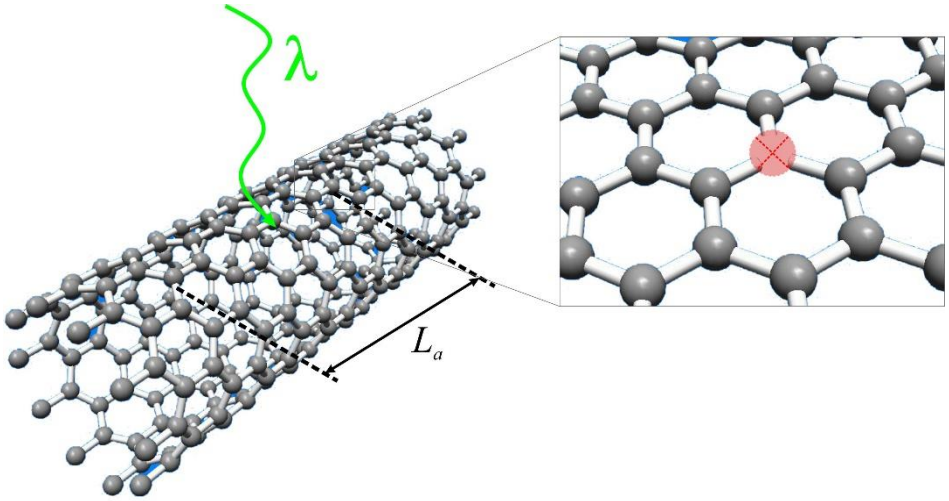

Fig. 5.7 – Schematic representation of mean inter-defect distance detection via Raman.

Moreover, L_a is the mean inter-defect distance and represents the mean separation between two consecutive defects (a schematic representation is shown in **Fig. 5.7**), irrespective of their nature (vacancies, Stone-Thrower-Wales defects, etc.). It is calculated based on the relationship proposed by Tuinstra and Koenig (Eq. 14) [65], [66]:

$$L_a(nm) = (2.4x10^{-10}) \cdot \lambda_{laser}^4 \cdot \left(\frac{I_D}{I_G}\right)^{-1} \quad (14)$$

Table 5.4 shows the fit data for each of the three peaks obtained, while **Table 5.5** shows the two ratios and the mean inter-defect distance.

Table 5.4 – Reference sample peak fit data.

Band	Intensity /counts	Peak center /cm^{-1}	FWHM (Γ) /cm^{-1}
D	2672.1	1345.8	49.4
G	3776.4	1580.4	50.7
G'	2735.7	2691.1	77.7

Table 5.5 – Reference sample ratios and mean inter-defect distance.

I_D/I_G	0.71
$I_{G'}/I_D$	1.02
L_a /nm	27.2

Mg-Nit coating samples

Sample M51

Fig. 5.8a shows the Raman spectrum of sample M51. In this spectrum, it can be observed that the D band is located at approximately 1349 cm^{-1}, the G band is ideally located at 1588 cm^{-1}, and the G' band at 2693 cm^{-1}. Based on the defect ratio, and the location of the peaks, very low defects (I_D/I_G = 0.53) and high crystallinity are observed. In regards of CNT purity, this sample presents higher purity compared to the reference sample. This is observed by the high intensity of the G' band and the elevated purity ratio ($I_{G'}/I_D$ = 1.12).

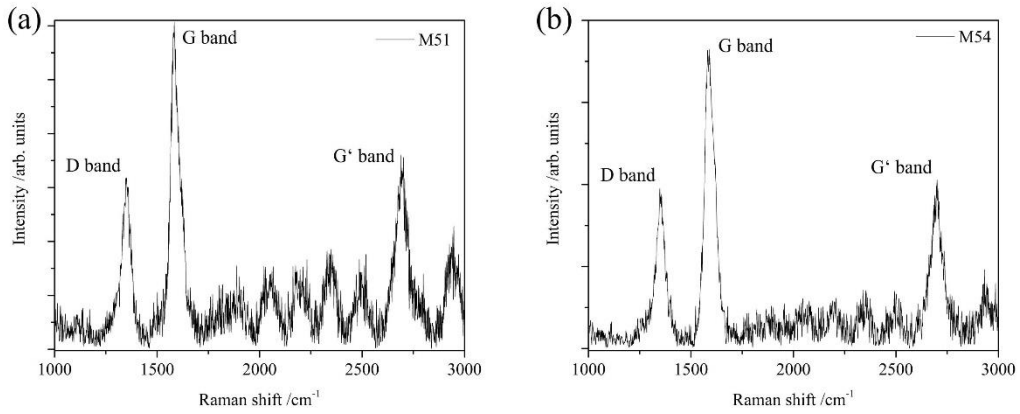

Fig. 5.8 – **(a)** Raman spectrum of sample M51; **(b)** Raman spectrum of sample M54.

Table 5.6 shows the fit data for each of the three peaks obtained, while **Table 5.7** shows the two ratios and the mean inter-defect distance.

Table 5.6 – Sample M51 peak fit data.

Band	Intensity /counts	Peak center /cm^{-1}	FWHM (Γ) /cm^{-1}
D	3172.9	1349.6	50.3
G	5979.4	1587.9	54.1
G'	3538.9	2692.9	70.5

Table 5.7 – Sample M51 ratios and mean inter-defect distance.

I_D/I_G	0.53
$I_{G'}/I_D$	1.12
L_a /nm	36.2

Sample M54

The Raman spectrum for sample M54 is shown in **Fig. 5.8b**. In this spectrum, the D band is located at about 1351cm^{-1}, the G band at 1591 cm^{-1}, and the G' band at 2698 cm^{-1}. As for sample M51, the CNT that form the coating present low defects and high crystallinity due to the outstanding peak locations and low defect ratio (I_D/I_G = 0.55). In terms of purity, the CNT present high purity due to an elevated purity ratio ($I_{G'}/I_D$ = 1.05) and G' peak intensity, although this sample's purity is lower than M51.

Table 5.8 shows the fit data for each of the three peaks obtained, while **Table 5.9** shows the two ratios and the mean inter-defect distance.

Table 5.8 – Sample M54 peak fit data.

Band	Intensity /counts	Peak center /cm^{-1}	FWHM (*Γ*) /cm^{-1}
D	1967.3	1348.1	51.4
G	3575.6	1587.6	61.6
G'	2056.7	2699.7	68.6

Table 5.9 – Sample M54 ratios and mean inter-defect distance.

I_D/I_G	0.55
$I_{G'}/I_D$	1.05
L_a /nm	34.9

TEA coating samples

Sample T14

For this sample, two spectra were acquired in two different locations. In the first spectrum, the D band is located at approximately 1351 cm^{-1}, the G band at 1592 cm^{-1}, and the G' band at 2697 cm^{-1}. Identically as for samples M51 and M54, the CNT present high crystallinity and very little defects as a consequence of low defect ratio (I_D/I_G = 0.57). The purity however, is lower at this site compared to previous samples, with a purity ratio below 1 ($I_{G'}/I_D$ = 0.85). This spectra is shown in **Fig. 5.9a**.

The second spectrum shows the D band at 1352 cm^{-1}, the G band at 1588 cm^{-1}, and the G' band at 2700 cm^{-1}. For this second location, compared to the first location, the CNT present fewer defects and higher crystallinity (I_D/I_G = 0.46). Additionally, this second site presents higher purity, showing a higher purity ratio ($I_{G'}/I_D$ = 1.30). This spectra is shown in **Fig. 5.9b**.

Table 5.10 shows the fit data for each of the three peaks obtained for both locations, while **Table 5.11** shows the two ratios and the mean inter-defect distance for both studied regions.

Compared to the first spectrum, the CNT defects in both locations are very similar. The crystallinity in the second location is slightly better than in the first location. Furthermore, the purity in the second location is somewhat better as well. This may be caused by a higher concentration of TEA in different regions of the sample, or a higher residue content from the cooking process in different regions.

It is important to keep in mind that the CNT present different characteristics throughout the surface. This was percieved studing two different regions in a single sample and obtaining different results. However, the results obtained, although different, are similar nonetheless. In contrast to the band locations, the purity ratio does variate significantly between the two regions of study, while the defect ratio varies very little.

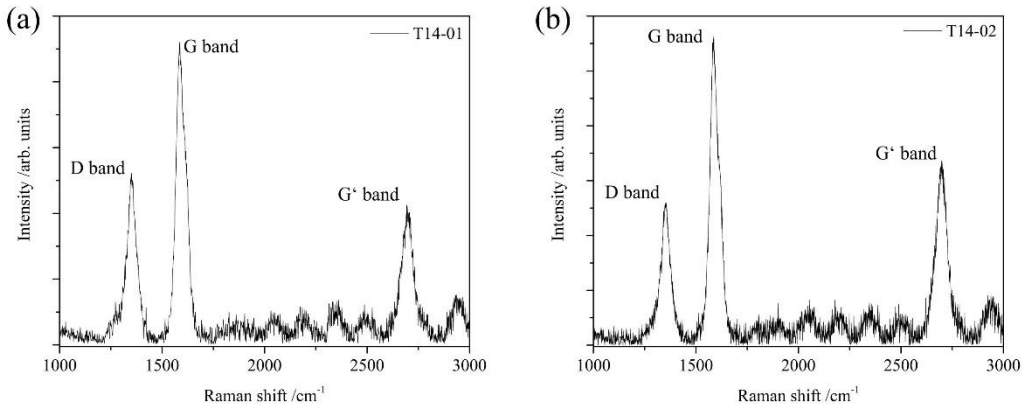

Fig. 5.9 – (a) Raman spectrum of sample T14-01; **(b)** Raman spectrum of sample T14-02.

Table 5.10 – Sample T14-01 and T14-02 peak fit data.

	T14-01			**T14-02**		
Band	**Intensity /counts**	**Peak center /cm^{-1}**	**FWHM (Γ) /cm^{-1}**	**Intensity /counts**	**Peak center /cm^{-1}**	**FWHM (Γ) /cm^{-1}**
D	5309.5	1351.4	53.7	5184.5	1351.8	53.9
G	9265.5	1592.2	67.5	11248.8	1590.8	59.7
G'	4537.5	2696.9	70.0	6729.3	2698.1	67.9

Table 5.11 – Sample T14-01 and T14-02 ratios and mean inter-defect distance.

	T14-01	**T14-02**
I_D/I_G	0.57	0.46
$I_{G'}/I_D$	0.85	1.30
L_a /nm	33.5	41.7

Sample T22

Acquiring the Raman spectrum of sample T22 resulted unsuccessful. Three different attempts were made, with different laser intensities (1% and 0.5%), but the acquisition was unsuccessful. This may be due to the fact that the coating itself was too thin, or due to an error in the measuring instrument. Nonetheless, it is expected that similar results as for sample T14 were to be obtained.

Non-post-processed samples

Sample TRD8

The Raman spectrum of this sample is shown in **Fig. 5.10a**. In this figure, the D band is located at approximately 1351 cm^{-1}, the G band at 1587 cm^{-1}, and the G' band at 2699 cm^{-1}. For this sample, the CNT present similar crystallinity and amount of defects compared to the other TEA samples, as the defect ratio is quite similar ($I_D/I_G = 1.06$). In regards to the purity of the CNT, the purity ration is very similar to the value obtained for T14-02, which is quite elevated ($I_{G'}/I_D = 1.19$). This was to be expected since the same batch of nanoparticles were used for all the coatings. However, it was learned that the additive affects the coating in very similar fashions, resulting in similar purity, defect and crystallinity.

Table 5.12 shows the fit data for each of the three peaks obtained, while **Table 5.13** shows the two ratios and the mean inter-defect distance.

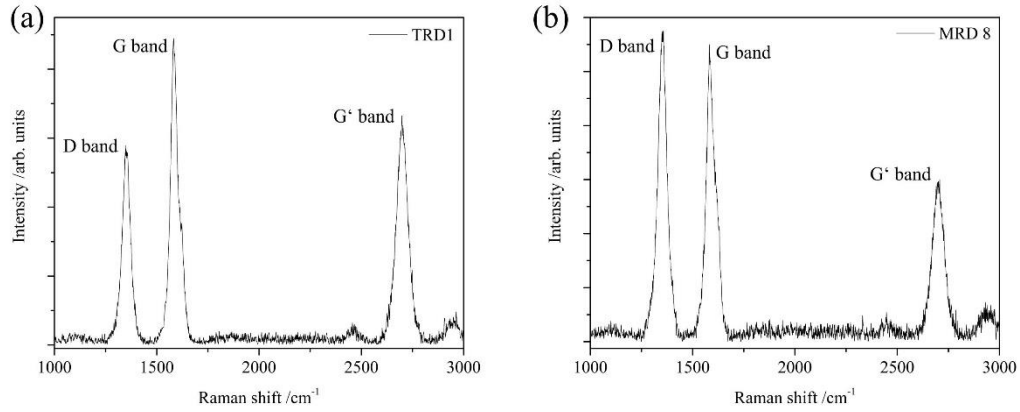

Fig. 5.10 – a) Raman spectrum of sample TRD8; b) Raman spectra of sample MRD8.

Table 5.12 – Sample TRD8 peak fit data.

Band	**Intensity /counts**	**Peak center /cm^{-1}**	**FWHM (Γ) /cm^{-1}**
D	1144.2	1351.3	47.7
G	1790.4	1586.5	47.7
G'	1358.7	2699.8	69.8

Table 5.13 – Sample TRD8 ratios and mean inter-defect distance.

I_D/I_G	0.64
$I_{G'}/I_D$	1.19
L_a /nm	30.1

Sample MRD8

The Raman spectrum of sample MRD8 is shown in **Fig. 5.10b**. As it can be seen, the location of the D band is approximately 1353 cm^{-1}, the G band at 1589 cm^{-1}, and the G' band at 2700 cm^{-1}. For this sample, the crystallinity is lower and the defects of these CNT are higher, compared to the other Mg-Nit samples, with a defect ratio that is quite elevated (I_D/I_G = 1.06). In regards to the purity, it was expected to be better since this sample was not cooked in crude oil. Nonetheless, the resulting purity is significantly lower than the Mg-Nit samples that underwent the post-processing, with a very low purity ratio ($I_{G'}/I_D$ = 0.51). These differences are surprising since the same batch of CNT were used for all conducted coatings.

Table 5.14 shows the fit data for each of the three peaks obtained, while **Table 5.15** shows the two ratios and the mean inter-defect distance.

Table 5.14 – Sample MRD8 peak fit data.

Band	Intensity /counts	Peak center /cm^{-1}	FWHM (Γ) /cm^{-1}
D	1182.5	1352.5	53.1
G	1110.9	1588.9	63.6
G'	600.4	2700.2	76.1

Table 5.15 – Sample MRD8 ratios and mean inter-defect distance.

I_D/I_G	1.06
$I_{G'}/I_D$	0.51
L_a /nm	18.1

Further discussions

Crystallinity and disorder

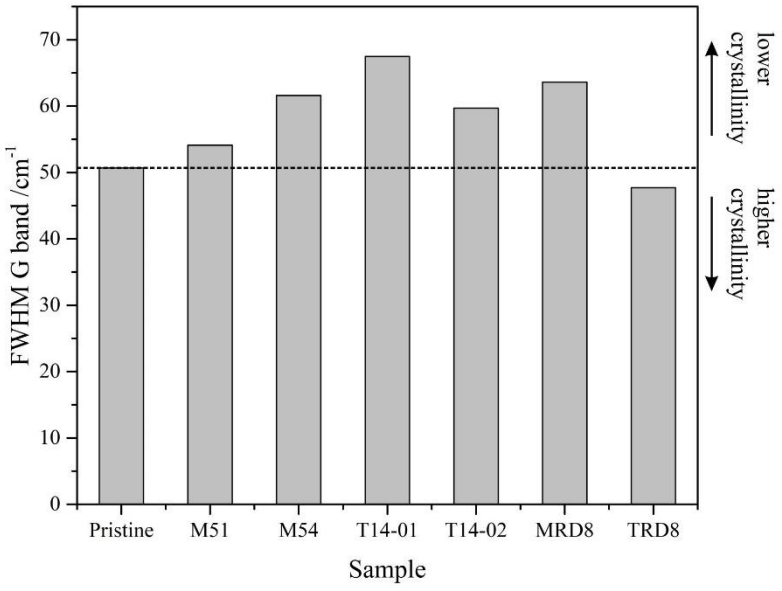

Fig. 5.11 – Crystallinity gain/loss comparison.

As **Fig. 5.11** shows, most of the samples (except TRD8) show lower crystallinity when compared to the pristine state. It could result from the exposure time to the ultrasound and/or the dispersing instrument. For the particular case of samples M51 and TRD8 however, it could be that these samples are within the uncertainty of the measurements, meaning that the respective loss or increase of crystallinity is not such. In these cases, the FWHM varies from the pristine state by approximately 5 cm^{-1}. For the other samples analyzed, the FWHM presents higher variations surpassing 10 cm^{-1}.

The crystallinity is analyzed by applying Heisenberg's uncertainty principle to the study of the Raman shift (as explained by Suarez et al. [67]), where an increase in the FWHM would represent a shorter resonance extinction time and hence, a lower lattice crystallinity of the CNT.

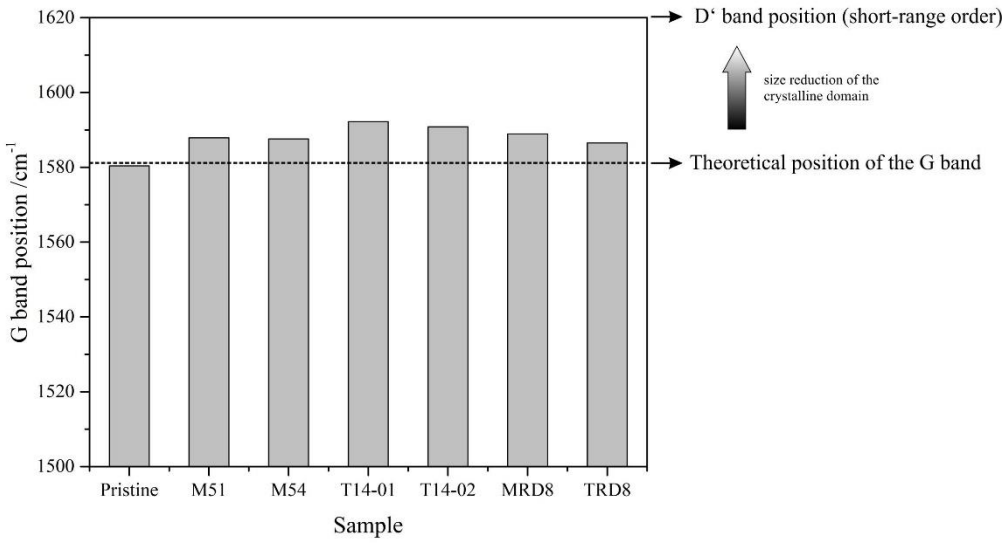

Fig. 5.12 – G band actual position compared to its theoretical position.

Fig. 5.12 shows the upward shift of the G band compared to the theoretical position for all studied samples. The theoretical position of the G band has been taken from Dresselhaus et al. [68]. This analysis is based on that proposed by Ferrari and Robertson [64], in which the upshifting of the G band is associated to a predominant short-range order of the lattice domains. Here, the upshift is physically not possible, since the position of the G band is set by the E2g phonon symmetry (being at 1582 cm^{-1} for graphitic carbon). What actually occurs is that a band associated to the short-range order of the lattice (D' band placed at 1620 cm^{-1}) starts to increase in intensity as the structure

loses its structural integrity. Hence, what is observed is a convolution of both bands that results in the apparent upshifting of the G band. In the abovementioned reference (Ferrari and Robertson [64]), the limit of the graphitic structure lays at about 1600 cm^{-1}, beyond which the sp^2 bonds start to rearrange themselves into sp^3 bonds. This rearrangement is usually associated with an increase in the disorder of the graphitic structure and can have its origin in several features, as for example; extended exposure to ultrasound, being subjected to significant mechanical stresses, etc. In this particular case, it can be stated that all coatings show no significant loss of long-range order, being their G band position within the values expected for weak, non-covalent functionalization. Therefore, no significant levels of disorder are detected. The variation of the G band's position ranges between 5 cm^{-1} for sample TRD8 to 10 cm^{-1} for sample T14-01.

Defects

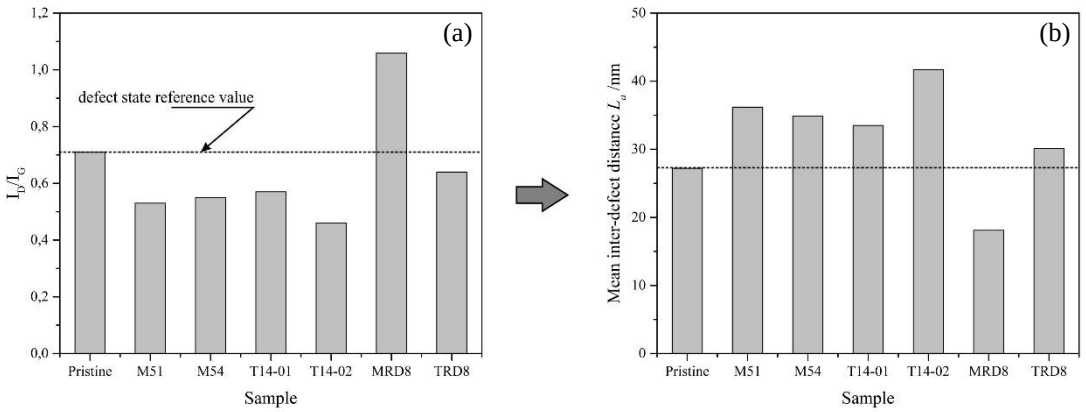

Fig. 5.13 – **(a)** Defect state comparison; **(b)** Mean inter-defect distance comparison.

The defect state is, unexpectedly, in all cases (except sample MRD8) is lower than the initial state, as **Fig. 5.13a** shows. One should be careful not to over-interpret these results, since this could be a consequence of the weakening of the resonance effect generated by the foreign species present on the surface of the CNT. This weakening of the resonance effect may be caused by species that are introduced on the surface by the post-deposition process. However, samples MRD8 and TRD8 do not possess said process. Therefore, it would appear that in the case of MRD8 this weakening effect does not occur, and the defect state is correctly detected. For sample TRD8 however, the

weakening effect could be generated by TEA since this is the only foreign species that could react with the surface and produce this weakening effect since no post-deposition process has been conducted on this sample. Another possible explanation is that, after a thermal treatment, certain (low-energy) defects could be "healed" in the same manner as an annealing process. Furthermore, by analyzing the mean inter-defect distance shown in **Fig. 5.13b**, the values are within those usually observed for this processing method. Accordingly, the samples that possess higher defect levels also possess lower mean inter-defect distances and vice versa.

Purity

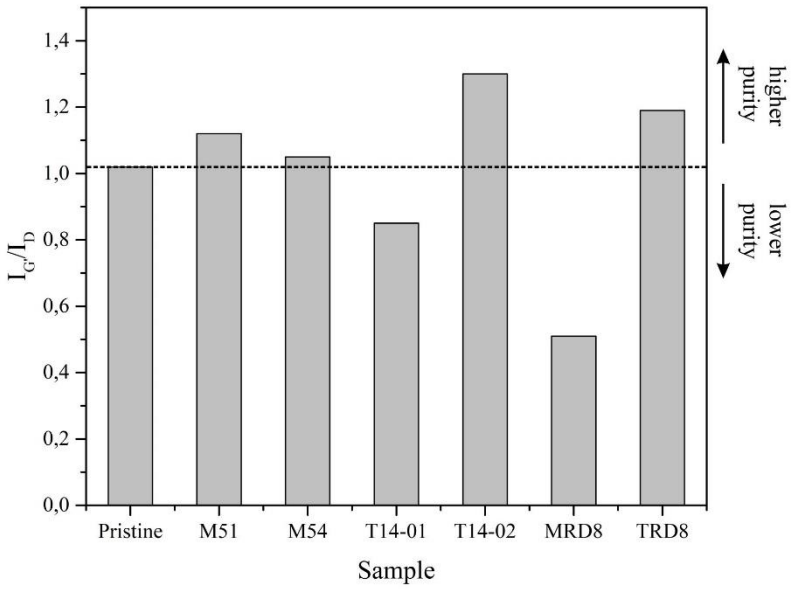

Fig. 5.14 – Purity gain/loss comparison.

Fig. 5.14 shows a comparison of the purity analysis conducted on the different samples. The most significant result is that of the MRD8 sample, since it seems to have retained many impurities from the deposition, since this sample does not possess a post-deposition process. These retained impurities would weaken the two-phonon, second-order scattering process that manages its intensity [46], [49]. However, the variation in purity, as DiLeo et al. [46] has stated, may be a result of different carbonaceous purity levels and not necessarily foreign elements. Therefore, low purity level observed for

sample MRD8 may be a consequence of highly damaged CNT structures. This hypothesis is supported observing **Fig. 5.13a** and **Fig. 5.13b**, where this sample shows a higher defect content (when compared to the other samples studied), and corresponding lower mean inter-defect distance. On the same note, sample T14-02 shows the highest purity level, and correspondingly the lowest defect content and highest mean inter-defect distance. From these observations, it is assumed that although the first four samples studied (M51, M54, T14-01, and T14-02) underwent the proposed post-deposition process, said process does not significantly alter the detected CNT's purity and does not generate considerable defects on the CNT's structure.

5.2.2. Thickness/compactness analysis

The thickness and compactness of the different coatings was characterized by FIB cross-sections. By performing these, and subsequently tilting the sample, an in-depth view of the sample is achieved. By observing said cross-section the thickness of the coating can be quantified, along with a qualitative analysis of the coating's compactness. The latter is related to the amount of pores and their size distribution. For the different attained coatings, high compactness is desired due to the simple fact that each pore is a possible mean of travel for corrosive substances. With a highly packed coating, the substrate is better protected from said agents by obstructing their path towards the substrate. Additionally, before performing the cross-section, the surface of the coating can be characterized in terms of homogeneity and regularity.

This analysis has been carried out for three different samples (representative of the proposed variations), all of which possess a type 2 substrate. The characteristics of these samples are summarized in **Table 5.16**.

Table 5.16 – Different samples analyzed via SEM/FIB.

Sample	Additive	Deposition time /min	Cook time /days
MRD8	Mg-Nit	5	0
TRD1	TEA		
DDRC4	Double deposition	3 for Mg-Nit ; 2 for TEA	4

The deposition time for samples MRD8 and TRD1 have been fixed at five minutes because it was of interest to observe the different CNT thickness utilizing both additives.

For sample DDRC4 however, the set "standard" deposition times were utilized, three minutes of Mg-Nit and two minutes of TEA over the previous coating.

For all three cases, the Platinum deposition was carried out with a voltage of 30 keV and a current of 0.92 nA. The deposition area possessed dimensions of 20 µm by 4 µm with a total height of 1 µm. In the cases of the actual cross-section cut, the dimensions were 20.5 µm by 15 µm with a depth of 6 µm deep, with the voltage fixed at 30 keV and the current at 21 nA.

Sample MRD8

Fig. 5.15a shows a SEM image of the MRD8's surface, with **Fig. 5.15b** illustrating a close-up of the surface. The surface of the coating is seen as irregular with pores and with regions where the CNT have bonded in a way where a "gap" remains. This gap represents a much larger pore. As seen in the zoomed image, the small pores possess an approximate mean diameter of 7 µm.

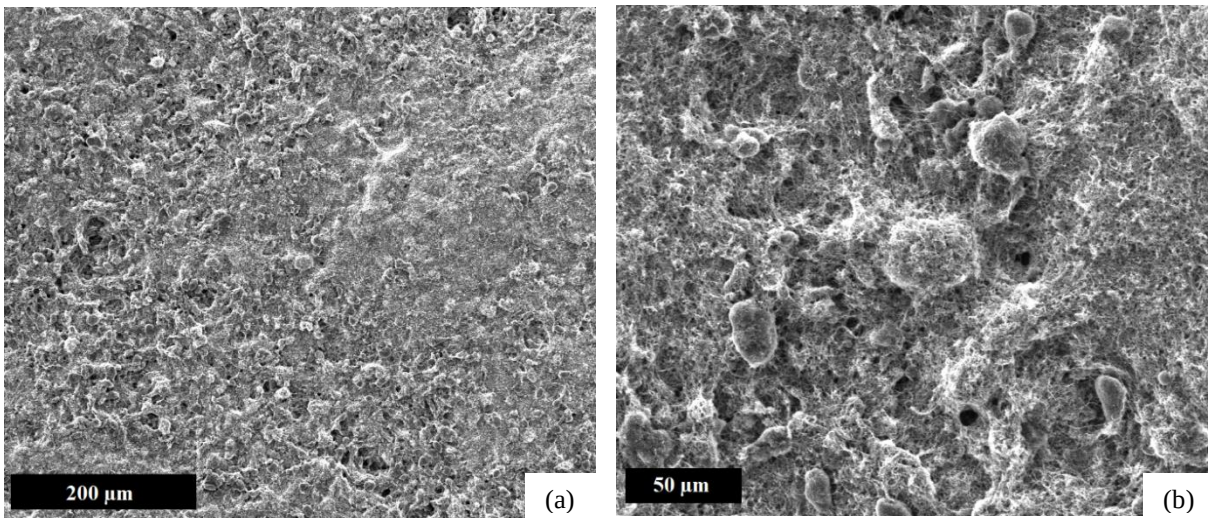

Fig. 5.15 – **(a)** Sample MRD8 surface at 200× magnification; **(b)** Sample MRD8 surface at 1000× magnification.

It can be observed in **Fig. 5.16a** that the coating presents an average thickness of about 12.5 µm. Observing the transversal section of the coating, several large pores are revealed. The coating presents regions of significant compactness, but also large porous regions with very few, if any, CNT. **Fig. 5.16b** shows a magnified image of a porous region. A couple of the larger pores are highlighted with arrows.

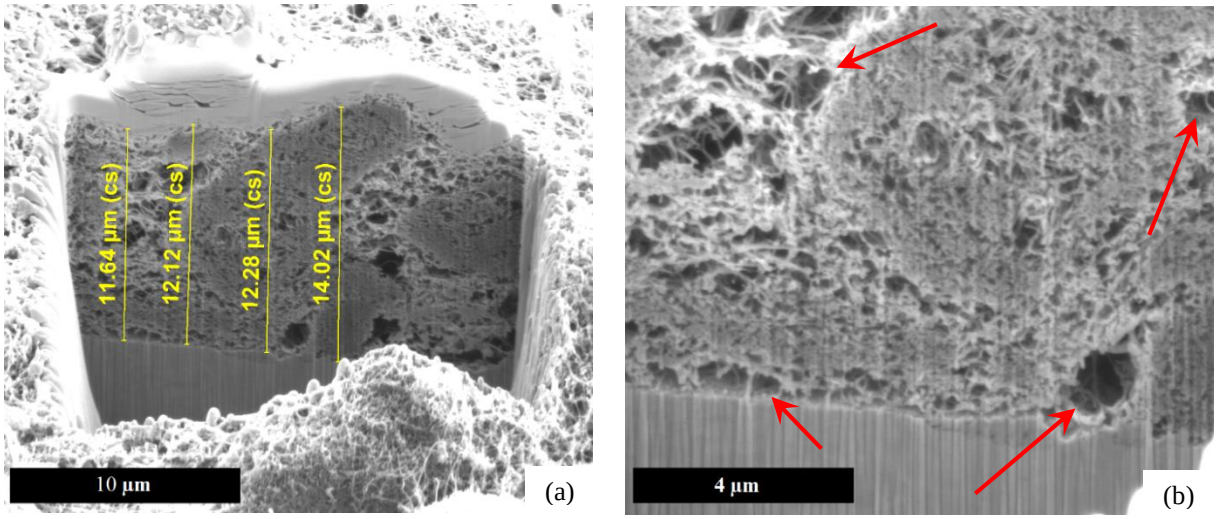

Fig. 5.16 – **(a)** Sample MRD8 cross-section at 5000× magnification; **(b)** Sample MRD8 cross-section at 12000× magnification. The red arrows indicate pours within the coating.

The large pore observed in the lower-right region of **Fig. 5.16b** possesses an approximate diameter of 1.6 µm, representing a value of approximately 13% of the coating's thickness. These pores are not only a possible path for corrosive agents to reach the substrate, but also represent a weakly-bonded region of the coating where the coating may fail to efficiently adhere to the substrate.

In regards to the interface between the coating and the substrate, for sample MRD8 it looks quite seamless. The interface looks continuous, with CNT homogenously dispersed throughout the surface of the substrate. Some regions of the interface possess pores, nonetheless, even in porous regions it is observed that CNT have interacted somewhat with the substrate's surface (as it can be seen in the lower-left part of **Fig. 5.16b**). Therefore, even in porous regions the substrate present a thin CNT barrier. This is important because this thin CNT barrier is the final defense that the substrate possess against corrosive agents.

Sample TRD1

Equivalently as done for sample MRD8, **Fig. 5.17a** depicts the surface of sample TRD1 as seen with the SEM. Additionally, **Fig. 5.17b** shows an up-close image of the sample's surface.

At first glance, it can be seen in **Fig. 5.17a** that this surface is less homogeneous than that of sample MRD8 (**Fig. 5.15a**). Sample TRD1's surface presents more irregularities and larger CNT agglomerates bundled together. These large CNT agglomerates are better observed in **Fig. 5.17b**. This is a consequence of the weaker bonding of the by-products

from TEA in comparison to those resulting from the addition of Mg-Nit. Here, many CNT agglomerates are observed throughout the sample's surface. It is evident that this sample presents a more porous network when compared to the Mg-Nit sample.

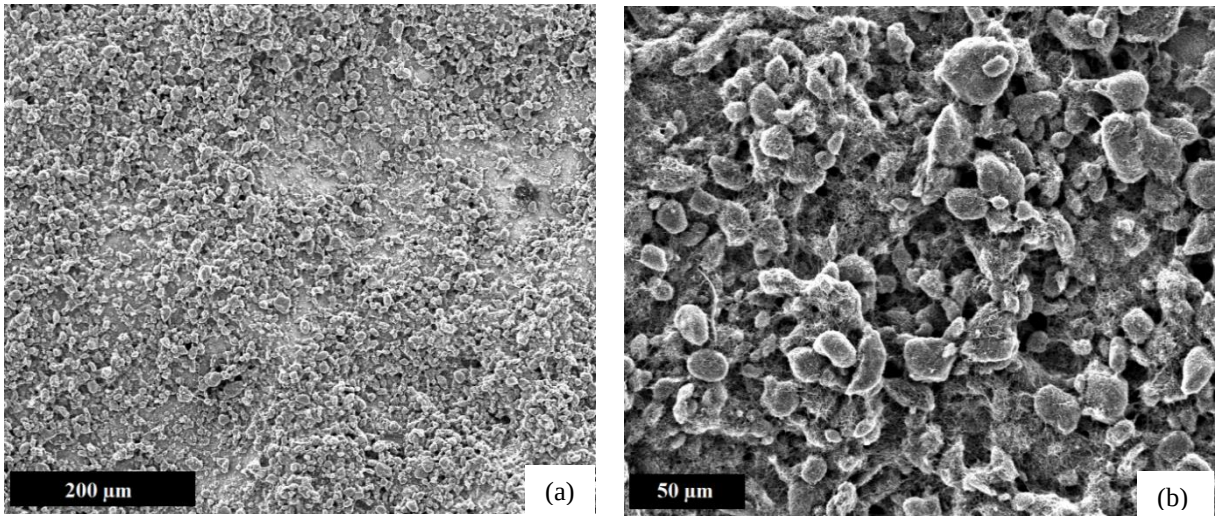

Fig. 5.17 – **(a)** Sample TRD1 surface at 200× magnification; **(b)** Sample TRD1 surface at 1000× magnification.

As **Fig. 5.18a** shows, the average coating thickness is 16.2 µm. It can already be stated that coatings done utilizing TEA produce thicker coatings compared to Mg-Nit coatings for identical deposition times. The increased thickness for same deposition times may be explained by the fact that effective electrical charge of the CNT's surface is higher. Therefore, with the same deposition time and electric field as for Mg-Nit, more CNT are transported towards the deposition electrode. Moreover, perhaps the transport load is lighter, presenting lighter ions, functional groups and/or atoms. This would allow more CNT to reach the deposition electrode under the same conditions.

When using TEA as an additive, the attained coating is approximately 30% thicker than coatings conducted using Mg-Nit as an additive, for the same deposition conditions. However, TEA coatings are significantly more porous. More pores are observed, and these pores are significantly larger than the pores observed for the Mg-Nit sample. As observed in **Fig 5.17a** and **Fig. 5.17b**, the coating is very irregular, presenting very different coating thicknesses in different regions of the cross-section. **Fig. 5.18b** shows a magnified image of pores present in the proximities of the substrate.

The inhomogeneous coatings may be a consequence of TEA's low stability. Once the CNT have been dispersed in the liquid medium, the TEA-doped CNT tend to re-agglomerate frequently, resulting in a more heterogeneous and porous coating. This is not

the case for Mg-Nit depositions, as the CNT tend to re-agglomerate at a much lower rate compared to TEA dispersions.

Consequently, not only do the re-agglomerated CNT produce a heterogeneous coating, but also produce a qualitatively weaker interface between the coating and the substrate. As shown in **Fig. 5.18b**, the interface presents large pores with very few CNT that have bonded with the surface of the substrate. Nonetheless, it is important to highlight that some CNT have in fact reacted with the surface forming a thin protective layer. Once again, in this figure some pores are indicated with arrows.

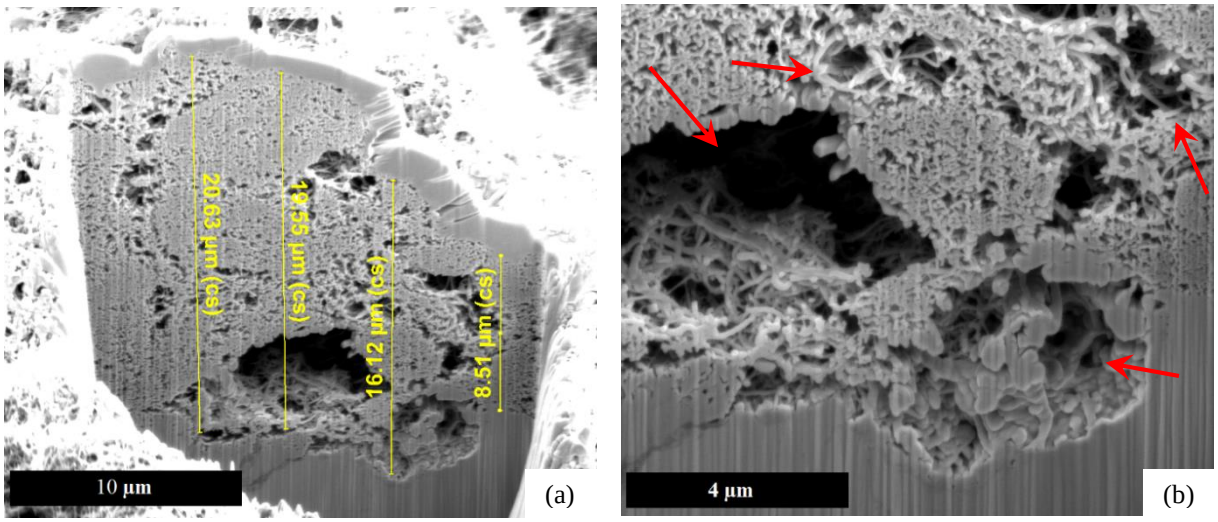

Fig. 5.18 – **(a)** Sample TRD1 cross-section at 5000× magnification; **(b)** Sample TRD1 cross-section at 12000× magnification. The red arrows indicate pours within the coating.

Sample DDRC4

The main difference between sample DDRC4 and the two previously studied samples, is that this sample is a double deposition and that this sample was post-processed in crude oil for four days. **Fig. 5.19a** and **Fig. 5.19b** show the surface of the sample with different magnifications. As was expected, the surface of sample DDRC4 is very similar to sample TRD1's surface, irregular and with CNT agglomerates. This is due to the fact that the outer layer of the double deposition is a TEA deposition. However, there are evidences of an improved compactness, likely resulting from the molecular cracking and integration of other elements stemming from the crude oil.

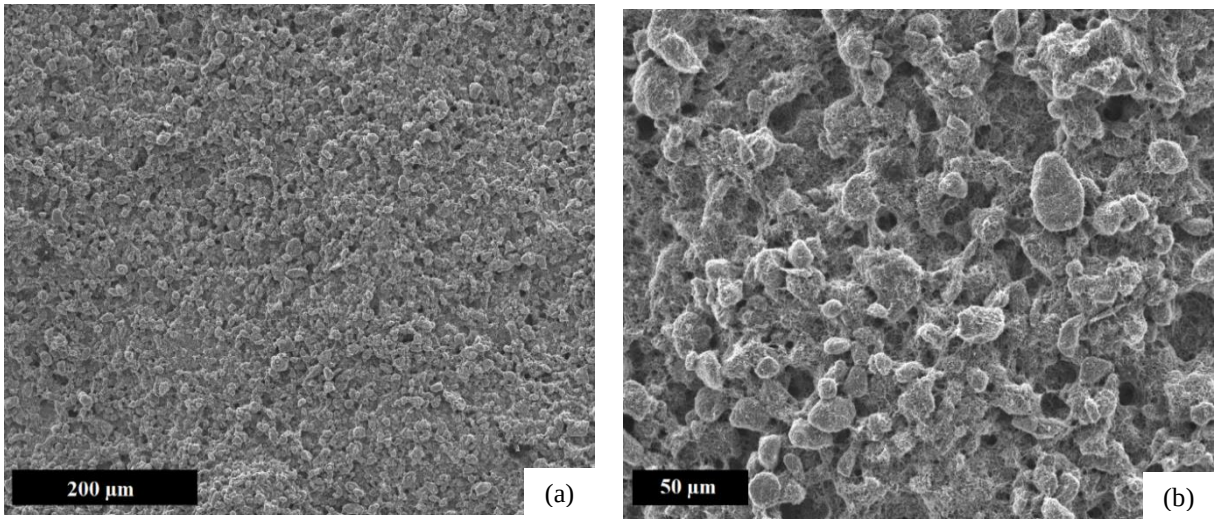

Fig. 5.19 – **(a)** Sample DDRC4 surface at 200× magnification; **(b)** Sample DDRC4 surface at 1000× magnification.

The overall deposition time for this sample is the same as for the previous two studied samples (five minutes), with three minutes of Mg-Nit and two minutes of TEA. For this reason, it is expected that the coating's thickness is at some point between the Mg-Nit coating and the TEA coating. As shown in **Fig. 5.20a**, this sample's coating thickness is in average 14 µm, thus proving that this coating is 11% thicker than the Mg-Nit coating and 14% thinner than the TEA coating and validating the initial hypothesis.

The cross-section view shows that this coating is more compact than the TEA coating. The overall porous network is very similar to the Mg-Nit coating. **Fig. 5.20b** shows the same image as **Fig. 5.20a** but without the thickness measurements to better visualize the pores present within the coating. A few of the pores are highlighted with arrows.

In regards to the interface between the substrate and the coating, it looks seamless, similarly to the MRD8 sample. This characteristic is expected since the innermost coating is a Mg-Nit deposition. Therefore, similar adhesive properties are expected. Furthermore, the interface between the two different coatings (Mg-Nit and TEA) is almost imperceptible. Demonstrating a very continuous adhesion between the differently-doped CNT. In the SEM image shown in **Fig. 5.20b**, the blue arrow shows the interface. This interface is detected by a slight change in the coating's contrast.

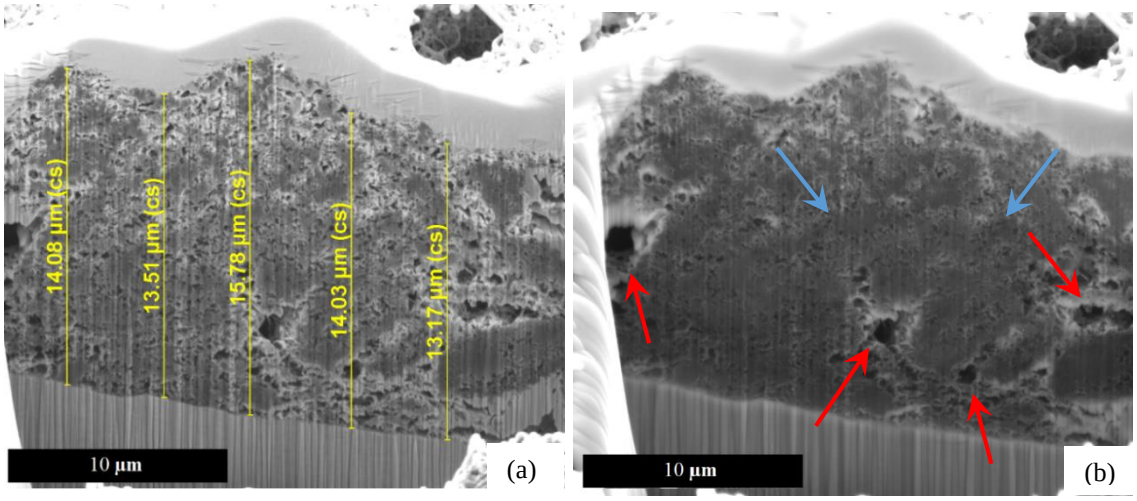

Fig. 5.20 – **(a)** Sample DDRC4 cross-section at 6500× magnification; **(b)** Sample DDRC4 cross-section at 6500× magnification. The red arrows indicate pours within the coating and the blue arrows indicate the interface between the Mg-Nit coating and the TEA coating.

5.2.3. Chemical analysis

The chemical analysis was conducted for samples MRD8, TRD1 and DDRC4. This technique is applied on the surface of the different samples to obtain a spectrum that shows the chemical elements present in the scanned region. Additionally, different map images may be attained depicting the spatial distribution of each element on the sample's surface. In this type of acquisition, the color intensity represents the spatial relative concentration of the element (nut not its global fraction).

The EDS map is acquired at 15 keV with a current of 22 nA, that generates a higher amount of counts (photons). The dwell time (time spent at each measuring spot) is set at 200 µs. Additionally, the final elemental map consists of the summation of sixteen acquired frames. The magnification used for each image is 500×.

Sample MRD8

Fig. 5.21 shows the EDS spectrum collected for sample MRD8. It can be seen that the main chemical element present are: carbon, magnesium, oxygen, nickel, iron and a small amount of silicon. Unmistakably, the carbon corresponds to the CNT and the magnesium detected is due to additive used. The iron, nickel, silicon and chromium detected correspond to substrate itself. The oxygen stems from the carboxy groups present in the CNT as a consequence of the CVD synthesis method, and to a minor extent, from light oxidation found on the sample's surface.

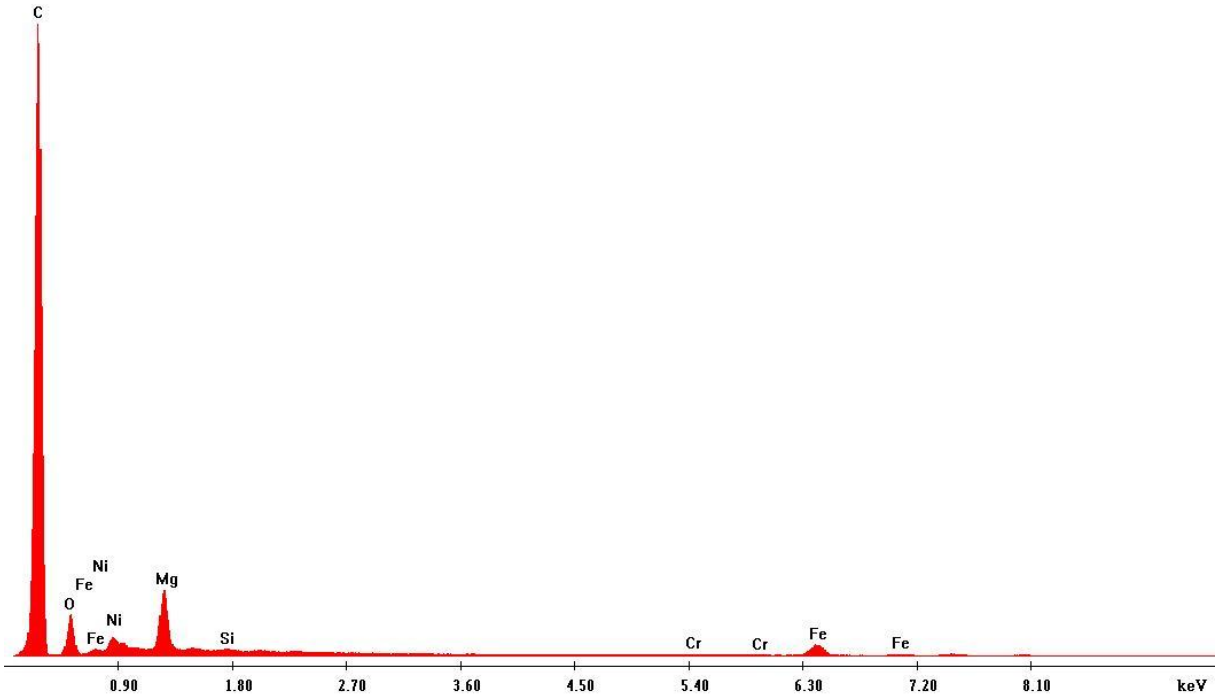

Fig. 5.21 - Chemical composition of sample MRD8's surface.

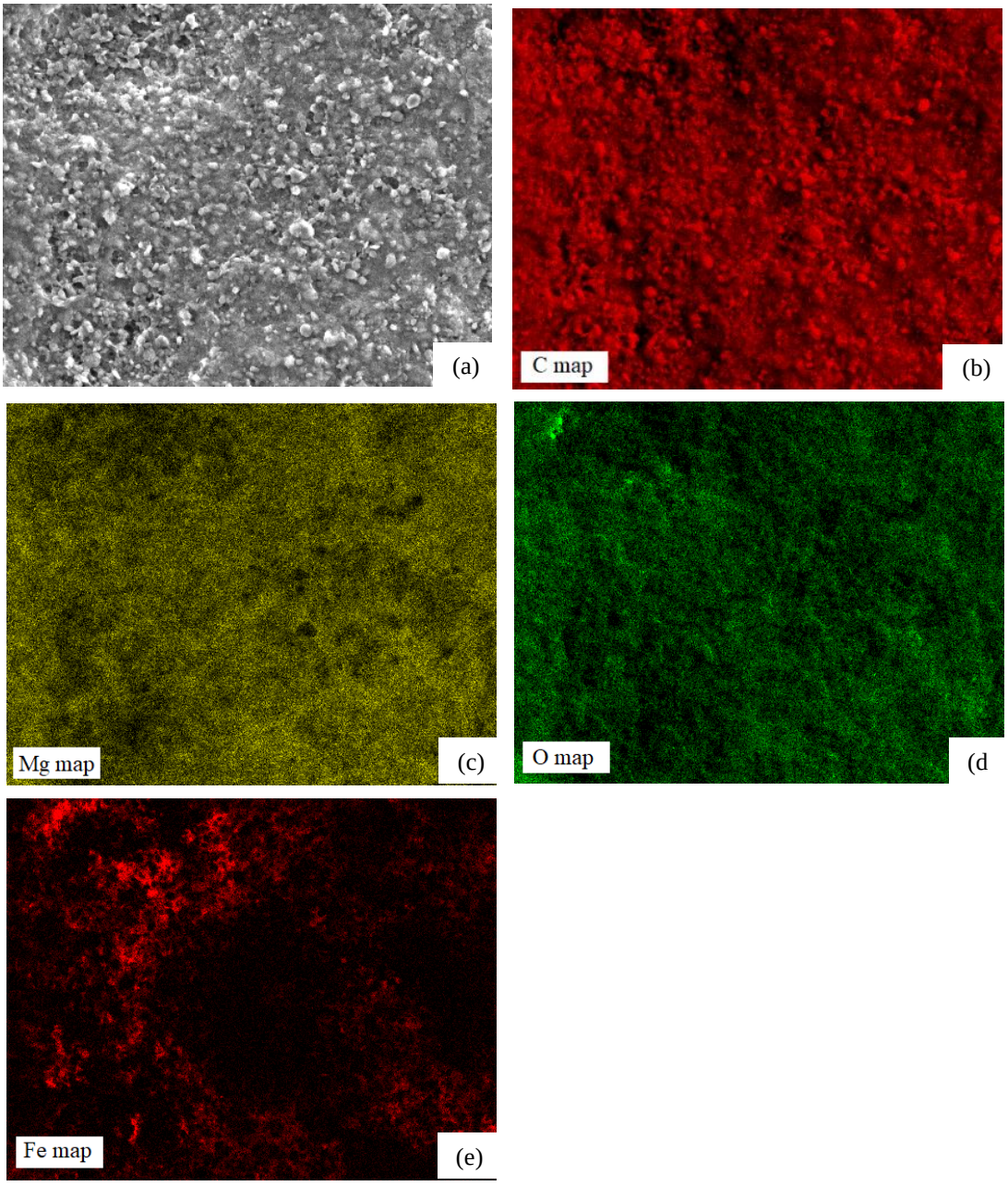

Fig. 5.22 – **(a)** SEM micrograph of sample MRD8's surface; **(b)** carbon EDS map; **(c)** magnesium EDS map; **(d)** oxygen EDS map; **(e)** iron EDS map.

Fig. 5.22a depicts an SEM micrograph of sample MRD8's surface, while **Fig. 5.22b-8e** depict the EDS maps of the different analyzed chemical elements. The pores present in the lower-left region of **Fig. 5.22a** are seen as well in **Fig. 5.22b** confirming the depletion of CNT in this region. Additionally, regions presenting large CNT agglomerates in **Fig. 5.22a** are shown a lighter shade of red in **Fig. 5.22b** verifying a larger carbon concentration in these regions. The EDS map in **Fig. 5.22c** proves that magnesium is found homogeneously distributed throughout most of the sample's surface.

Likewise, **Fig. 5.22d** shows the presence of oxygen throughout the surface of the sample. As already explained, this fact may have different sources, namely: the presence of carboxy groups bonded to the CNT, some degree of oxidation present in the sample's surface and/or the retention of oxygen in combination with the Mg^{2+} ions after the dissociation of the additive precursor. The iron signal shown in **Fig. 5.22e** proves that the penetration depth of the chemical analysis reaches the substrate. More specifically, it can be seen that the coating is thinner in the upper-left region since a stronger iron signal was detected.

Sample TRD1

Fig. 5.23 shows the EDS spectrum obtained for sample TRD1. As the spectrum shows, the most abundant element is again carbon, as was to be expected. Here, however, magnesium is not detected in accordance to the fact that TEA was utilized as an additive and not Mg-Nit. Oxygen is also detected, for similar reasons as explained for sample MRD8. The rest of the detected elements (iron, nickel, chromium and silicon) correspond to the substrate.

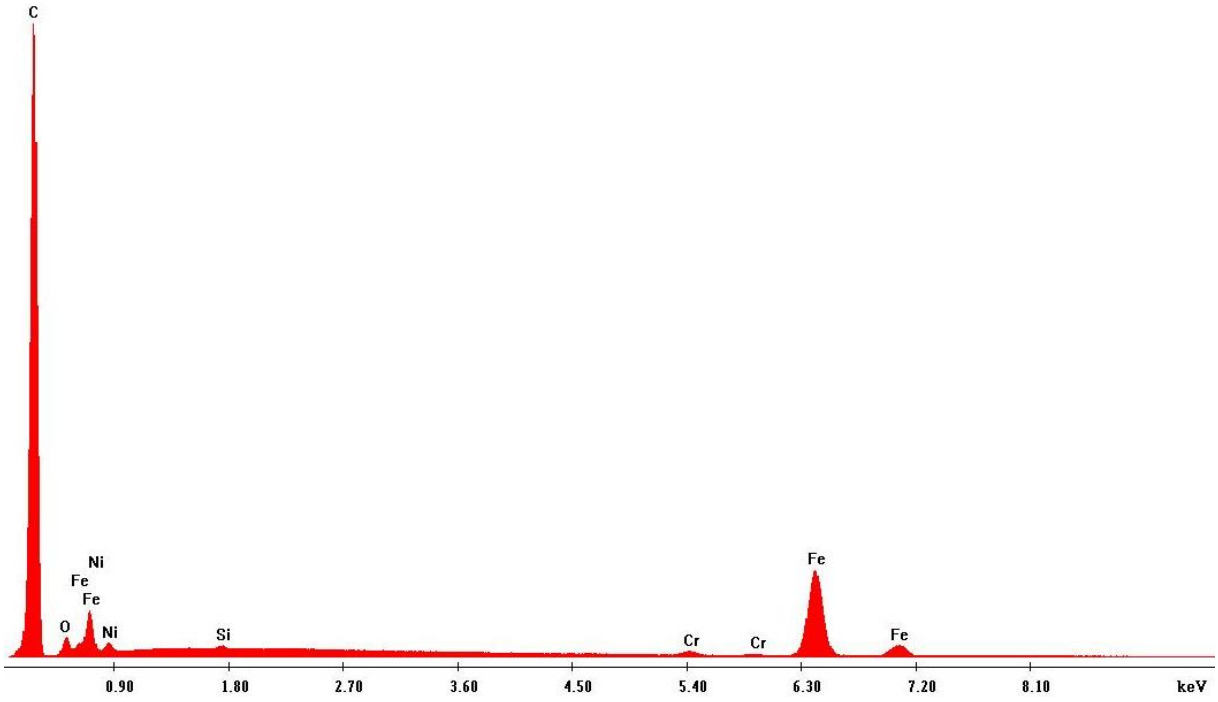

Fig. 5.23 - Chemical composition of sample TRD1's surface.

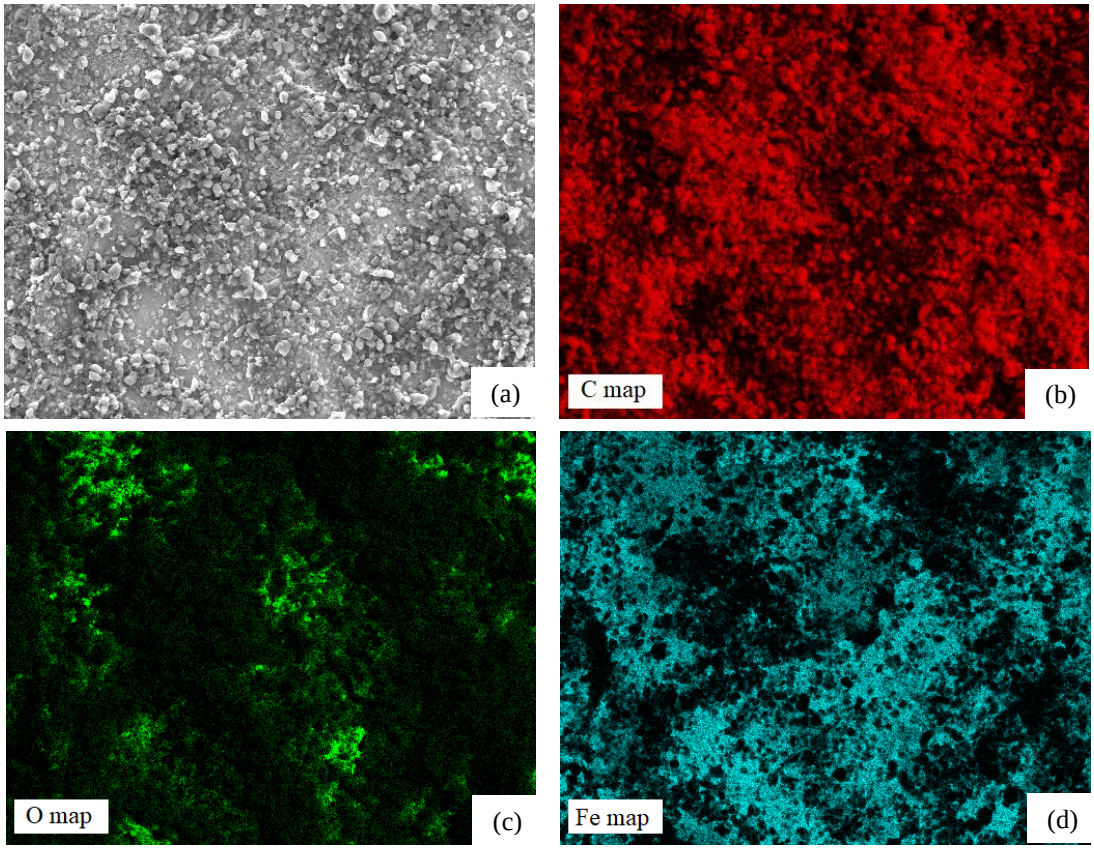

Fig. 5.24 – **(a)** SEM micrograph of sample TRD1's surface; **(b)** carbon EDS map; **(c)** oxygen EDS map; **(d)** iron EDS map.

As done for sample MRD8, **Fig. 5.24a** shows the SEM micrograph of this sample's surface. This sample does not present visible pores on its surface. However, it does present regions where the coating seems significantly thicker. These thicker regions are confirmed in **Fig. 5.24b** by showing a larger concentration of carbon compared to regions where the coating seems thinner. The dark regions in **Fig. 5.24b** proves that some regions of the surface possess very little amount of CNT. The oxygen EDS map shown in **Fig. 5.24c** is particularly interesting when compared to the carbon EDS map from **Fig. 5.24b**. From the comparison, one may observe that regions with lower amounts of carbon possess a higher amount of oxygen, and vice versa. From this observation, it can be deduced that the oxygen content detected is primarily due to the oxidation on the sample's surface. The iron map shown in **Fig. 5.24d** further supports this observation, by showing a weaker intensity where the highest carbon concentration has been observed.

Sample DDRC4

As explained in *section 4.6.4*, sample DDRC4 has underwent the oil post-processing for four days. For this particular reason, it is of special interest to obtain the EDS map to study the difference in chemical composition generated by said process. **Fig. 5.25** shows the EDS spectrum collected for this sample. As this figure shows, carbon is again the primarily detected element, which is to be expected. Additionally, since this coating is a double deposition, magnesium is detected along with oxygen, iron, nickel and silicon. The main difference between this sample and the previous two is the observation of sulfur. The detected sulfur is either a consequence of remnant crude oil within the coating, or the sulfur present in the crude oil reacted with the CNT coating during the process. In the spectrum shown in **Fig. 5.25** platinum and gallium have been detected, being both present as a result of the FIB characterization.

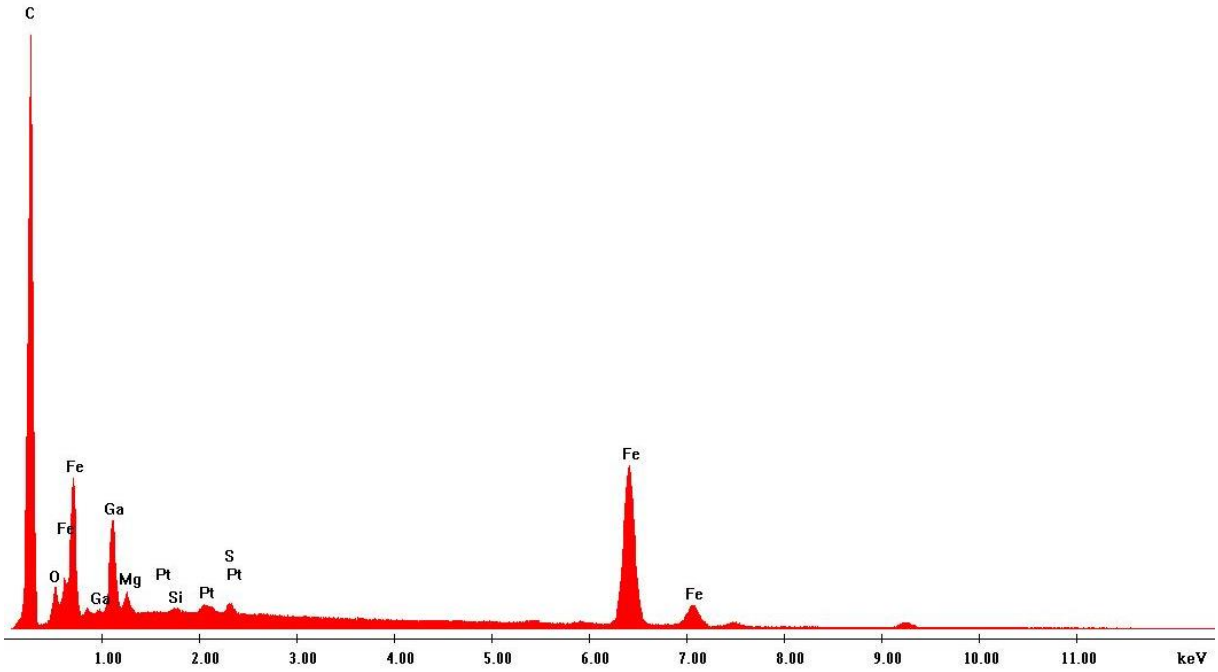

Fig. 5.25 - Chemical composition of sample DDRC4's surface.

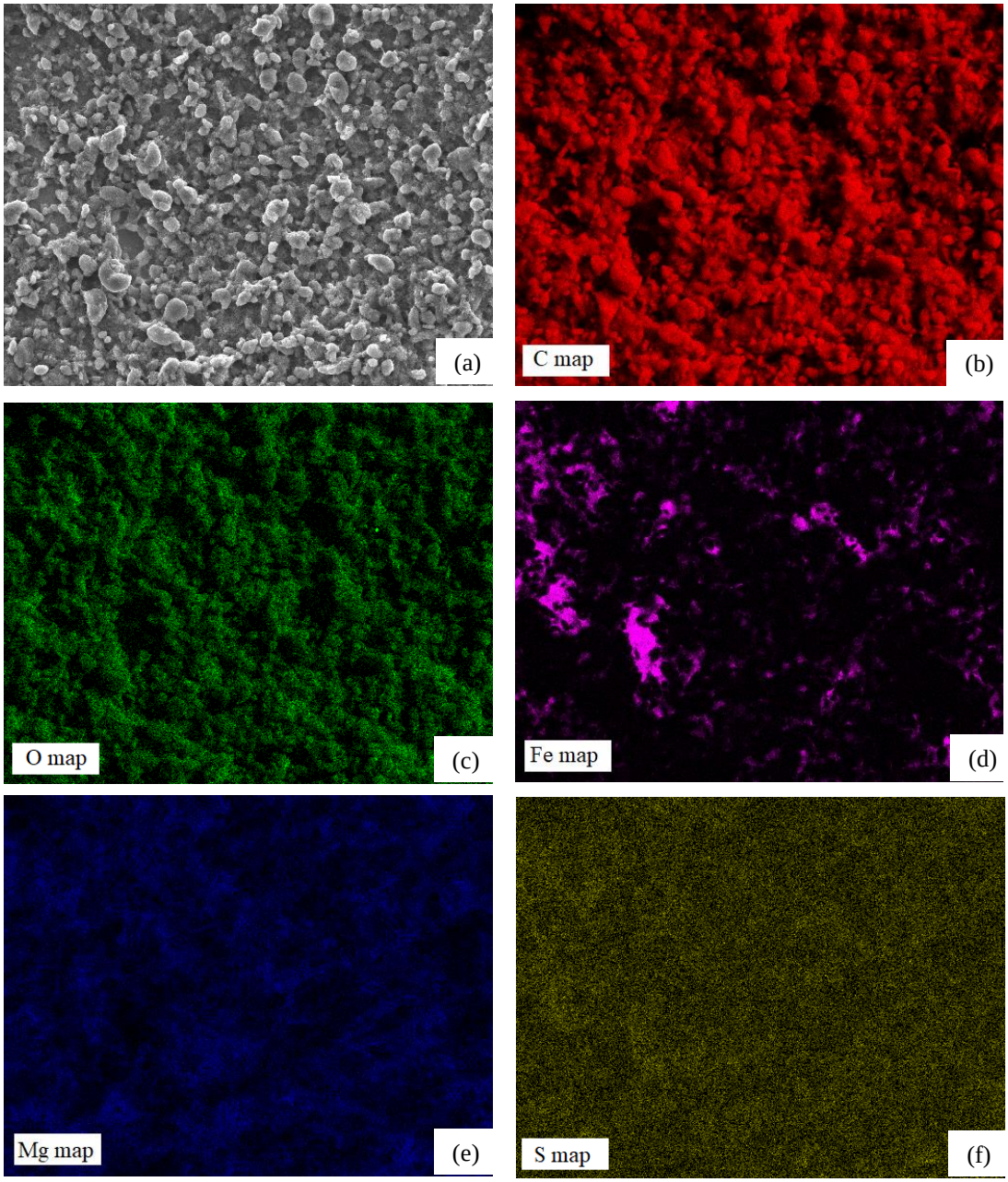

Fig. 5.26 – **(a)** SEM micrograph of sample DDRC4's surface; **(b)** carbon EDS map; **(c)** oxygen EDS map; **(d)** iron EDS map; **(e)** magnesium EDS map; **(f)** sulfur EDS map.

For this sample in particular, the chemical analysis has been carried out in two different configurations. The first consisted of the acquisition of the superficial elemental maps, whereas the second was a concentration profile analysis in a cross-section. **Fig. 5.26a-5.26f** show the EDS maps collected for the first region. In this case, only carbon, oxygen, magnesium, iron and sulfur are of interest.

Fig. 5.26a shows the SEM micrograph of the first scanned region. Similarly to the previously analyzed samples, **Fig. 5.26b** shows the locations where carbon is present in the sample's surface. Comparing **Fig. 5.26a** and **Fig. 5.26b** it is clear to see that the

regions with large CNT agglomerates have a higher concentration of carbon, and regions with fewer carbon concentration represent the depletion of CNT. Additionally, those regions with low carbon content, present a strong iron signal. In **Fig. 5.26c**, it can be seen that the oxygen content is mainly present in regions with higher CNT agglomerates. Therefore, it can be concluded that it is detected as a cause of the CNT functionalization and not because of the substrate's oxidation. Since this coating is a double deposition, the surface of the sample is entirely covered with magnesium, as **Fig. 5.26e** shows. Lastly, **Fig. 5.26f** shows the EDS map of sulfur, chemical element which is not present in samples MRD8 and TRD1. It is thus assumed that it stems from the chemical interaction between the crude oil and the coating. Furthermore, it is evident the sulfur content of the coating is homogeneously distributed throughout the whole region analyzed.

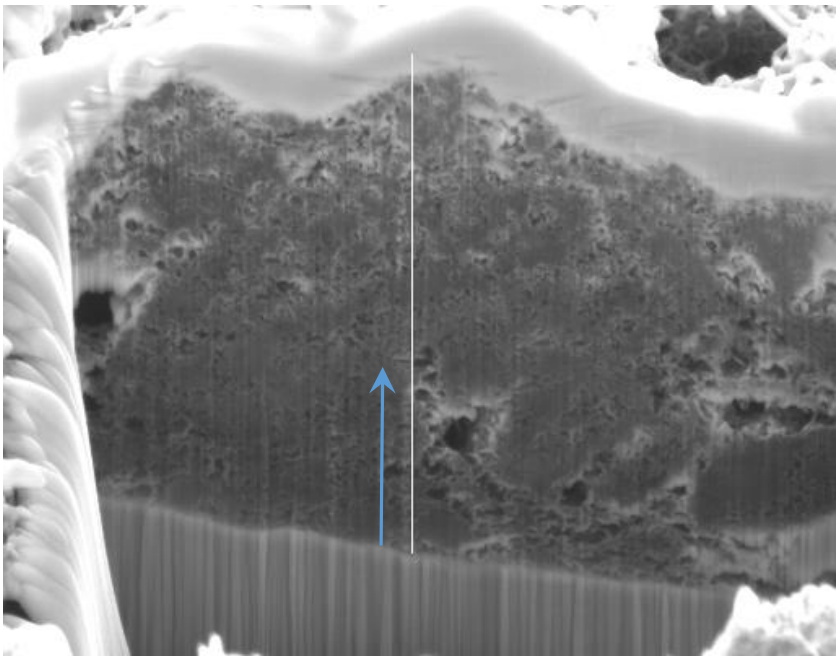

Fig. 5.27 - FIB cross-section of sample DDRC4 with linear trajectory for chemical analysis.

Along with the EDS maps, it is interesting to analyze how the chemical composition of the coating changes as it is deposited and how the post-processing modifies its chemical composition. This analysis is achieved by applying an EDS line scan along the cross-section. **Fig. 5.27** shows a SEM image of the cross-section utilized to analyze the chemical composition, the line that was analyzed and the arrow indicates the scan direction (from the substrate's surface upwards towards the coating's surface).

The elements of interest are: carbon, oxygen, magnesium and sulfur. **Fig. 5.28a-5.28d** show the linear chemical composition of the same sample, in the same location for

these four elements. **Fig. 5.28a** shows the chemical composition of carbon along the linear trajectory. Carbon is found throughout the entire coating with only marginal variations. As soon as the scan begins, the amount of carbon detected sharply increases. The counts vary, however the amount of carbon detected is somewhat similar from beginning to end. **Fig. 5.28b** shows the oxygen content present in the coating. It can be immediately noticed that the oxygen content varies significantly throughout the coating. In proximities of the substrate, the oxygen content is extremely high. However, as the scan progresses, the oxygen content sharply decreases and remains fairly constant for all thicknesses. This effectively proves that the vast majority of the oxygen detected in the EDS maps is due to the substrate's oxidation, and a small amount is detected from the carboxy groups. **Fig. 5.28c** shows the magnesium concentrations detected for different coating thicknesses. Unsurprisingly, there is a high magnesium content in the proximities of the substrate, since the lower part of the coating was deposited using Mg-Nit as an additive. However, even in the outermost regions of the coating, a considerably high content of magnesium is detected even though this section of the coating was deposited using TEA as an additive. Finally, **Fig. 5.28d** shows the sulfur content present in the coating. Unexpectedly, a considerably high amount of sulfur is detected in the interface between the substrate and the coating. The sulfur concentrations gradually decreases until it becomes constant at about halfway through the coating. Near the surface however, the amount of sulfur detected strongly increases. This indicates that during the post-processing, the crude oil was able to infiltrate the coating and reacted with the species present in the carbon. This statement is supported by the fact that hydrocarbons tend to show a good wetting compatibility with carbonaceous coatings (oleophilicity). Another important conclusion that can be drawn from this is that, irrespective of the additive used for the deposition, the post-processing with crude oil would effectively interact with the whole coating.

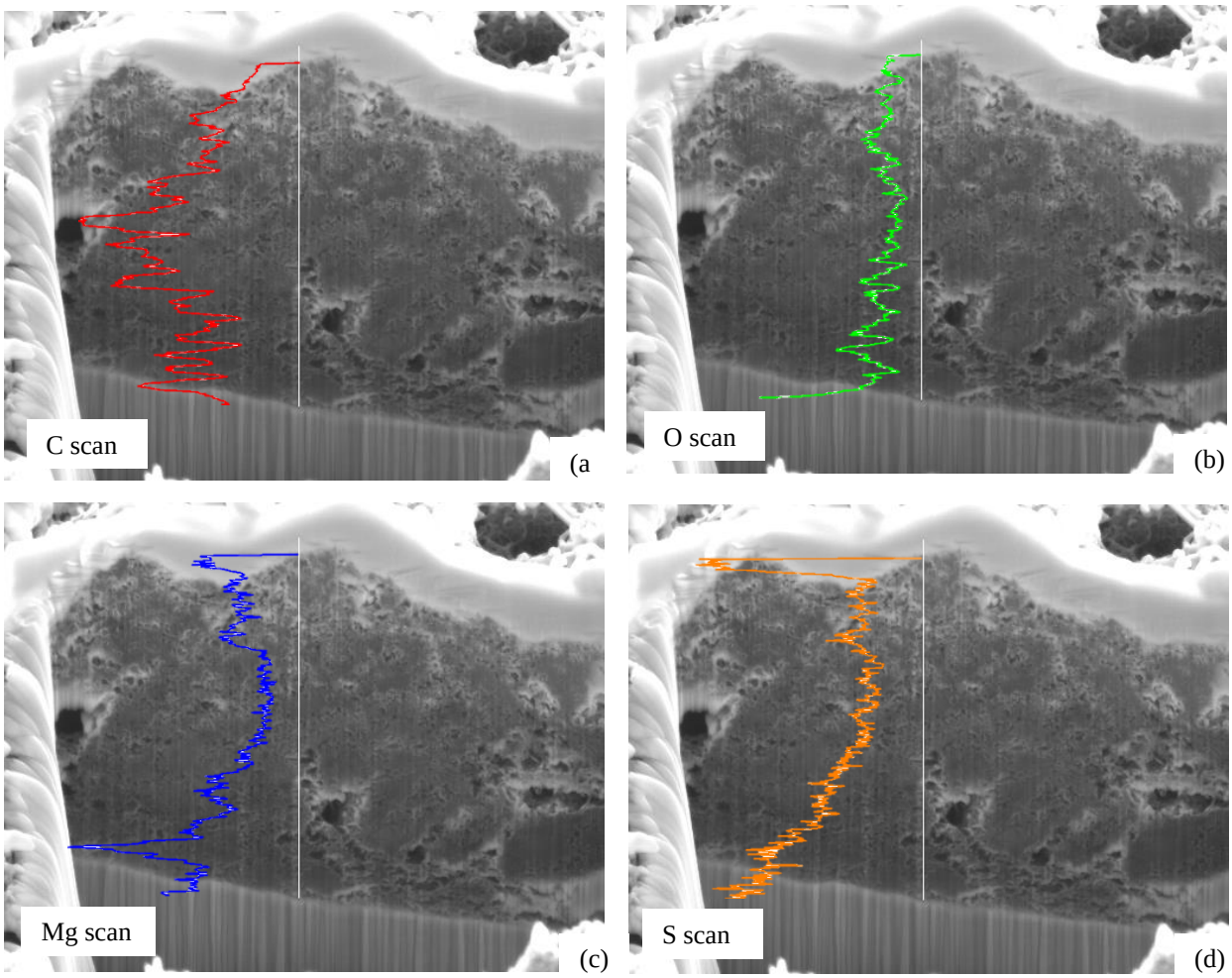

Fig. 5.28 – **(a)** carbon detected along a linear trajectory; **(b)** oxygen detected along a linear trajectory; **(c)** magnesium detected along a linear trajectory; **(d)** sulfur detected along a linear trajectory.

5.2.4. Wettability (sessile drop test)

Sessile drop test is a study that determines the wetting behavior of different surfaces. In this section, four different surfaces are analyzed. To begin with, a reference sample is studied to determine the contact angle that is formed with the surface of the steel substrate. With the substrate's surface analyzed, three different coatings are tested. The samples studied are: Mg-Nit3, M2-1, M5-1, TEA3, T2-2, T2-4 and DD10. The study of these three different surfaces is key to determining the best coating for this particular application. Since the wetting behavior of the surface is significantly influential on the anticorrosive properties of the coating, the coating that produces the highest contact angle is expected to be the one that presents the best protection in terms of corrosion.

The images shown in this section illustrate the contact angle that a water drop forms with the surface of the sample studied. The fluid used is deionized water with a volume of 3 µL, unless specified otherwise. The choice of the volume is not arbitrary,

since very small volumes render the effect of the droplet's own weight negligible. During the analysis, a red line will be placed in the image to clarify the baseline used for the determination of the contact angle. Furthermore, the blue line in the image show the tangent lines that the computation software uses to determine the contact angle formed between the droplet and the sample's surface. Additionally, each measurement is take after the drop comes into contact with the surface. In regards to the computational method, all measurements obtained with the computational method "circle" in the Krüss calculation software.

Additionally, the contact angle measurements have been taken for the right and left side of the droplet. However, no shape anisotropies in the droplet have been detected with the resolution limits of the sessile drop test. Therefore, all contact angle values showed in this section are the same for the right and left side of the droplet.

Reference sample

The reference sample is a standard type 2 sample obtained from the sucker rod. Before this sample's wetting behavior was studied, the sample underwent the cleaning process described in *section 4.2*. **Table 5.17** summarizes the contact angle values obtained for the reference sample. As this table shows, the values obtained are range from 72° to 82°, resulting in an average value of about 74° with a standard deviation of 4.4°.

Table 5.17 – Reference sample contact angle measurements.

Measurement	Contact angle /°
1	81.9
2	75.4
3	72.1
4	68.8
5	73.6
6	73.4
Average	74.2
Standard deviation	4.4

As explained before, these measurements were taken to find the starting point. With these reference values, one is able to evaluate if the different coatings applied to the

substrate improve the system's wettability or diminish its characteristics **Fig. 5.29** shows the image used to determine the fifth contact angle measurement (73.6°).

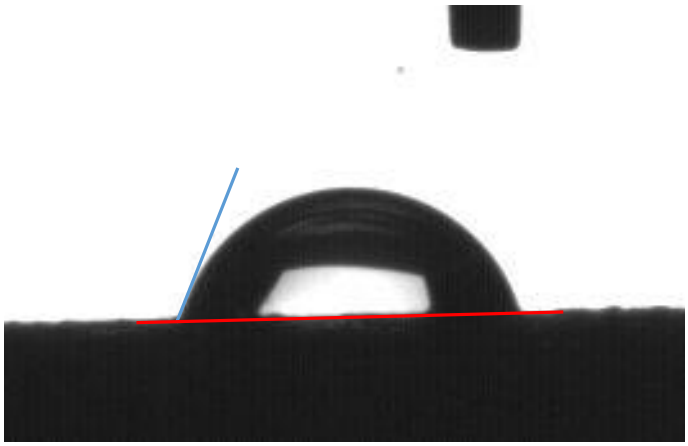

Fig. 5.29 - Contact angle of 73.6° for reference sample. The red line indicates the object baseline and the blue line the tangent to the deposited droplet.

Mg-Nit samples

The first coating studied is deposited via the use of Mg-Nit as an additive. Without a post deposition process, coatings deposited with this additive are usually hydrophilic due to the interaction between the droplet and the magnesium ions (Mg^{2+}). **Table 5.18** summarizes results for an as-deposited Mg-Nit sample. As expected, the measurements acquired present low contact angles which are significantly below those from the reference sample. Therefore, this coating would weaken the system's corrosion protection since the corrosive medium would infiltrate the coating and become in contact with the steel. The average contact angle value obtained is approximately 35°, with a standard deviation of 6°, representing a hydrophilic wetting behavior. **Fig. 5.30** shows the image utilized to determine the contact angle of the fifth measurement (34.1°).

Table 5.18 – Mg-Nit3 sample contact angle measurements.

Measurement	Contact angle /°
1	35.2
2	44.4
3	30.3
4	29.2
5	34.1
Average	34.6
Standard deviation	6.0

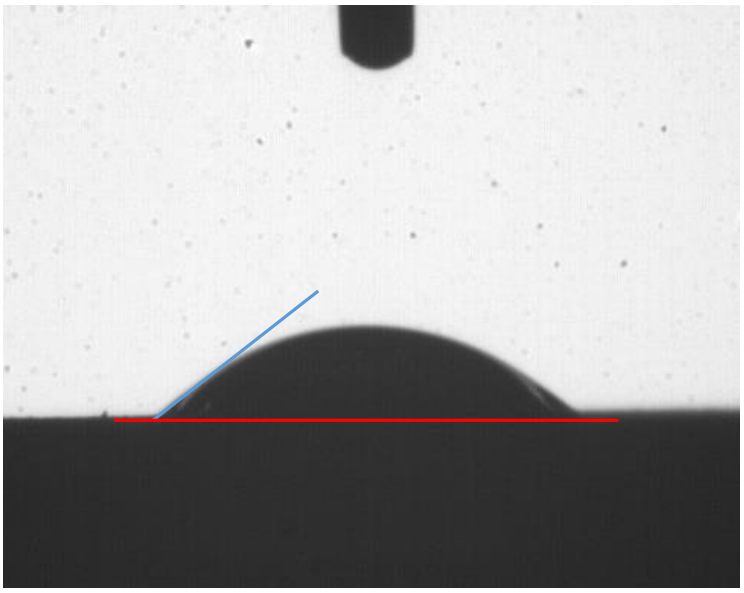

Fig. 5.30 - Contact angle of 34.1° for Mg-Nit3 sample. The red line indicates the object baseline and the blue line the tangent to the deposited droplet.

If a post-deposition cooking process is conducted, as described in *section 4.6.4*, the contact angle measurements obtained for Mg-Nit samples significantly improve compared to the as-deposited samples. This M2-1 sample was cooked in crude oil for one day at 80°C, and later dried for four hours at 200°C, with a deposition time of two minutes. The results obtained are summarized in **Table 5.19**. After this process, the average contact angle is approximately 116° with a standard deviation of 2.3°. This increase in contact angle represents about a 230% improvement, transforming a hydrophilic coating into a hydrophobic one. With this change, the new Mg-Nit coating is indeed a viable option for effectively protecting the coated substrate. The image used to determine the seventh measurement is shown in **Fig. 5.31**. The improved hydrophobicity

of the cooked samples is explained by molecular sulfur found in these coatings [69]. Alone, CNT are hydrophobic [2]. However, the additives that are used to deposit the CNT on the substrate's surface make the CNT reactive, reducing their hydrophobicity.

Table 5.19 – M2-1 sample contact angle measurements.

Measurements	Contact angle /°
1	118.2
2	118.0
3	119.3
4	115.0
5	115.5
6	112.8
7	115.6
Average	116.3
Standard deviation	2.3

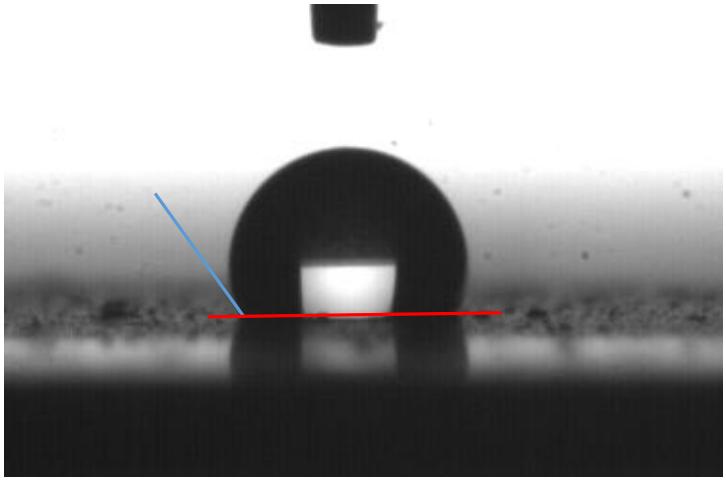

Fig. 5.31 - Contact angle of 115.6° for sample M2-1. The red line indicates the object baseline and the blue line the tangent to the deposited droplet.

As explained in *section 4.8.2*, for Mg-Nit samples, the thickness of the coating is the determining factor for wetting behavior improvements. Consequently, yet another sample (M5-1) was studied after cooking for one day. The cooking and drying parameters are identical to those utilized for M2-1. However, this sample possesses a coating that was deposited for five minutes. The results obtained for M5-1 sample are shown in **Table 5.20**. As this table shows, the average contact angle for this sample is approximately 145° with a standard deviation of 1.3°. This value corresponds to a 25% increase in contact

angle compared to M2-1 and 314% improvement compared to Mg-Nit3 sample. This increased value proves that in the case of Mg-Nit samples, maintaining the cook time constant, the thickness of the coating is a key factor in determining the wetting behavior of the coating. With thicker coatings and relatively short cooking periods, the coating shifts to a strong hydrophobic behavior. **Fig. 5.32** shows the image used to determine the second measurement.

It is of utmost importance to clarify that these contact measurements correspond to a higher droplet volume. The volume was increased from 3 µL to 9µL. This was done due to the fact that during the measuring process, the droplet would not adhere to the surface of the coating. Therefore, the volume must be increased. With this larger volume, the gravitational effects on the droplet force it to fall off the needle and it is deposited over the coating's surface. Furthermore, as a consequence of this higher droplet volume, the droplet possesses an elliptical contour. This elliptical shape of the droplet introduces an error into the measurement which cannot be removed. Consequently, the real contact angle for the M5-1 sample is expected to be slightly higher than the 145° measured. Evidently a higher contact angle is desired, therefore this source of error does not negatively affect the decision-making process, in terms of choosing the most adequate protective coating.

Table 5.20 – M5-1 sample contact angle measurements.

Measurements	Contact angle /°
1	143.8
2	145.2
3	145.5
4	143.4
5	147.3
6	144.4
7	145.0
Average	144.9
Standard deviation	1.3

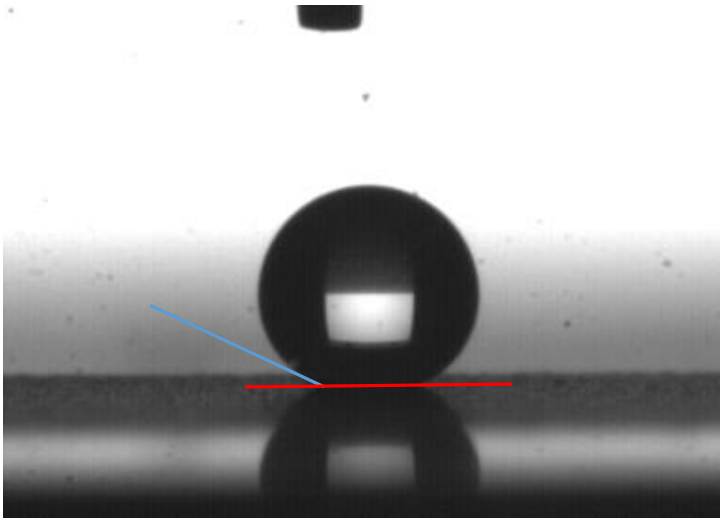

Fig. 5.32 - Contact angle of 145.2° for sample M5-1. The red line indicates the object baseline and the blue line the tangent to the deposited droplet.

TEA samples

Coatings deposited using TEA as an additive present outstanding wetting behavior without the need of post deposition processing, generating a near super-hydrophobic coating. This hydrophobicity is a consequence of the total removal of TEA from the coating's surface since TEA is polar by nature [2]. However, the rinsing process after deposition removes any residual TEA on the coating's surface leaving behind the hydrophobic (non-polar) CNT. **Table 5.21** summarize the contact angle measurements acquired for an as-deposited TEA coating. As it can be seen, this coating presents an average contact angle of about 140° with a standard deviation of 4°. When compared to the Mg-Nit sample, this coating presents a fourfold improvement of the contact angle without any additional post deposition processes. **Fig. 5.33** shows the image used to determine the fifth measurement acquired. Similarly as it occurred for sample M5-1, these contact angle measurements were conducted with a droplet volume of 9 µL. Therefore, the actual contact angle that the droplet forms with the coating's surface is expected to be slightly higher than 140°.

Table 5.21 – TEA3 sample contact angle measurements.

Measurements	Contact angle /°
1	138.1
2	137.3
3	137.0
4	146.6
5	138.6
Average	139.5
Standard deviation	4.0

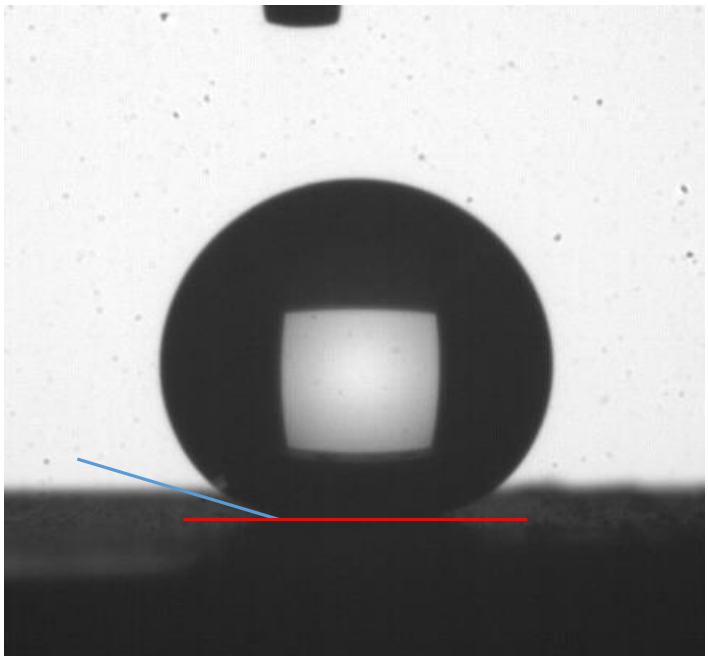

Fig. 5.33 - Contact angle measurement of 138.6° for TEA3 sample. The red line indicates the object baseline and the blue line the tangent to the deposited droplet.

Although sample TEA3 presents exceptional hydrophobicity (near super-hydrophobic behavior), this coating's adhesion is insufficient. The coating itself is extremely fragile, and great care must be taken to maintain the coating's structural integrity. Nonetheless, a similar post deposition process as for the Mg-Nit samples is conducted to observe if any enhancements are measureable. Sample T2-2 is a TEA deposition that lasted two minutes and has been cooked in crude oil for two days. The contact angle measurement results are displayed in **Table 5.22**. As this table shows, the

average value is approximately 115° with a standard deviation of 1.8°. **Fig. 5.34** shows the image utilized to measure the fourth value.

When comparing T2-2 with TEA3, it can be noted that the contact angle drops with the cooking process. However, the decrease in angle is only about 18%, and the final result is still a hydrophobic coating. At cost of this 18% hydrophobicity, a gain in adhesion is acquired. The coating becomes less fragile, facilitating sample manipulation. A more robust coating is desired because hydrophobicity is not an effective protective mechanism if the coating is easily removed by scratches, vibrations or impacts. Therefore, the loss in hydrophobicity is within a certain tolerance since the gain in adhesion complements the coating, generating a system that is better fit to protect the substrate from corrosive agents.

Table 5.22 – T2-2 sample contact angle measurements.

Measurements	Contact angle /°
1	117.2
2	116.7
3	116.1
4	115.5
5	114.4
6	112.6
7	113.0
Average	115.1
Standard deviation	1.8

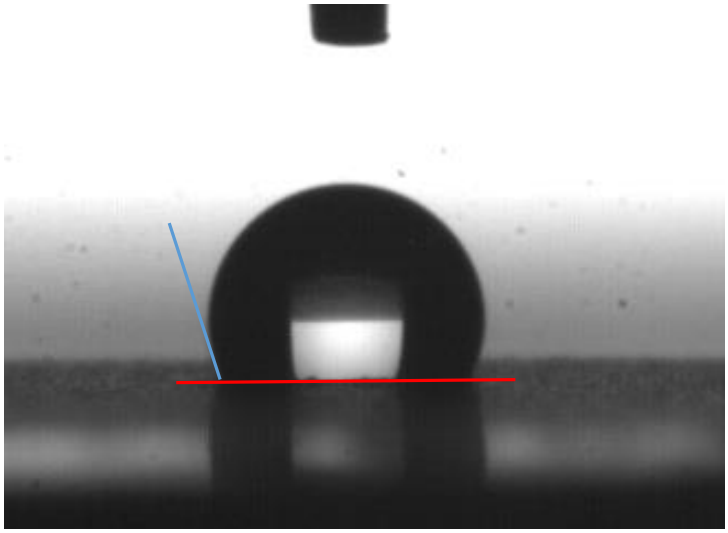

Fig. 5.34 - Contact angle of 115 for T2-2 sample. The red line indicates the object baseline and the blue line the tangent to the deposited droplet.

In pursuit of recuperating some hydrophobicity while maintaining the gain in adhesion, sample T2-4 is a TEA deposition with a duration of two minutes that has been cooked in crude oil for four days. All other cooking parameters are identical, as was explained for previous samples. **Table 5.23** summarizes the contact angle values obtained for sample T2-4. As this table shows, the average contact angle is approximately 137° with a standard deviation of 1.6°. **Fig. 5.35** displays the image used to measure the second value. This improvement in contact angle for prolonged post-deposition processes may be due to a stronger influence of sulfur in the coating's surface, providing a more hydrophobic surface.

This sample proves an improvement when compared to T2-2 while maintaining the adhesion properties of the latter. The contact angle values obtained are very similar to the as-deposited sample (TEA3).

Table 5.23 – T2-4 sample contact angle measurements.

Measurements	Contact angle /°
1	137.6
2	137.4
3	139.4
4	138.1
5	135.7
6	135.7
7	134.7
Average	136.9
Standard deviation	1.6

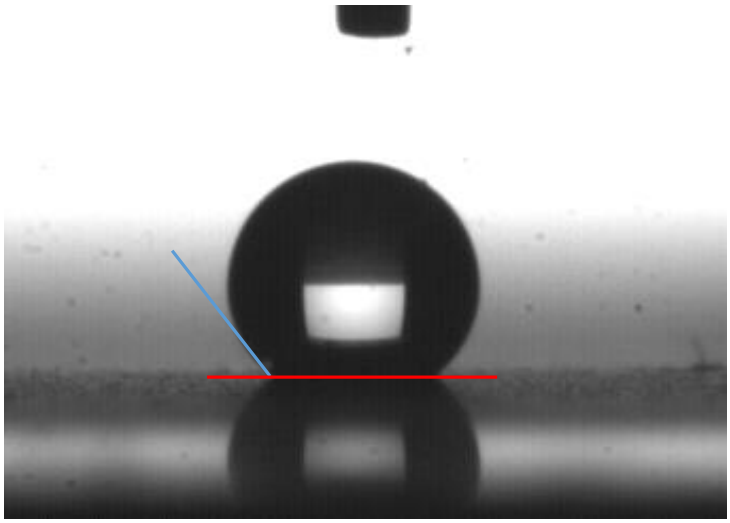

Fig. 5.35 - Contact angle of 137° for sample T2-4. The red line indicates the object baseline and the blue line the tangent to the deposited droplet.

As explained in *section 4.8.2*, for TEA deposited coatings, the main parameter is cook time. The thickness of the coating is not as relevant, with the only requirement being that the entire surface of the substrate must be completely coated. If this requirement is met, the thickness is not relevant in regards to hydrophobicity. Cook time on the other hand does influence the observed contact angle. This is demonstrated by comparing samples T2-4 and T2-4. Both samples possess similar thicknesses since both coatings were deposited for two minutes. The main difference between these two samples is the cook time, the first sample was cooked for two days and the second for four. With sample T2-4, a high grade of hydrophobicity is achieved, while maintaining the adhesion improvements that T2-2 demonstrated.

Double deposition sample

Double deposition coatings were devised to combine the best characteristics from both additives. The lower layer of the coating was a Mg-Nit deposition due to this coating's enhanced adhesion behavior resulting from the formation of the holding layer. To improve on this Mg-Nit coating, a thin layer of TEA is deposited over it. This outermost layer provides the hydrophobicity that the Mg-Nit coating lacks. Therefore, the resulting coating would ideally present a proper adhesion and its top layer would be hydrophobic.

Having said that, **Table 5.24** summarizes the contact angle measurements obtained for a double deposition coating. The Mg-Nit layer was deposited for four minutes, while the outer TEA layer was deposited for 1 minute.

As this table shows, the average contact angle for this sample is about 141° with a standard deviation of 4°. These measurements effectively prove that the contact angle obtained corresponds to the outer TEA layer. Therefore, this coating would be a strong candidate to be used for corrosion protection, since it may prevent corrosive media from coming into contact with the steel substrate. **Fig. 5.36** displays the image utilized to determine the third measurement. In all measurements, 9 µL were used to determine the contact angle as a consequence of the surface's hydrophobicity.

Table 5.24 – DD10 sample contact angle measurements.

Measurements	Contact angle /°
1	144.4
2	137.9
3	143.3
4	136.7
5	134.8
6	144.9
7	141.7
Average	140.5
Standard deviation	4.0

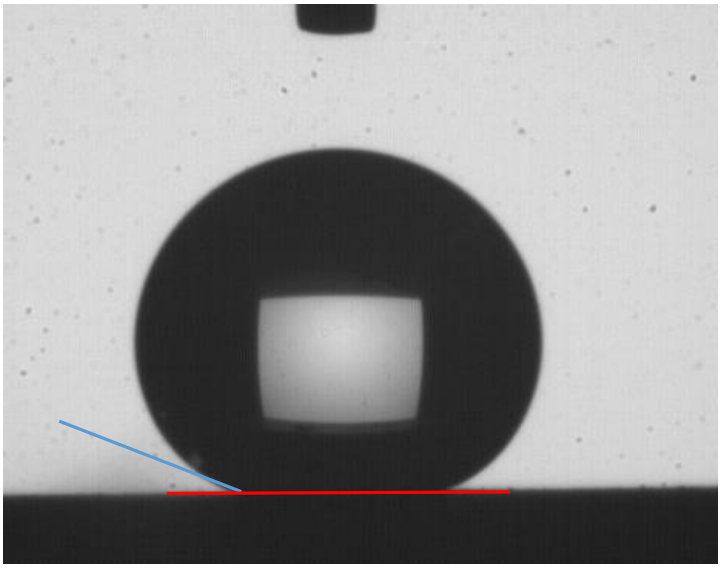

Fig. 5.36 - Contact angle measurement of 143.3° for DD10 sample. The red line indicates the object baseline and the blue line the tangent to the deposited droplet.

Salt water measurements

Additionally from the deionized water droplets used to measure contact angle on the different samples, measurements were conducted utilizing a saltwater solution. The water quality [70] and salt type and concentration to prepare the solution respect the requirements specified in ASTM standard [71].

The measurements conducted utilizing the saltwater solution do not show significant differences compared to the deionized water results. This may be a consequence of the negligible variation in surface tension due to the miniscule amount of salt added to the deionized water. Therefore, the results obtained when measuring with saltwater are not exposed as they do not present any insight.

Differences measured varying droplet volume

To quantify the difference in contact angle when measured with 3 µL and 9 µL, the same sample was studied with both volumes. The results obtained are shown in **Table 5.25**. As this table shows, the average difference is approximately 9° with differences ranging between 4° and 13°. However, the most valuable piece of information that can be extracted from these results is the fact that the volume decreases the contact angle measured. Therefore, it is proven that the contact angle measurements obtained for samples TEA 3 and DD10 are indeed lower than the real contact angle.

Table 5.25 – Differences observed with different droplet volumes.

Measurement	3 µL	9 µL	Difference /°
1	146.6	136	10.6
2	140.4	136.1	4.3
3	144.3	130.7	13.6
4	145	136	9
Average	144.1	134.7	9.4
Standard deviation	2.6	2.7	3.9

6. Concluding Remarks & Outlook

Carbon nanotubes have been successfully deposited on steel samples extracted from sucker rods, with the aim of protecting them from corrosion during transport. Three different coating systems have been studied in these terms. Although coating adhesion to the substrate has not been individually tested, it is analyzed by observing the fragility that the coating presents when manipulating the coated samples.

The Mg-Nit system post-processed with crude oil presents outstanding wetting properties, especially when compared to the Mg-Nit as-deposited samples. The as-deposited sample has a hydrophilic behavior, measuring a contact angle of 35°. In this case, the Mg-Nit coating diminishes the wetting behavior of the substrate, as this coating makes the surface more hydrophilic. After a post-deposition cooking procedure, the contact angle measured for these samples increases by 230%, with contact angle measurements that surpass 116°. Additionally, for Mg-Nit depositions, there is a tendency toward the coating becoming more hydrophobic as the thickness increases. The time that the sample is cooked does not significantly alter the contact angle measurements. However, it is of utmost importance that this step is taken, since it greatly affects the results obtained. The thickness of the coating on the other hand, does affect the measurements. When comparing two post-processed Mg-Nit samples with different thicknesses, the thicker coating presents a 25% increase in contact angle (145°). The thickest post-processed sample shows improvements of 314% compared to the as-deposited Mg-Nit coating.

The coating obtained with as-deposited Mg-Nit presents adequate adhesion in terms of fragility. This coating's adhesive characteristics are primarily based on the formation of a $Mg(OH)_2$ holding layer during the deposition process. Additionally, after the post-process, the adhesion of the coating is further increased, reducing the coating's fragility.

The as-deposited TEA system presents near super-hydrophobic wetting behavior, with contact angle measurements that reach 140°. The primary drawback is the fragility that the coating presents. Great care must be taken when manipulating these samples so as to not remove parts of the coating. To improve this shortcoming, TEA samples are submitted to the aforementioned post-deposition process. Initially, this process

diminishes the coating's wetting behavior by 18%. Although the surface's reactivity with fluids is increased, the surface is still considered hydrophobic. However, this weakening of the wetting behavior is traded off for an increase in the coating's adhesion. After the cooking process, the coating's fragility is decreased, allowing easier sample manipulation. This tradeoff is considered beneficial since the coating maintains its hydrophobic behavior, but also presents an increase in its adhesion to the substrate.

The benefits obtained by the post-process on TEA samples is governed primarily by the time of the isothermal post-treatment. Contrarily as for Mg-Nit samples, coating thickness is not a key factor. As the cook time increases, the wetting behavior improves as well. Therefore, for prolonged post-deposition processes, the aforementioned tradeoff between wetting behavior and adhesion is not necessary. In other words, for longer post-deposition processes, the adhesion of the coating to the substrate increases while maintaining high contact angles. This observation is proved when comparing two TEA samples with similar thicknesses and different cooking periods. For shorter cook times, the wetting properties are diminished compared to the as-deposited TEA sample. For longer cook times however, the contact angle measurements obtained are similar to the as-deposited samples.

As an alternative to generate a coating system that entails the advantages from both additives, double depositions were produced. Combining the benefits from both additives, the additional post-deposition process would not be required. Therefore, a thin layer of Mg-Nit coating is deposited over the substrate's surface, and an outer layer of TEA coating deposited over the Mg-Nit layer. This way, the coating has an adequate adhesion to the substrate, as a consequence of the innermost Mg-Nit coating, and the surface of the coating possesses a hydrophobic behavior because of the outermost TEA coating.

This system was proven effective due to the fact that the contact angle measurements obtained correspond to a near super-hydrophobic surface with values of 141°. From these results, it is confirmed that the measurements correspond to the outer TEA layer and not the hydrophilic behavior of Mg-Nit.

Chemical analysis of the different coatings do not reveal unexpected elements, except for the analysis conducted on the cooked sample. This sample shows the presence of sulfur dispersed homogeneously throughout the coating. A linear, in-depth scan of the

coating provides additional information on how this element is distributed throughout the coating. The linear EDS image shows that sulfur is primarily found near the substrate and specifically near the surface of the coating. The improved hydrophobicity of the cooked samples is explained by molecular sulfur found in these coatings [69]. Alone, CNT are hydrophobic [2]. However, the additives that are used to deposit the CNT on the substrate's surface make the CNT reactive, reducing their hydrophobicity. The introduction of sulfur in the coating's matrix increases once again the hydrophobic behavior of the coating due to the hydrophobic nature of molecular sulfur.

In terms of thickness, analysis have shown that for same deposition times Mg-Nit depositions are deposited at a lower rate than TEA depositions. For a set time of five minutes, Mg-Nit coatings produce thicknesses of 12.5 µm while TEA coatings produce thicknesses of 16.2 µm. This is once again seen in the double deposition sample. The total deposition time is five minutes as well, three minutes corresponding to Mg-Nit deposition and two minutes corresponding to TEA deposition. The resulting coating possesses a thickness that is bounded between the corresponding thickness for Mg-Nit and TEA, equivalent to 14 µm. Additionally, when referring to compactness, the Mg-Nit coatings shows a highly-packed coating with some small and scattered porosities. The TEA coating, on the other hand, presents a highly porous network. Furthermore, the coating's surface obtained for both coatings differs significantly. The surface of Mg-Nit presents few CNT agglomerates and small pores, while TEA's surface presents large CNT agglomerates with areas that prove to be thinly coated. Despite this difference in compactness and surface homogeneity, after the post-process, either coating's surfaces react with the droplet. Therefore, it reasonable to state that neither the Wenzel effect nor the Cassie-Baxter effect apply in these cases.

Different types of samples with different geometries and surface finishing were coated. Regardless of the different characteristics of the coated samples, the deposition process proved to be successful. Flat polished surfaces, flat rough surfaces and curved rough surfaces, the CNT deposited adhered successfully to the surface of the substrate. This demonstrates that the chosen deposition technique is efficient when it comes to coating complex geometries.

As it was mentioned before, this study was conducted considering that this investigation has a direct industrial application. Based on what was exposed in this thesis, it can be concluded that all three coating systems possess the characteristics required to

protect the sucker rods from corrosion. For this reason, the selection of the most appropriate system is done with a financial and safety criteria. Both these criteria must be taken into consideration since both cannot be equally met for one specific system.

The cooked Mg-Nit system complies with the safety criteria. The dispersing solvents and the additive are not harmful to the worker's health and no special equipment is required to manipulate said components. Furthermore, the amount of CNT used is relatively low when compared to the other two systems due to the lower thickness that this deposition produces. By adding the final post-deposition process this system combines all the requirements needed, making this system viable.

The cooked TEA system does not meet the safety criteria. TEA is a toxic additive, care must be taken when manipulating this chemical. Therefore, a fume hood must be available when working with TEA. From a financial point of view however, this systems is more viable than the Mg-Nit system. To obtain hydrophobicity with these depositions, a thin layer of CNT coating is required, making this system more cost-efficient than the Mg-Nit system.

The double deposition system is caught somewhere between the other two systems. This system does not require the post-deposition process, however it does require two separate deposition processes. As this system involves the use of TEA as an additive, it does not meet the safety criteria.

Based on these criteria, the most appropriate system is the cooked Mg-Nit system. The amount of material used is relatively low, producing thin coatings. This is sought after because the CNT used in the coating are not wasted. Additionally, the additive used is not toxic, making it safe to manipulate without special equipment. Lastly, the post-deposition process is simple and straightforward, with much to gain. The costs of this additional process is considerably low since it consists of crude oil (which is brought from the oil well where the sucker rods will be used), a container and a heat source.

As an added advantage to the Mg-Nit system, rods are able to be coated and treated at a higher rate compared to the TEA system. Although TEA coatings are deposited for shorter periods of time, they require prolonged periods of post-processing. Mg-Nit coatings require a few minutes more to deposit the CNT coating, but require less post-processing than TEA coatings. When comparing the post-processing of Mg-Nit coatings with a two-step deposition, the post-processing is considered more convenient. This is

based on the idea that the consumers of the manufactured sucker rods will provide the manufacturers with the crude oil required to produce the rods. Also, having a two-step deposition technique involves more sophisticated equipment than a one-step deposition technique with an added post-deposition process.

In a further work, it would be of interest to study in detail the formation of the holding layer. This could possibly allow the reproduction of this holding layer with the use of different additives. This would allow the acquisition of as-deposited hydrophobic coatings with proper adhesion. Additionally, it would also be of interest to study corrosion resistance via different techniques (e.g. anodic polarization tests). Conducting complex studies would allow for a more comprehensive understanding of the anticorrosive properties of the CNT coating. Furthermore, the deposition of different hydrophobic CNP for corrosion protection would be of interest. Finally, since sucker rods are subject to corrosion and wear during normal operational conditions, it would be of interest to study the wear behavior that the CNT-coated sucker rods present when compared to the non-coated sucker rods utilizing a nanotribometer. Moreover, adhesion could also be studied via scratch test and/or “scotch tape test” to have a qualitative understanding of how the post-deposition process improves the coating’s adhesion.

References

[1] L. Reinert *et al.*, “Long-lasting solid lubrication by CNT-coated patterned surfaces,” *Sci. Rep.*, vol. 7, no. July 2016, pp. 1–13, 2017.

[2] T. MacLucas, S. Schütz, S. Suárez, and F. Mücklich, “Surface protection of austenitic steels by carbon nanotube coatings,” *Surf. Topogr. Metrol. Prop.*, vol. 6, no. 1, p. 14005, 2018.

[3] L. Reinert, S. Schütz, S. Suárez, and F. Mücklich, “Influence of surface roughness on the lubrication effect of carbon nanoparticle-coated steel surfaces,” *Tribol. Lett.*, vol. 66, no. 1, pp. 1–16, 2018.

[4] S. Nasir, M. Z. Hussein, Z. Zainal, and N. A. Yusof, “Carbon-based nanomaterials/allotropes: A glimpse of their synthesis, properties and some applications,” *Materials (Basel).*, vol. 11, no. 2, pp. 1–24, 2018.

[5] L. Reinert, M. Zeiger, S. Suárez, V. Presser, and F. Mücklich, “Dispersion analysis of carbon nanotubes, carbon onions, and nanodiamonds for their application as reinforcement phase in nickel metal matrix composites,” *RSC Adv.*, vol. 5, no. 115, pp. 95149–95159, 2015.

[6] P. Ajayan and O. Zhou, “Applications of Carbon Nanotubes Carbon Nanotubes,” vol. 80, pp. 391–425, 2001.

[7] S. Beg, M. Rizwan, A. M. Sheikh, M. S. Hasnain, K. Anwer, and K. Kohli, “Advancement in carbon nanotubes: Basics, biomedical applications and toxicity,” *J. Pharm. Pharmacol.*, vol. 63, no. 2, pp. 141–163, 2011.

[8] K. A. Shah and B. A. Tali, “Synthesis of carbon nanotubes by catalytic chemical vapour deposition: A review on carbon sources, catalysts and substrates,” *Mater. Sci. Semicond. Process.*, vol. 41, pp. 67–82, 2016.

[9] R. Saito, G. Dresselhaus, and M. S. Dresselhaus, *Physical Properties of Carbon Nanotubes*. London: Imperial College Press, 1998.

[10] H. Jiang *et al.*, “The effect of nanotube radius on the constitutive model for carbon nanotubes,” *Comput. Mater. Sci.*, vol. 28, no. 3–4 SPEC. ISS., pp. 429–442, 2003.

[11] M. Terrones *et al.*, “Graphene and graphite nanoribbons: Morphology, properties, synthesis, defects and applications,” *Nano Today*, vol. 5, no. 4, pp. 351–372, 2010.

References

[12] C. J. Brinker, “Chemical Solution Deposition of Functional Oxide Thin Films,” pp. 233–261, 2013.

[13] J. Puetz and M. A. Aegerter, “Dip Coating Technique,” *Sol-Gel Technol. Glas. Prod. Users*, pp. 37–48, 2004.

[14] K. Kalantar-Zadeh and B. Fry, “Spin Coating and Drop Casting,” in *Nanotechnology-Enabled Sensors*, Springer US, 2008.

[15] W. A. Barlow, “Langmuir-Blodgett films,” vol. 263, no. March, 1980.

[16] A. E. Engineering, “Spin Coating,” no. April 2007, pp. 1–8, 2011.

[17] J. F. Taylor, “Spin coating: An overview,” *Met. Finish.*, vol. 99, no. 1, pp. 16–21, 2001.

[18] L. E. Scriven, “Physics and Applications of Dip Coating and Spin Coating,” *Better Ceram. Through Chem. III*, vol. 121, pp. 717–729, 1988.

[19] M. Schmitt and H. Stark, “Marangoni flow at droplet interfaces: Three-dimensional solution and applications,” *Phys. Fluids*, vol. 28, no. 1, 2016.

[20] L. E. Scriven and C. V. Sternling, “The Marangoni Effects,” *Nature*, vol. 187, no. 4733, pp. 186–188, 1960.

[21] J. Zhang, J. Milzetti, F. Leroy, and F. Müller-Plathe, “Formation of coffee-stain patterns at the nanoscale: The role of nanoparticle solubility and solvent evaporation rate,” *J. Chem. Phys.*, vol. 146, no. 11, 2017.

[22] R. C. Tucker and P. S. T. Inc, “Thermal Spray Coatings,” *Handb. Surf. Eng.*, vol. 5, pp. 1446–1471, 1993.

[23] M. F. Smith, *Comparing cold spray with thermal spray coating technologies*. 2007.

[24] J. X. Zhang, “Analysis on the effect of venturi tube structural parameters on fluid flow,” *AIP Adv.*, vol. 7, no. 6, 2017.

[25] A. R. Boccaccini, J. Cho, J. A. Roether, B. J. C. Thomas, E. Jane Minay, and M. S. P. Shaffer, “Electrophoretic deposition of carbon nanotubes,” *Carbon N. Y.*, vol. 44, no. 15, pp. 3149–3160, 2006.

[26] J. H. Dickerson and A. R. Boccaccini, *Electrophoretic Deposition of Nanomaterials*, 2nd Editio. Sp, 2011.

[27] P. Sarkar and P. S. Nicholson, “Electrophoretic deposition (EPD): Mechanisms, kinetics, and application to ceramics,” *Journal of the American Ceramic Society*, vol. 79, no. 8. pp. 1987–2002, 1996.

[28] H. C. Hamaker, “Formation of a Deposit by Electrophoresis,” *Trans. Faraday*

Soc., vol. 30, pp. 279–287, 1940.

[29] M. Farrokhi-Rad and T. Shahrabi, "Electrophoretic deposition of titania nanoparticles: Sticking parameter determination by an in situ study of the EPD kinetics," *J. Am. Ceram. Soc.*, vol. 95, no. 11, pp. 3434–3440, 2012.

[30] I. Minkoff, "Applications of the scanning electron microscope in materials science," *J. Mater. Sci.*, vol. 2, no. 4, pp. 388–394, 1967.

[31] L. A. Giannuzzi and F. A. Stevie, *Introduction to Focused Ion Beams: Instrumentation, Theory, Techniques and Practice*. Springer US, 2005.

[32] A. J. Wilkinson and T. B. Britton, "Strains, planes, and EBSD in materials science," *Mater. Today*, vol. 15, no. 9, pp. 366–376, 2012.

[33] T. B. Britton *et al.*, "Tutorial: Crystal orientations and EBSD - Or which way is up?," *Mater. Charact.*, vol. 117, pp. 113–126, 2016.

[34] S. I. Wright, M. M. Nowell, R. De Kloe, P. Camus, and T. Rampton, "Electron imaging with an EBSD detector," *Ultramicroscopy*, vol. 148, pp. 132–145, 2015.

[35] D. B. Williams and C. B. Carter, *Transmission Electron Microscopy*. Springer US, 2009.

[36] R. O. Duda and P. E. Hart, "Use of the Hough transform to detect lines and cures in pictures," *Commun. Assoc. Comput. Mach.*, vol. 15, no. 1, pp. 11–15, 1972.

[37] EDAX, "OIM Analysis Software." .

[38] H. Stanjek, "Basics of X-ray Diffraction," no. 617, pp. 107–119, 2004.

[39] A. Chauhan and P. Chauhan, "Powder XRD Technique and its Applications in Science and Technology," *J. Anal. Bioanal. Tech.*, vol. 5, no. 6, 2014.

[40] W. H. Bragg and W. L. Bragg, "Ley de Bragg," *Proc. R. Soc. A.*, vol. 88, pp. 428–438, 1913.

[41] C. Ashbacher, "Introduction to," p. 145, 2002.

[42] S. Provided, I. S. O. No, and I. H. S. Licensee, "INTERNATIONAL STANDARD ISO 6507-1: Metallic materials - Vickers hardness test," *Int. Stand.*, vol. 1, 2005.

[43] RENISHAW, "Raman Spectroscopy Explained," *RENISHAW -Apply Innov.*, no. March, pp. 1–44, 2017.

[44] E. Smith and G. Dent, *Modern Raman Spectroscopy: A Practical Approach*. John Wiley & Sons, Ltd, 2005.

[45] G. S. Bumbrah and R. M. Sharma, "Raman spectroscopy – Basic principle, instrumentation and selected applications for the characterization of drugs of

abuse," *Egypt. J. Forensic Sci.*, vol. 6, no. 3, pp. 209–215, 2016.

[46] R. A. DiLeo, B. J. Landi, and R. P. Raffaelle, "Purity assessment of multiwalled carbon nanotubes by Raman spectroscopy," *J. Appl. Phys.*, vol. 101, p. 064307/1-5, 2007.

[47] K. Ramadurai, C. L. Cromer, A. C. Dillon, R. L. Mahajan, and J. H. Lehman, "Raman and electron microscopy analysis of carbon nanotubes exposed to high power laser irradiance," *J. Appl. Phys.*, vol. 105, no. 9, 2009.

[48] R. DiLeo, B. Landi, and R. Raffaelle, "Application of the G'/D Raman Ratio for Purity Assessment of Multi-Walled Carbon Nanotubes," *MRS Proc.*, vol. 1018, pp. 1018-EE05-11, 2011.

[49] J. H. Lehman, M. Terrones, E. Mansfield, K. E. Hurst, and V. Meunier, "Evaluating the characteristics of multiwall carbon nanotubes," *Carbon N. Y.*, vol. 49, no. 8, pp. 2581–2602, 2011.

[50] A. Koshanova *et al.*, "Synthesis of carbon nanostructures on iron nanopowders," *J. Phys. Conf. Ser.*, vol. 741, no. 1, pp. 201–207, 2016.

[51] T. C. Hirschmann *et al.*, "G'Band in double- and triple-walled carbon nanotubes: A Raman study," *Phys. Rev. B - Condens. Matter Mater. Phys.*, vol. 91, no. 7, 2015.

[52] G. Bracco and B. Holst, *Surface science techniques*, vol. 51, no. 1. 2013.

[53] W. M. Robertson and G. W. Lehman, "The shape of a sessile drop," *J. Appl. Phys.*, vol. 39, no. 4, pp. 1994–1996, 1968.

[54] S. W. Rienstra, "The shape of a sessile drop for small and large surface tension," *J. Eng. Math.*, vol. 24, no. 3, pp. 193–202, 1990.

[55] G. L. Mack and D. A. Lee, "The Determination of Contact Angles from Measurements of the Dimensions of Small Bubbles and Drops. II. The Sessile Drop Method for Obtuse Angles," *J. Phys. Chem.*, vol. 40, no. 2, pp. 169–176, 1935.

[56] A. W. Adamson, "Physical Chemistry of Surfaces," *J. Electrochem. Soc.*, vol. 124, no. 5, p. 192C, 1977.

[57] ASTM, "Standard D7490--13 Standard Test Method for Measurement of the Surface Tension of Solid Coatings, Substrates and Pigments using Contact Angle Measurements," *Astm*, pp. 1–5, 2013.

[58] G. Whyman, E. Bormashenko, and T. Stein, "The rigorous derivation of Young, Cassie-Baxter and Wenzel equations and the analysis of the contact angle

hysteresis phenomenon," *Chem. Phys. Lett.*, vol. 450, no. 4–6, pp. 355–359, 2008.

[59] S. Provided, I. S. O. No, and I. H. S. Licensee, "INTERNATIONAL STANDARD ISO 6106: Abrasive products - Checking the grain size of superabrasives," vol. 2013, 2013.

[60] S. Santhanagopalan, A. Balram, E. Lucas, F. Marcano, and D. D. S. Meng, "High Voltage Electrophoretic Deposition of Aligned Nanoforests for Scalable Nanomanufacturing of Electrochemical Energy Storage Devices," *Key Eng. Mater.*, vol. 507, pp. 67–72, 2012.

[61] S. Santhanagopalan, F. Teng, and D. D. Meng, "High-voltage electrophoretic deposition for vertically aligned forests of one-dimensional nanoparticles," *Langmuir*, vol. 27, no. 2, pp. 561–569, 2011.

[62] P. Rameshkumar and R. Ramaraj, "Gold nanoparticles deposited on amine functionalized silica sphere and its modified electrode for hydrogen peroxide sensing," *J. Appl. Electrochem.*, vol. 43, no. 10, pp. 1005–1010, 2013.

[63] M. F. De Riccardis, D. Carbone, and A. Rizzo, "A novel method for preparing and characterizing alcoholic EPD suspensions," *J. Colloid Interface Sci.*, vol. 307, no. 1, pp. 109–115, 2007.

[64] A. C. Ferrari and J. Robertson, "Interpretation of Raman spectra of disordered and amorphous carbon," *Phys. Rev. B - Condens. Matter Mater. Phys.*, vol. 61, no. 20, pp. 14095–14107, 1999.

[65] F. Tuinstra and J. L. Koenig, "Raman spectrum of graphite," *J. Chem. Phys.*, vol. 53, pp. 1126–1130, 1970.

[66] M. A. Pimenta, G. Dresselhaus, M. S. Dresselhaus, L. G. Cançado, A. Jorio, and R. Saito, "Studying disorder in graphite-based systems by Raman spectroscopy," *Phys. Chem. Chem. Phys.*, vol. 9, no. 11, pp. 1276–1291, 2007.

[67] S. Suarez, F. Lasserre, O. Prat, and F. Mücklich, "Processing and interfacial reaction evaluation in MWCNT/Ni composites," *Phys. Status Solidi Appl. Mater. Sci.*, vol. 211, no. 7, pp. 1555–1561, 2014.

[68] M. S. Dresselhaus, G. Dresselhaus, R. Saito, and A. Jorio, "Raman spectroscopy of carbon nanotubes," in *physics Reports*, vol. 409, 2005, pp. 47–99.

[69] G. W. Walker, C. P. Walters, and P. E. Richardson, "Hydrophobic effects of sulfur and xanthate on metal and mineral surfaces," *Int. J. Miner. Process.*, vol. 18, pp. 119–137, 1986.

[70] ASTM, “Standard D1193-91 -- Water Quality Standards.” 1999.

[71] S. P. ASTM, “B 0117 Operating Salt Spray (Fog) Apparatus,” *Astm*, pp. 1–12, 2011.

[72] S. Suarez, N. Souza, F. Lasserre, and F. Mücklich, “Influence of the Reinforcement Distribution and Interface on the Electronic Transport Properties of MWCNT-Reinforced Metal Matrix Composites,” *Adv. Eng. Mater.*, vol. 18, no. 9, pp. 1626–1633, 2016.

[73] Q. Ngo *et al.*, “Electron transport through metal-multiwall carbon nanotube interfaces,” *IEEE Trans. Nanotechnol.*, vol. 3, no. 2, pp. 311–317, 2004.

[74] C. Li, E. T. Thostenson, and T. W. Chou, “Dominant role of tunneling resistance in the electrical conductivity of carbon nanotube-based composites,” *Appl. Phys. Lett.*, vol. 91, no. 22, pp. 91–94, 2007.

Appendix A

Electrical behavior of the coating: Contact resistance determination

The rationale behind determining the dependence of the electrical contact resistance upon the compressive mechanical load and electrical current is that, for different compactness grades and doping elements, the electrical behavior of the coating would differ. Furthermore, if successful, it would provide a "quasi" non-destructive method to assess the coating quality and thickness that could be straightforwardly up-scaled to industrial-size CNT-based coatings.

The determination of the electrical resistivity of the coating was carried out utilizing an equipment that measures the contact resistance between two different materials based on the two-probe method. This equipment consists of a static gold electrode, through which it applies a set current when it comes into contact with the mobile counter electrode (sample). It later registers the voltage and by applying Ohm's Law, the resistance is obtained. Additionally, this equipment allows the user to control the contact force between the two electrodes utilizing a load cell with a strain gauge and a servomotor (which moves the mobile stage). **Fig. A.1** shows the experimental set-up with a sample ready to be measured. **Fig. A.2** shows the electrical equivalent circuit. The power source is a constant DC generator. The resistance (R) is the resistance between the gold electrode and the CNT coating. Voltage is measured between these two points.

The electrical resistance was measured on three different samples: steel reference, Mg-Nit coated and TEA coated. For all samples, ten measurements are taken for different applied forces. The force steps increase by 0.25 N intervals, from an initial force of 0.25 N to 4 N. In the constant current tests, the applied current is 10 mA (applied for three seconds) with two measuring cycles (a full load-unload loop 0.25N-4N-0.25N).

Appendix A

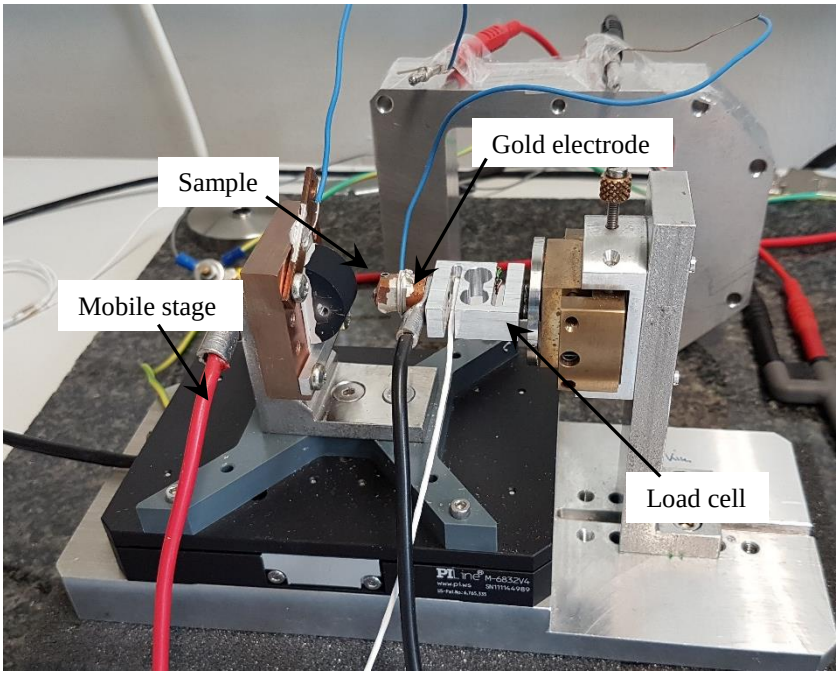

Fig. A.1 – Contact resistance measurement setup.

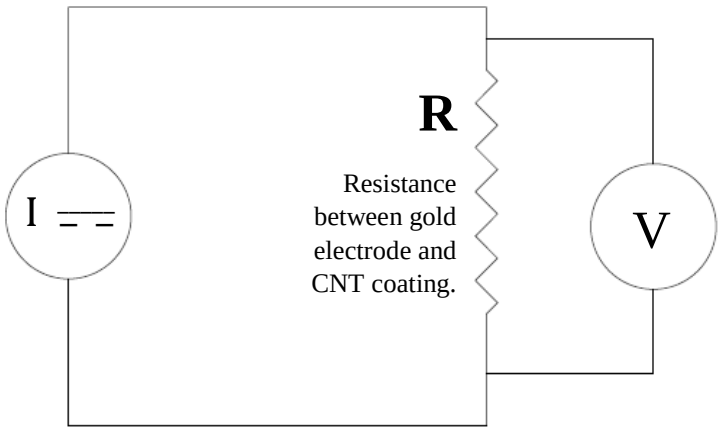

Fig. A.2 – Electrical circuit for resistivity measurements.

Reference sample

The reference sample was measured so as to obtain its electrical behavior and use it as a baseline for the analysis of the coatings.

Fig. A.3 shows the resistance measured for the reference sample during four complete measurement cycles. As it can be seen, for the first cycle and low contact forces, the resistance measured is around 1.4 Ω. With a single force increment, to 0.5 N, the contact resistance measured significantly decreases to about 0.7 Ω. As the contact force steadily increases, the measured resistance decreases. This is due to an effective increase in the real contact area, hence reducing the constriction resistance brought by the contact

between asperities. At the end of the first measuring cycle, at 4 N, the resistance reaches its lowest value of 0.1 Ω. During the second measurement cycle the resistance increases slightly to 0.3 Ω, whereas during the last two cycles, the resistance remains fairly constant at values between 0.2 Ω and 0.3 Ω.

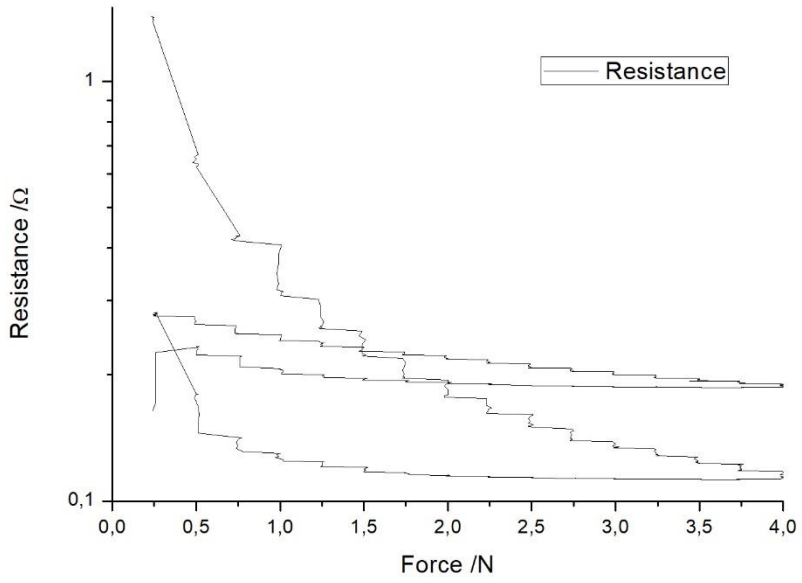

Fig. A.3 - Resistivity of reference sample for 4 measurement cycles.

Furthermore, it is of interest to measure the resistivity as a function of the current for a given contact force. This study presents the advantage that the measurements taken are more stable since the electrical noise measured from outer sources is reduced. **Fig. A.4** shows how the contact resistance is influenced by the applied current for a set contact force of 0.5 N. Observing this figure, it is clear to see that the contact resistance is high for low currents, but sharply decreases as the applied current increases. For low current values ($3x10^{-9}$ A through $3x10^{-4}$ A) the measured resistance is between 35 Ω and 65 Ω. The first measurement however ($1x10^{-9}$ A), results in a significantly higher resistance, about 240 Ω. Once the applied current surpasses values of approximately 0.01 A, the measured resistance is below 20 Ω.

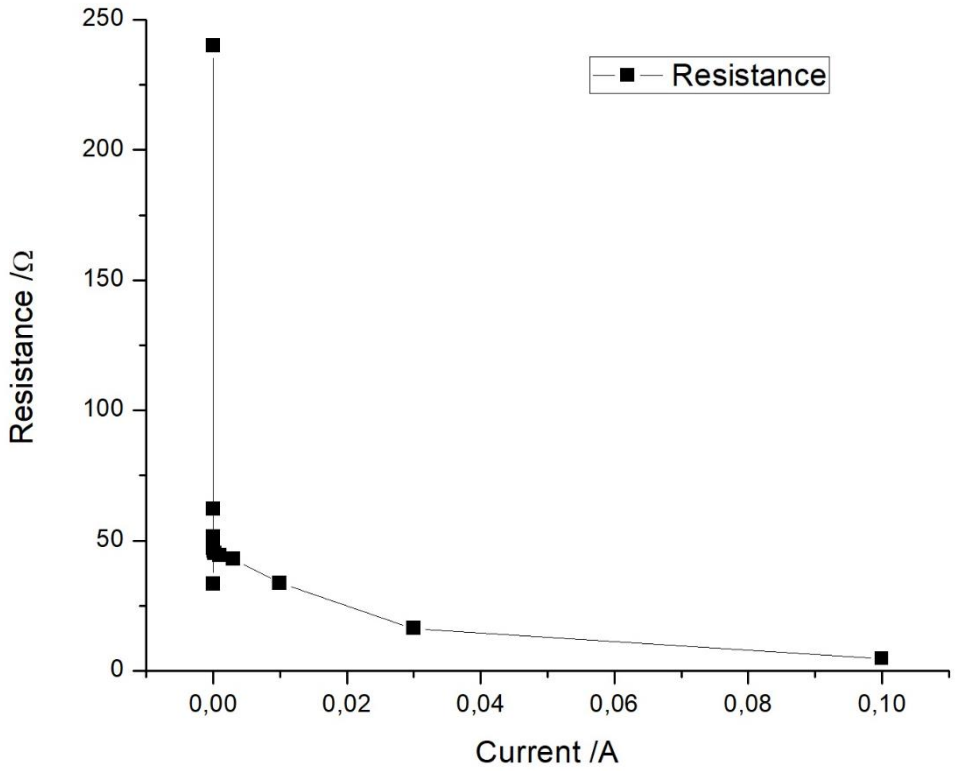

Fig. A.4 - Resistance as a function of applied current for 0.5 N contact force for reference sample.

Mg-Nit sample

Fig. A.5 depicts the resistivity measurements of two cycles for the Mg-Nit sample. As this image shows, the initial resistance for low contact force is extremely high. Approximately 93 times higher than the resistance of the reference sample for the same measurement conditions. This is in agreement with reports in the literature, which state that due to the strong anisotropy in the electrical/electronic response of the CNT, a side-wall contact would raise up to some kΩ [72], [73]. Considering that the CNT lay horizontally on top of the substrate, this situation is the most likely. However, the overall resistance would seldomly reach values in this range (kΩ), since they would form a percolation network of parallel electrical paths. Similarly as for the reference sample, as the contact force increases, the measured resistance decreases. At the beginning of the first cycle, the resistance is about 130 Ω. At the end of the first cycle however, the resistance has dropped down to about 1.2 Ω. The continuous drop throughout the scanned forces is related to the closure of the spacing between the different constituent CNT. It is known that there is a threshold distance that should be overcome (by bringing neighboring

CNT together), thereby allowing an electron to hop between CNT and thus, travel the lowest resistance path, also known as inter-tube tunneling [72]–[74].

The final resistance value coincides with the approximate resistance measured for the reference samples at low contact forces. Therefore, it can be deduced that the resistivity measured at the end of the first measurement cycle is the resistance of the substrate and defining –qualitatively–the compressive strength limit of the coating. Throughout the entire second cycle, the measured resistance remains to some extent constant, with values slightly above 1 Ω, indicating that the coating has been irreversibly damaged.

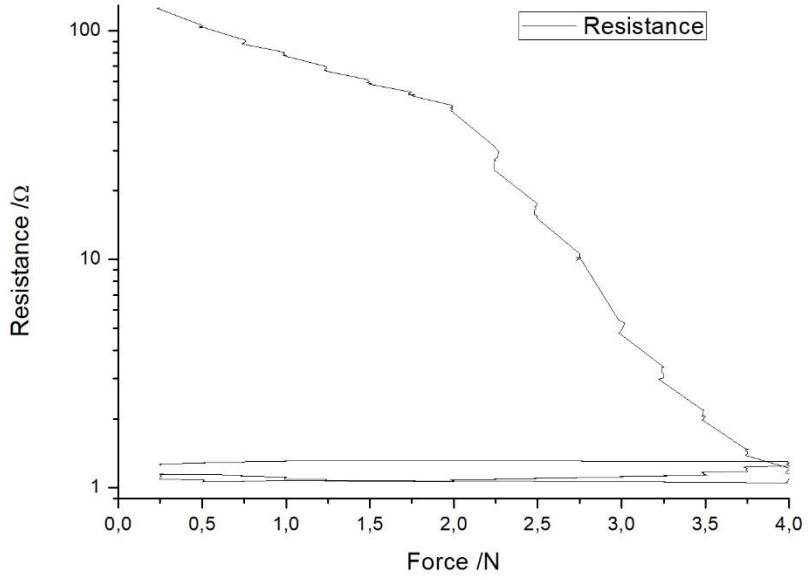

Fig. A.5 - Resistivity of Mg-Nit sample after two measurement cycles.

As it was done for the reference sample, the resistance as a function of the current was measured for an applied force of 0.5 N. This is shown in **Fig. A.6**. Similarly as for the reference sample, the resistance obtained for low currents is much higher than for currents surpassing 0.01 A.

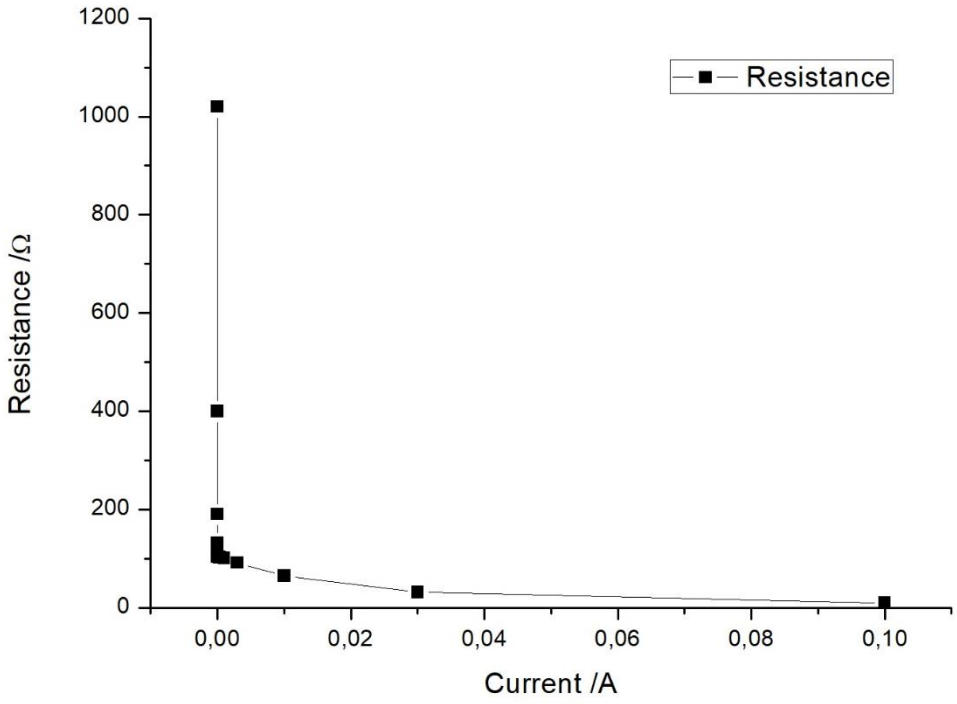

Fig. A.6 - Resistance as a function of applied current for 0.5 N contact force for Mg-Nit sample.

TEA sample

Fig. A.7 depicts the for measurement cycles for the TEA sample. When compared to the reference and Mg-Nit, the initial resistance is higher than for the reference, but lower than the Mg-Nit sample. This results is reasonable, considering that the amount of foreign species present after the deposition with TEA is significantly smaller than in the Mg-Nit case.

During the first cycle, the resistance for 0.25 N is about 75 Ω. As for the other samples, the resistance decreases as the applied force increases. At the end of the first cycle, the measured resistance has a value of approximately 20 Ω, which is considerably higher than for the reference and Mg-Nit samples which both had values below 1.5 Ω. During the second cycle, the resistance increases as the force decreases, being this associated to an elastic restitution of the coating. The value of resistance measured at the end of the second cycle is elevated as well, reaching a value of approximately 50 Ω. Once again, this value is significantly higher than for the reference and Mg-Nit samples. In the third cycle the resistance decreases once again, but the final value is about 5 Ω higher than the value for the first cycle. Nonetheless, the resistance value at the end of the fourth and final cycle is exactly the same as for the end of the second cycle. It is worth

mentioning that, from these observations, it seems that the TEA shows a better compressive response than the Mg-Nit samples. This elastic behavior might be useful when the coated component is subjected to impact stresses in a normal direction. Moreover, the coating shows a low hysteresis after 5 loading cycles, which speaks about the reliability in monotonically loaded contact situations.

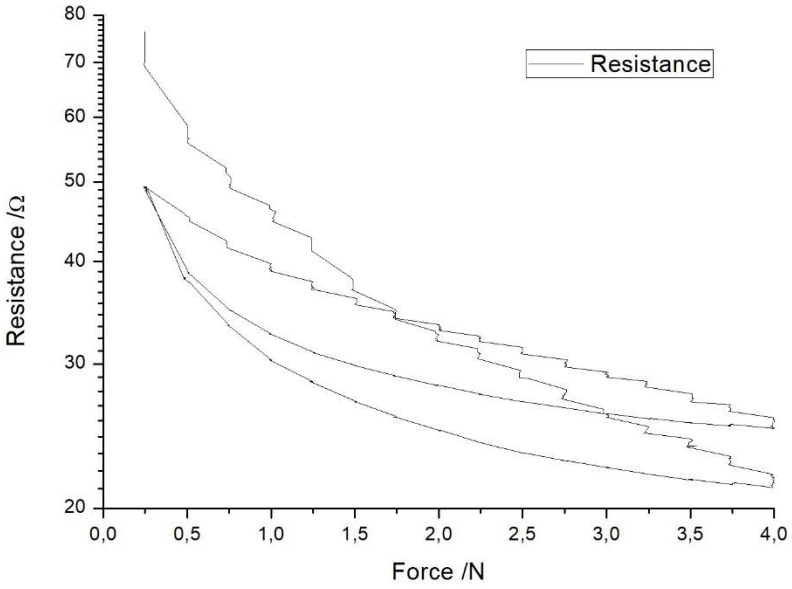

Fig. A.7 - Resistivity of TEA sample after four measurement cycles.

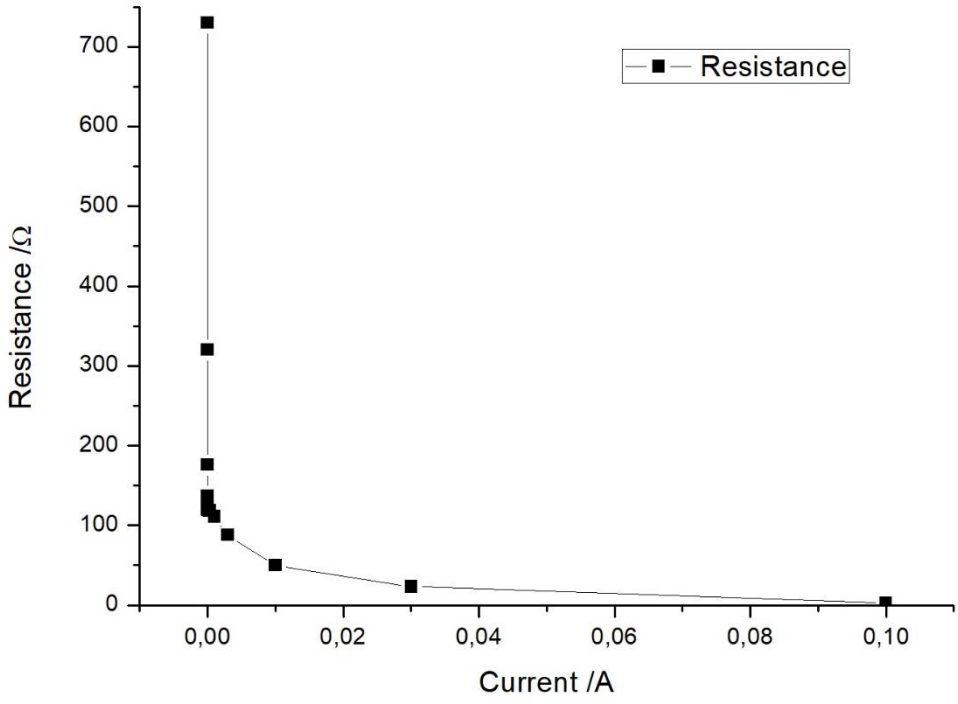

Fig. A.8 - Resistance as a function of applied current for 0.5 N contact force for Mg-Nit sample.

Appendix A

Although the resistivity curve of the TEA sample for varying force is very different to the other two samples, when the current is varied and the force is maintained constant the curve is very similar to the other two samples, **Fig. A.8**. For low currents, the resistance is extremely elevated, surpassing 700 Ω. Nonetheless, for currents above 0.01 A, the resistance drops below 50 Ω, which is still much higher than for the other two samples. For currents above 0.1 A however, the resistance drops down to about 3 Ω, which is a similar value when compared to the other two samples.

Appendix B

List of figures

Appendix B

Appendix B

Appendix B

List of tables

List of equations

List of units

Unit	Name
°C	Degree Celsius.
°	Degrees.

Appendix B

Unit	Name
g	Grams.
s	Seconds.
m	Meters.
V	Volts.
A	Ampere.
N	Newton.
cm^{-1}	Wavenumbers.
bar	Bar.
L	Liter.
Hz	Hertz.
W	Watts.
rpm	Revolutions per minute.
eV	Electron Volt.
Ω	Ohm.

List of symbols

Symbol	Meaning
dw/dt	Particle deposition rate.
μ	Electrophoretic mobility.
c	Particle concentration.
A	Deposition area.
E	Electric field.
f	Sarkar and Nicholson's efficiency factor.
j_i	Mass flow of particles that are deposited.
j_d	Mass flow of detached particles.
ε_o	Vacuum permittivity.
ε_r	Relative dielectric constant.
ζ	Zeta potential
η	Dynamic viscosity.
d	Interplanar distance.
θ	Diffraction angle (Bragg).

Symbol	Meaning
λ	Wavelength.
F	Force.
I_D	D band intensity.
I_G	G band intensity.
$I_{G'}$	G' band intensity.
θ_c	Contact angle.
γ_{SG}	Surface tension between solid-gas phase.
γ_{SL}	Surface tension between solid-liquid phase.
γ_{LG}	Surface tension between liquid-gas phase.
R_a	Arithmetic roughness.
L_a	Mean inter-defect distance.

List of abbreviations

Abbreviation	Meaning
CNT	Carbon nanotube(s).
EPD	Electrophoretic deposition.
Mg-Nit	Magnesium nitrate hexahydrate.
TEA	Triethylamine.
CNP	Carbon nanoparticle(s).
SWCNT	Single-walled carbon nanotube(s).
MWCNT	Multiwall carbon nanotube(s).
CVD	Chemical vapor deposition.
DC	Direct current.
SEM	Scanning electron microscope.
FIB	Focused ion beam.
EBSD	Electron backscatter diffraction.
IPF	Inverse pole figure.
IQ	Image quality.
XRD	X-Ray diffraction.
RBM	Regular breathing mode.
IPA	Isopropanol.

Appendix B

Abbreviation	Meaning
DD	Double deposition.
PDF	Powder diffraction file.
ICDD	International Center for Diffraction Data.
CI	Confidence index.
FWHM	Full width at half maximum.
EDS	Energy-dispersive X-Ray spectroscopy.